IN SITU SYNTHESIS AND GROWTH OF NANOPARTICLES USING A LIQUID CELL TRANSMISSION ELECTRON MICROSCOPY

Bojan Ambrožič

Doctoral Dissertation
Jožef Stefan International Postgraduate School
Ljubljana, Slovenia

Supervisor: Prof. Dr. Sašo Šturm, Jožef Stefan International Postgraduate School and Jožef Stefan Institute, Slovenia

Evaluation Board:
Prof. Dr. Goran Dražić, Chair, Jožef Stefan International Postgraduate School and National Institute of Chemistry, Ljubljana Slovenia
Assist. Prof. Dr. Blaž Likozar, Member, National Institute of Chemistry, Ljubljana Slovenia
Prof. Dr. Yuki Kimura, Member, Institute of Low Temperature Science, Hokkaido University, Sapporo, Japan

MEDNARODNA PODIPLOMSKA ŠOLA JOŽEFA STEFANA
JOŽEF STEFAN INTERNATIONAL POSTGRADUATE SCHOOL

Bojan Ambrožič

IN SITU SYNTHESIS AND GROWTH OF NANOPARTICLES USING A LIQUID CELL TRANSMISSION ELECTRON MICROSCOPY

Doctoral Dissertation

IN SITU SINTEZA IN RAST NANODELCEV V TEKOČINSKI CELICI PRESEVENGA ELEKTRONSKEGA MIKROSKOPA

Doktorska disertacija

Supervisor: Prof. Sašo Šturm

Ljubljana, Slovenia, September 2020

Acknowledgments

This research was financially supported by the Slovenian Research Agency (research core funding No. P2-0084 and P2-0152 and Project Z2-8161). Additional funding was received from the European Union's Horizon 2020 research and innovation program under grant agreement No. 823717 – ESTEEM3.

I acknowledge for the use of their research equipment to Jožef Stefan Institute, National Institute of Chemistry, Institute of Low Temperature Science at Hokkaido University and Center of Excellence on Nanoscience and Nanotechnology – Nanocenter.

This PhD thesis wouldn't have been completed without help from Prof. Dr. Sašo Šturm, Anže Prašnikar, Assoc. Prof. Dr. Nejc Hodnik, Dr. Nina Kostevšek, Maja Koblar, Dr. Špela Trafela, Dr. Ulrike Wolf, Dr. Marjan Bele, Prof. Dr. Goran Dražić, Prof. Dr. Yuki Kimura, Assist. Prof. Dr. Blaž Likozar and Prof. Dr. Saša Novak Krmpotič.

Abstract

This thesis deals with the liquid cell transmission electron microscopy (LCTEM) technique. LCTEM is currently at the frontier of the research into nanomaterials, since it enables in situ in-liquid nanoparticle-synthesis experiments at a sub-nanometer spatial resolution. LCTEM allowed us to make observations of the nucleation, growth/dissolution, and movement of nanoparticles in situ in a liquid. For this purpose, three different synthesis systems were applied: gold-based, yttrium-based, and iron-based.

It was found that for all the selected systems, radiolysis, induced by the 200-kV electron beam of a transmission electron microscope (TEM), has the predominant effect on the nanoparticle synthesis. In order to mitigate the radiolysis effects and produce reliable data about in situ nanoparticle synthesis, the kinetic radiolysis model was built. For the case of gold nanoparticle synthesis from a gold(III) chloride trihydrate solution, we could predict the gold nanoparticle precipitation/dissolution in relation to the induced dose rate and the temperature parameters. Kinetic radiolysis model predictions were matched with LCTEM in situ experiments, proving the model is valid for this experimental system and that it can be further expanded to other technologically important material systems. In the thesis, procedures for obtaining quantitative and replicable data with the LCTEM technique are thoroughly discussed.

In the case of the yttrium-based system as a model phosphor material, ex situ synthesis of the nanoparticles was performed from urea and a yttrium acetate hydrate solution. The experiments were replicated under the same conditions using the LCTEM technique. Both methods yielded the same result - amorphous yttria nanoparticles. In the second step, nanoparticles were annealed, which transformed them into crystalline yttrium hydroxide that could be used in the future in photonics. This is believed to be one the first reports of the synthesis of hydroxide powders using the LCTEM technique.

Iron nanoparticles were synthesized from Iron(II) sulfate heptahydrate, sodium citrate, and sodium sulfate solution using the electrochemical approach. First, a cyclic voltammetry study inside the LCTEM was used to investigate the electrochemical behavior of the studied Fe-based system. Based on these studies, the conditions for potentiostatic Fe deposition were determined, and the Fe deposition was performed for E= -1.1 V vs Pt quasi reference electrode in situ under dynamic conditions. Experiments were replicated under the same conditions using LCTEM. The synthesized nanoparticles were γ-iron, which is a material with interesting ferromagnetic properties.

Finally, artifacts resulting from radiolysis are shown and procedures for its mitigation are discussed.

Povzetek

Doktorska disertacija se ukvarja s tehniko presevna elektronska mikroskopija tekočin (LCTEM). LCTEM je napredna raziskovalna tehnika za in situ raziskave nanomaterialov v tekočinah, ker omogoča in situ sintezo nanodelcev v tekočinah s subnanometrsko prostorsko ločljivostjo. LCTEM nam je omogočila opazovanje nukleacije, rasti/raztapljanja in gibanja nanodelcev in situ v raztopinah. Izbrani so bili naslednji trije sintezni sistemi: zlatov, itrijev in železov.

Ugotovili smo, da ima radioliza, ki je posledica 200 kV elektronskega snopa presevnega elektronskega mikroskopa (TEM), glavni vpliva na vse tri izbrane sintezne sisteme. Z namenom, da smo zmanjšali učinke radiolize in da smo pridobili zanesljive informacije o in situ sintezi nanodelcev, smo izdelali kinetični model radiolize. Model nam je za primer sinteze zlatih nanodelcev iz raztopine zlatovega(III) klorida trihidrata omogočil predvideti obarjanje/raztapljanje zlatih nanodelcev v odvisnosti od parametrov hitrosti elektronske doze in temperature. Napovedi kinetičnega modela radiolize se ujemajo z LCTEM in situ eksperimenti, kar dokazuje, da je model pravilen za ta eksperimentalni sistem in da ga je možno v prihodnosti razširiti na druge tehnološko pomembne sisteme materialov. V disertaciji so natančno razloženi postopki za zajem kvantitativnih in ponovljivih podatkov s tehniko LCTEM.

V primeru itrijevega sistema smo izvedli eksperimente ex situ sinteze nanodelcev iz raztopine sečnine in itrijevega acetata hidrata. Eksperimenti so bili pri identičnih pogojih ponovljeni s tehniko LCTEM. V obeh primerih so nastali amorfni itrijevi nanodelci. V drugem koraku so bili nanodelci s postopkom žarjenja pretvorjeni v kristalinični itrijev hidroksid, ki ima potencialno uporabo v fotoniki. To je ena prvih raziskav, ki je s tehniko LCTEM uspešno sintetizirala hidroksidne nanodelce.

Železovi nanodelci so bili sintetizirani z elektrokemijskimi postopki iz raztopine železovega(II) sulfata heptahidrata, natrijevega citrat in natrijevega sulfata. Najprej je bilo s ciklično voltometrijo in tehniko LCTEM raziskano elektrokemijsko obnašanje preiskovanega železovega sistema. Na podlagi teh raziskav so bili določeni pogoji za potentiostatsko nanašanje Fe. Odlaganje Fe je bilo izvedeno in situ pri dinamičnih pogojih pri E=-1.1 V s Pt kvazireferenčno elektrodo. Eksperimenti so bili uspešno ponovljeni pri istih pogojih s tehniko LCTEM. Sintetizirani nanodelci so γ-železo, ki je material z zanimivimi feromagnetnimi lastnostmi.

Disertacija se zaključi z razpravo o artefaktih, ki so nastali kot posledica radiolize, in s seznamom posebnih postopkov za njihovo izničenje oz. zmanjšanje.

Contents

List of Figures

List of Tables

Abbreviations

AFM	. . .	Atomic force microscope/microscopy
BCC	. . .	Body-centered cubic
CCD	. . .	Charge-coupled device
CE	. . .	Counter electrode
CEMM	. . .	Center for Electron Microscopy and Microanalysis
CENN	. . .	Center of Excellence in Nanoscience and Nanotechnology
CNT	. . .	Classical nucleation theory
CV	. . .	Cyclic voltammetry
DFT	. . .	Density functional theory
EDS	. . .	Energy-dispersive X-ray spectroscopy
EELS	. . .	Electron energy loss spectroscopy
ETEM	. . .	Environmental transmission electron microscope / microscopy
Ex situ	. . .	Out of site / out of place
FCC	. . .	Face-centered cubic
FEG	. . .	Field emission gun
FIB	. . .	Focused ion beam
fps	. . .	Frames per second
ICSD	. . .	The Inorganic Crystal Structure Database
In situ	. . .	On the site / on the place
JSI	. . .	Jožef Stefan Institute
LCTEM	. . .	Liquid cell transmission electron microscopy
LET	. . .	Linear energy transfer
MP	. . .	Megapixel
mrad	. . .	Miliradian
MRI	. . .	Magnetic resonance imaging
NIST	. . .	National Institute of Standards and Technology
NPs	. . .	Nanoparticles
OCP	. . .	Open circuit potential
PEEK	. . .	Polyether ether ketone
ppm	. . .	Parts per million
RE	. . .	Reference electrode
SAED	. . .	Selected area electron diffraction
SDD	. . .	Silicon drift detector
SE	. . .	Secondary electrons
SEM	. . .	Scanning electron microscope/microscopy
SHE	. . .	Standard hydrogen electrode
STEM	. . .	Scanning transmission electron microscope/microscopy
TDR	. . .	Temperature/Dose-rate Redox potential diagrams
TEM	. . .	Transmission electron microscope/microscopy
UV	. . .	Ultraviolet radiation
WE	. . .	Working electrode
YAc	. . .	Yttrium acetate hydrate

Symbols

α	...	Objective semi-angle
C_C	...	Chromatic aberration coefficient
T_H	...	Thickness of the liquid layer
k_{water}	...	Inelastic scattering constant for water
E	...	Energy
e^-	...	Electron
e^-_{aq}	...	Solvated (aqueous) electron
$H^\bullet$	...	Hydrogen radical
H_2O_2	...	Hydrogen peroxide
HO_2^-	...	Hydroperoxyl
$HO_2^\bullet$	...	Hydroperoxyl radical
$O_2^\bullet$	...	Oxygen radical
H_3O^+	...	Hydronium
$HO_3^\bullet$	...	Hydrogen trioxy radical
Gy	...	Gray
ψ	...	Electron dose rate
S	...	Stopping power of water
As	...	Surface area
eV	...	Electronvolt
q_e	...	Elementary electron charge
C	...	Coulomb
s	...	Second
T	...	Temperature
G	...	Gibbs free energy
Gv	...	Free energy per unit volume
N_{r^*}	...	Number of clusters that reach crtical size
N_a	...	Avogadro constant
G^*	...	Critical free energy
r	...	Radius
r^*	...	Critical size of the nucleus
γ	...	Surface energy per unit area
V_m	...	Molar volume
R	...	Ideal gas constant
S_r	...	Ratio between solute concentration at saturation
E_e	...	Equilibrium potential
E^0	...	Standard electrode potential
n	...	Number
F	...	Faraday constant
M	...	Molar concentration
N	...	Newton
$Å$	...	Ångstrom
D	...	Dose rate
R_{pix}	...	Relative pixel size
I	...	Intensity
c_{cal}	...	Calibration factor

q_e	...	Elementary charge
c_n	...	Concentration of solute n
k	...	Rate constant
E_a	...	Activation energy
p	...	Pressure
J	...	Joule
q_e	...	Elementary electron charge
d_L	...	Thickness of liquid layer
R_i	...	Radiolytic yield
ρ	...	Density
G_i	...	G value
I_b	...	Beam current
a	...	Beam radius
$E_{p,a}$	...	Anodic peak potential
$E_{p,c}$	...	Cathodic peak potential
$i_{p,a}$	...	Anodic peak current
$i_{p,c}$	...	Cathodic peak current
A	...	Amper

Chapter 1

Introduction

Nanoparticles (NPs) represent an important class of nanomaterials [1], [2], widely used in electronics [3], optics [4] and the chemical industry [5], which is related to their high surface area [6], good magnetic and mechanical properties [7], including the recently widely studied photothermal effect in gold NPs [8]. These applications demand the synthesis of NPs with very high quality, such as monodispersibility and synthesis replicability [9]. As a consequence, controlling the synthesis parameters, especially in the early stage of NPs growth, is of vital importance to obtain high-quality NPs products [10]. Existing ex situ characterization techniques often lack quantitative data [11] about NP nucleation and early growth stages, which are crucial for the determination of comprehensive NPs synthesis mechanisms. As a solution to this challenge, the liquid cell transmission electron microscopy (LCTEM) technique [12] offers nanometer spatial and millisecond temporal resolution, allowing us to observe dynamic processes in situ during the nucleation and growth of industrially important NPs [13].

1.1 Liquid Samples

Liquid samples or samples that contain at least some amount of liquid (moisture) are an essential part of the research in many different fields of science: such as life sciences [14] (cell biology and molecular biology, viral and bacterial studies, cancer research, zoology of life samples, studies of food containing NPs, etc.), material science (hydrothermal growth studies and nucleation mechanism studies) [15] as well as also some fields of industry (such as the pharmaceutical research of drugs in vivo). All or at least many of these samples need to be observed on the nanoscale [13] in a pristine environment.

In this thesis, liquid samples were studied in relation to direct observations of the precipitation of individual NPs directly in situ from liquids. There was a huge advancement in the past few decades in the field of material characterization using electron microscopy with a very high spatial resolution [16]. However, there are still two basic problems that were only recently solved. First, observation of liquid samples by an electron microscope is normally not possible due to the required high vacuum inside the microscope [16]. Moreover, most liquids have the intrinsic property of a very high vapor pressure, which causes instantaneous evaporation inside the ultra-high vacuum of an electron microscope. Second, evaporation of the liquid from the sample inside of a microscope can cause irreversible deformation to the sample, and so masking the real sample properties and possibly leading to the erroneous scientific conclusions. Moreover, the liquid can cause damage to the microscope [16].

1.2 Limitations of TEM and the Development of LCTEM

Transmission electron microscopy (TEM) is the technique of choice for the direct imaging and spectroscopy of individual NPs. TEM was invented in 1931 by Max Knoll and Ernst Ruska, surpassing the resolution using an optical microscope. The first TEMs in the 1930s had a resolution of ~100 nm. By the early 1990s, TEM resolution had surpassed 0.1 nm, making it possible to resolve individual atoms. In 2018 a record resolution of 0.039 nm was achieved [17].

However, TEM is conventionally performed in a high-vacuum environment, which requires dehydrated samples. And there is another universal problem: no matter how often, during the synthesis, sintering, or any other material formation process, the sampling is done, the entire picture is never obtained. Even if the time between each sampling time is decreased, still there is no guarantee that all the necessary information will be obtained - following the Nyquist-Shannon sampling theorem [18]. As quoted by Ngo et al. [19], there is a need to: "End the guessing game". In other words, an analytical technique that can provide continuous observations of matter at a high spatial resolution in real-time, in situ and operating in a liquid environment.

There are two TEM tools currently available to overcome these challenges:

- Environmental TEM
- LCTEM

The environmental transmission electron microscope (ETEM) is a specialized TEM, where the liquid is preserved using differential gas pressure inside the viewing chamber (10^{-3}–$2*10^{3}$ Pa) [16]. However, this technique is not useful for liquids with a low vapor pressure (e.g., water) because they would still evaporate inside the ETEM. Some life-science samples could also not withstand this pressure difference. By engineering the solution for how the liquid is isolated from the vacuum there are two types of ETEM: the differential pumping type and the isolation-film type.

The second approach (and the approach used in this thesis) is the combined use of the transmission electron microscopy technique combined with a liquid cell. In the literature, different names and abbreviations are used for this technique: e.g., liquid TEM [20], liquid cell TEM [21], LCTEM [22], LC-TEM [23], liquid-phase electron microscopy (LP-EM) and in situ TEM [20]. In this thesis the liquid cell transmission electron microscopy (LCTEM) name and abbreviation will be used.

A LCTEM is a specialized holder that can fit in a normal TEM. The liquid is in a closed environment, allowing imaging and spectroscopy of samples in liquid media without altering the vacuum of the microscope [12] by isolating them between two silicon chips containing electron-transparent membrane windows, like silicon nitride (SiN) [24] or graphene [25]. LCTEM, combined with in situ heating and electrochemistry experiments, represents a novel state-of-the-art characterization technique.

In 2012, company Hummingbird Scientific developed the first commercially available flow in situ TEM liquid specimen holder (Evans et al., 2012). In September 2015 the Jožef Stefan Institute (JSI) obtained a LCTEM system from Protochips, Inc. In total, two holders were provided: an in situ heating holder and an in situ electrochemical holder. At that time the heating holder was a prototype, set up for testing at the JSI. It is worth noting that with the manufacturer (Protochips, Inc.) a common research and development program was established. In our part, we have provided a review of the liquid cell's performance and suggestions for further improvements, which were highly beneficial for their development of the next generations of liquid cell holders. And they provided us with

up-to-date improvements of the LCTEM system, enabling our lab (in that time-frame period) to be updated with a cutting-edge LCTEM system.

In recent years, LCTEM gained significant interest in the field of material science as it allows unprecedented, direct high-temporally and high-spatially resolved information about the kinetics of NP nucleation and growth from solutions [26],[12],[13],[27]. LCTEM provides valuable new opportunities for studying the dynamic phenomena of matter in solvated environments [28], at high spatial and temporal resolutions [29],[30]. Recently, materials science benefitted largely from LCTEM for the investigation of atomistic reaction mechanisms at interfaces. With these novel approaches, the mechanism of dynamical processes can be revealed, reaction kinetics can be quantified, and even electrochemical processes can be studied in situ in the microscope. LCTEM was successfully used in many different fields of science, like metallurgy [31], crystallography [32], biology [33], cell biology [34]. LCTEM enabled several studies of the nucleation processes in many different materials, used in different applications. Smeets et al. [35] studied the nucleation of the vaterite polymorph of $CaCO_3$ used for biomedical applications. Ahn et al. [36] observed in situ in real-time the growth and dissolution of silver NPs used in photovoltaics and chemical sensors. Ievlev et al. [37] studied Pt nanocrystals used for catalysis in organic chemistry. Dukes et al. [38] observed the growth of Au NPs for biomedical applications. Chee et al. [31] studied the corrosion of aluminum at the nanoscale. In the past decade several studies were focused on the precipitation and dissolution dynamics of different nanostructured systems by utilizing electron-beam-induced phenomena inside the LCTEM, for example, single metal Cu and Ni nanocrystals [39], Pd dendritic nanostructures [40], alloys such as Ag-Pd or more complex structures like $CaCO_3$ [41], and ceria [42]. One of the most studied material using the LCTEM technique is gold [43],[44],[45],[46], typically used to gain insights into the dynamics of precipitation and dissolution of Au NPs particles in various aqueous environments. The obtained data revealed a complex interplay of thermodynamic and kinetic parameters influencing their final morphologies, leaving the space for the discussion about the influence of the electron-beam-induced phenomena [21], [36], [43], [47].

The power of LCTEM in comparison to the other in situ techniques is the combined spatial and temporal resolution (Figure 1.1). The spatial resolution of LCTEM was defined by Jonge et al. [13] with an approximation that the window material is transparent for typical electron beam energies. The resolution of LCTEM is mainly limited by the chromatic aberration caused by the inelastic scattering of electrons by the liquid [13]. The resolution of LCTEM (d_{TEM}) is defined by the following equation:

$$d_{TEM} = \frac{\alpha\, C_c\, T_h\, k_{water}}{2E} \tag{1.1}$$

where α is the objective semi-angle, C_C is the chromatic aberration coefficient, T_h the thickness of the liquid layer, k_{water} is the inelastic scattering constant for water and E is the beam energy.

If typical values for LCTEM microscopy are inserted into the equation ($\alpha = 10$ mrad, $C_C = 2$ mm, $k_{water} = 4.7$, $T = 1$ µm and $E = 200$ keV): a 4-nm theoretical resolution is achieved [13]. Typical practical resolution in a TEM using a 1-µm-thick layer of liquid is < 10 nm [13]. To further improve the resolution, the thickness of the liquid should be reduced (Figure 1.1). Evans et al. [48] used a 50–100-nm-thick column of liquid in an aberration-corrected scanning transmission electron microscope (STEM) to achieve a resolution of

0.21 nm and to perform the first direct in situ atomic resolution imaging of (PbS) NPs grown from a liquid solution.

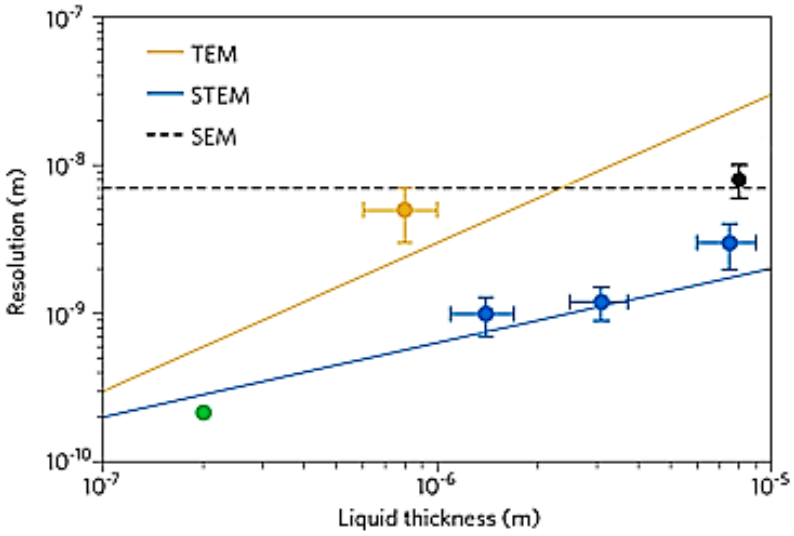

Figure 1.1: Theoretical maximum resolutions for TEM (Transmission electron microscopy), STEM (Scanning transmission electron microscopy), and SEM (Scanning electron microscopy) in relation to the water thickness [13].

1.3 Radiolysis

Dynamic LCTEM shows great potential in probing and understanding the underlying mechanisms during the nucleation and early growth stage of various nanomaterials [36], [41],[6]. It also possesses some great challenges, mainly related to the electron-beam-solvent interaction effects, which can be induced during the LCTEM experiments and can consequently modify the reaction kinetics to such an extent that they cannot be directly related to the corresponding tabletop laboratory experiments [33]. According to Woehl et al. [49] at least three different types of artifacts can occur: 1) the effect of the experimental apparatus, 2) the effect of the indirect interaction between the sample and aqueous chemical species formed by the electron beam, and 3) the effect of the direct interaction between the electron beam and the observed sample. The last two effects are a consequence of the interaction between the water and the electron beam, referred to as water radiolysis.

Radiolysis is defined as the electron-beam degradation of an observed water-based electrolyte through inelastic scattering [43]. Radiolysis is in this case defined as electron-beam-induced degradation of an observed water-based electrolyte through inelastic scattering [43], [50], [51]. Namely, water is bombarded with ionizing radiation (e.g., a beam of high-energy electrons in a TEM), and at first low-energy secondary electrons (SEs) are formed. SEs have enough energy (<100 eV) to interact with water to create new, even lower energy, electrons (<10 eV). These electrons within a picosecond react with water to form a wide variety of ionization and hydration products called the “initial yield”. The newly formed products react within less than 1 µs with electrons and with other products to form a cascade of new products [52]. There are three separate stages (Figure 1.2) in the radiolysis process [53]: 1) physical stage, which lasts up 10^{-15} s, 2) physicochemical stage, which dominates between 10^{-15} to 10^{-12} s and 3) chemical stage, taking place in timescales longer than 10^{-12} s. In the present study, we focused only on the chemical part of the radiolysis in the stage after 10^{-6} s where radiolysis species are homogeneously distributed. In this stage, several different types of reactions occur, namely: 1) reactions between

different radiolysis species, 2) reactions between radiolysis species and gases and 3) reactions between radiolysis species and solute ions. As a result, 16 radiolytic species are known to form in water: solvated electrons (e_h^-), hydrogen radical ($H^\bullet$), hydroxyl radical ($OH^\bullet$), hydrogen (H_2), hydrogen peroxide (H_2O_2), hydroperoxyl radical ($HO_2^\bullet$), hydroperoxyl (HO_2^-), proton (H^+), oxygen (O_2), superoxide (O_2^-), oxygen anion (O^-), ozone (O_3), hydrogen trioxy radical ($HO_3^\bullet$), ozone anion (O_3^-), and hydroxide (OH^-).

It is well documented that these effects are predominately caused by water radiolysis as a consequence of the interaction between water and the energy-intense (80–300 keV) electron beam [49]. Although the LCTEM technique is a very promising technique it also carries challenges that need to be properly addressed and quantified [19],[49]. The main challenge regarding the LCTEM technique is to understand and quantify the influence of the electron beam on the sample [43]. During irradiation of the sample with an electron beam of 200 keV (typical for TEM), the water (usually the main component for NP syntheses) is altered by the water radiolysis [43], which results in the production of various highly reactive radiolysis species that can significantly alter the reaction kinetics [43]. Consequently, these phenomena need to be understood and resolved prior to any successful and reliable interpretation of the experimental results. Different approaches were used in the past to reduce the effects of radiolysis: 1) lowering the electron dose rate [54],[22] 2) using solvents that are not affected by the radiolysis [55] 3) adding scavengers – sacrificial molecules used to oxidize or reduce radiolytic products before reacting with the material of interest [51], 4) running the experiments in the flowing conditions to physically remove the radiolytic products [20]. Among them, the most reactive components are the reducing solvated electrons (e^-_{aq}) with a very negative standard redox potential of E^0=-2.90 V_{SHE} in the range between Li (E^0=-3.04 V_{SHE}) and K (E^0=-2.92 V_{SHE}) and hydroxyl radical ($OH^\bullet$) that acts as a strong oxidizing agent (E^0=+1.8 V_{SHE}).

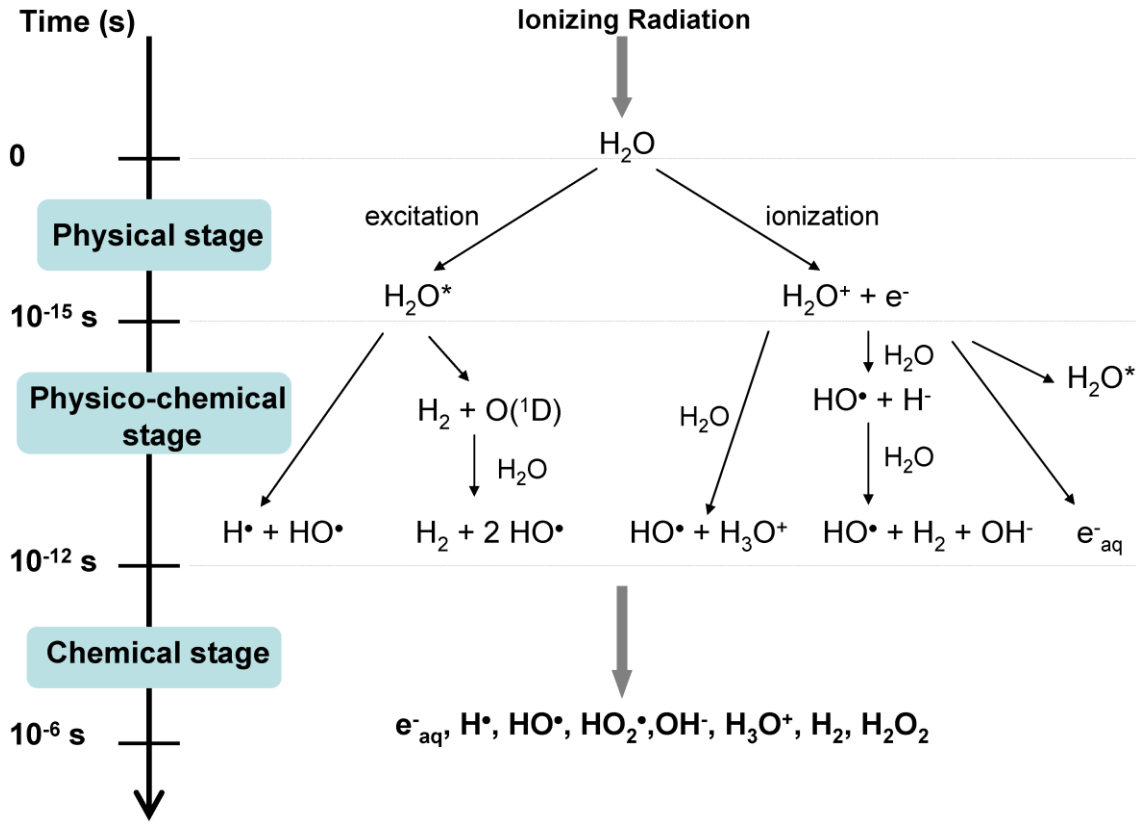

Figure 1.2: Basic radiolysis processes of water in relation with time scale [53].

Due to the extremely localized radiolysis, which is intimately bound to the specimen observation area by the intense electron beam inside the small volume of water-based electrolytes, it is very important that the effects of radiolysis are properly quantified in the overall chemical reactions, which take place inside the liquid cell. Schneider et al. [43] made a pioneering work, by quantifying this very complex process inside the liquid cell using a radiolysis model for the prediction of the concentration of radiolysis species as a function of the dose rate. Although direct imaging of the radiolysis species is not viable in LCTEM, their presence can be to some extent evaluated by the indirect methods, for example, quantifying the nucleation and dissolution of Au and Ag NPs as a function of the concentration of the various radiolysis products that act as oxidizing and reducing species [43] or observing the formation of the gas bubble inside the liquid cell [56].

The electron dose rate (ψ) can be measured in two different units: electrons per square unit area ($e^-/nm^2/s$) or Grays per second (Gy/s). The unit Gy/s is the measurement of the absorbed ionizing radiation energy and it is very regularly used in the field of LCTEM [43],[57],[44],[58]. A further explanation can be found in the article by Schneider et al. [43]. It is especially convenient because of its direct use in radiolysis modeling. The unit [electron $\cdot$ nm^{-2} $\cdot$ s^{-1}.] is more commonly used in the field of conventional TEM. Both units cannot be directly converted since they signify different physical parameters. The approximate conversion equation is given below:

$$\psi\ [\tfrac{Gy}{t}] = \psi\ [e^-/As/t] *\ S\ /q_e \tag{1.2}$$

where ψ is the electron dose rate, S is the stopping power of water (2.78 *10^5 eV/m^2/s/e$^-$), t is time, As is surface area and q_e is elementary electron charge (1.6 * 10^{-19} C).

In the literature, many different dose rates were used (Table 1.1), depending on the nature of the experiment. The development of the novel LCTEM technique enables the deduction of valuable kinetic processes when tailoring the properties of the material on the nanoscale in solvated environments. The beam-driven solvent radiolysis, inevitability connected with the irradiation of a high-energy electron beam during specimen observation, can have a significant influence on the system dynamics. Recent research paradigms suggest that radical-induced redox chemistry can be utilized for the direct investigation of various redox-driven dynamics inside a broad family of functional nanomaterials. Because of this, the interplay between the formation of various highly reactive radiolysis species and nanomaterials of interest needs to be fully quantitatively assessed, to efficiently formulate new strategies of nanomaterials research.

Table 1.1 Table of dose rates and doses used. All data are given for TEM mode, except where it is written that STEM mode was used.

Studied system	**Dose rate ($e^-/nm^2/s$)**	**Dose (e^-/nm^2)**	**Reference**
Liposomes	5–10	5–10	[38]
Gold nanorods		10–320	[38]
$LiFePO_4$, $CuSO_4$	30		[59]
Silver nanocrystals			[60]
Gold nanoparticles		10^5	[61]
Cells		740–7400	[34]
Gold nanorods		10 - 320	[38]
Liquid crystals	25	162	[62]
Pd salt		10 (in STEM)	[63]
Eukaryotic cells in liquid		900	[64]
E-coli bacteria, mammalian cells		10^4	[64]
Gold nanoparticles in live cells		30	[34]
Gold nanorods	$1.2*10^8$		[65]

1.4 Nanoparticles Used in This System: Synthesis and Applications

A nanoparticle (or nanopowder or nanocluster or nanocrystal) is a microscopic particle with one or more dimensions at the nanoscale (at least one dimension < 100 nm). A nanomaterial is a material having a physicochemical structure on a scale greater than typically atomic/molecular dimensions but less than 100 nm (nanostructure), which exhibits physical, chemical, and/or biological characteristics associated with its nanostructure [66].

In the thesis, three different systems with different nucleation mechanisms were studied using the LCTEM technique. The first was Au NPs, which are known to precipitate using a single or multistep nucleation mechanism [67]. The second was yttrium hydroxide NPs, as a model phosphor oxide material, which have complicated nucleation mechanism via an

indirect path combined with the temperature-dependent decomposition of urea [68]. And the third was Fe NPs as a typical example of electrochemical synthesis [69].

1.4.1 Gold Nanoparticles

Gold NPs were among the most studied nanomaterials, first synthesized by Michael Faraday in the 1850s [70]. Since then many different types (Figure 1.3) of synthesis methods and types of gold NPs were invented [71].

Gold NPs are versatile engineering material, which, is among many other applications [72], are also used in experimental cancer treatments where the gold nanoparticle`s photothermal effect is employed [73]. For that reason, gold nanoparticle nucleation processes and chemical reaction kinetics need to be understood in situ in a liquid at the elevated temperature conditions [9].

Gold NPs were among the first materials analyzed using the LCTEM method [64]. Since then they were involved in numerous LCTEM studies. Chen et al. [74] and Jungjohann et al. [75] investigated the movement of gold NPs in solution. Nielsen et al. [76] observed Au nucleation and noted radiolysis effects. Wang et al. [77] observed the interactions of Au NPs with cells. Schneider et al. [43] reported the growing and etching of Au NPs in situ in a liquid. The reaction pathways of these mechanisms were explained by Hutzler et al. [78].

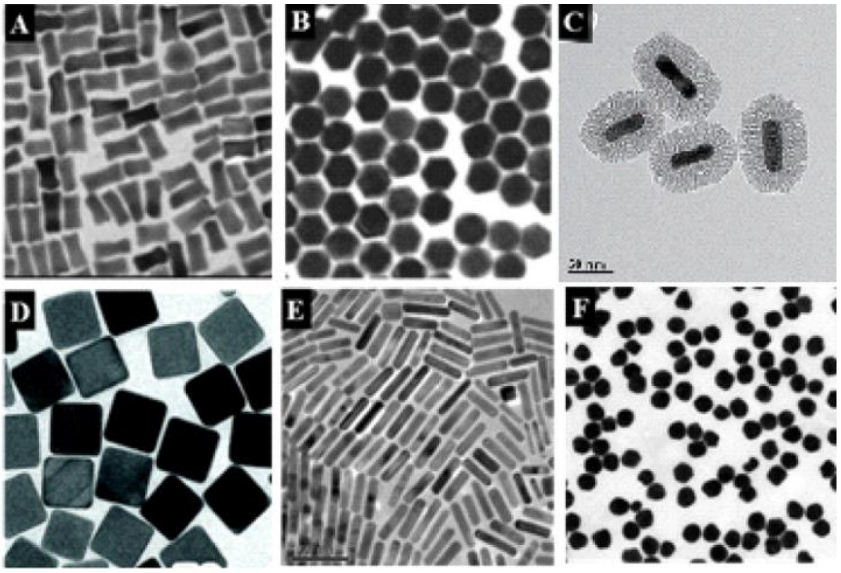

Figure 1.3: Different types of gold NPs: a) Gold nano bones. (b) Gold nanohoneycombs. (c) Mesoporous silica-coated gold nanorods (d) Gold nanocages. (e) Gold nanorods. (f) Gold nanospheres [77].

1.4.2 Yttria Nanoparticles

Yttria has outstanding properties such as a high melting point, excellent chemical stability, and low volatility in a vacuum [79]. In the last few decades, yttrium oxide has most commonly been used as a sintering agent for densifying ceramics and, when doped with Eu or Tb, as a phosphor material (Figure 1.4) [80], [81]. Yttrium oxide is the most thermodynamically stable oxide available [82].

Yttrium oxide NPs are a host for heavy-rare-earth elements (Yb^{3+}, Eu^{3+}) and are known to be an efficient up-conversion phosphor material with a great potential ranging from therapy [83] and sensing for drug delivery to photovoltaic applications [84]. Yttrium oxide has excellent chemical stability, low volatility in a vacuum, and a high melting point [85]. Optical properties depend on the particle size and morphology [86]. Therefore, the efficient

use of yttria in the form of yttria-based phosphor precursor NPs is related to the understanding of the synthesis and early growth stage kinetics of yttria precursors, formed by the precipitation from the saturated solutions. In contrast to various analytical methods, where the kinetic data are deduced from large sampled volumes, the LCTEM technique offers the unique possibility to study the spatial and temporal evolution of NPs one-by-one, facilitating a complete reconstruction of early-stage events that are vital for the formation of the final products.

The formation of yttria NPs is controlled by the decomposition rate of urea. It is known that the decomposition rate of urea is very well temperature controlled, especially above 80 °C. For example, the decomposition constant of urea in the water at 25 °C is calculated to be 6.65 x 10^{-8}/s, which is about 1/15000 of its value at 90 °C [87]. The activation energy for this decomposition process is 135.5 kJ.

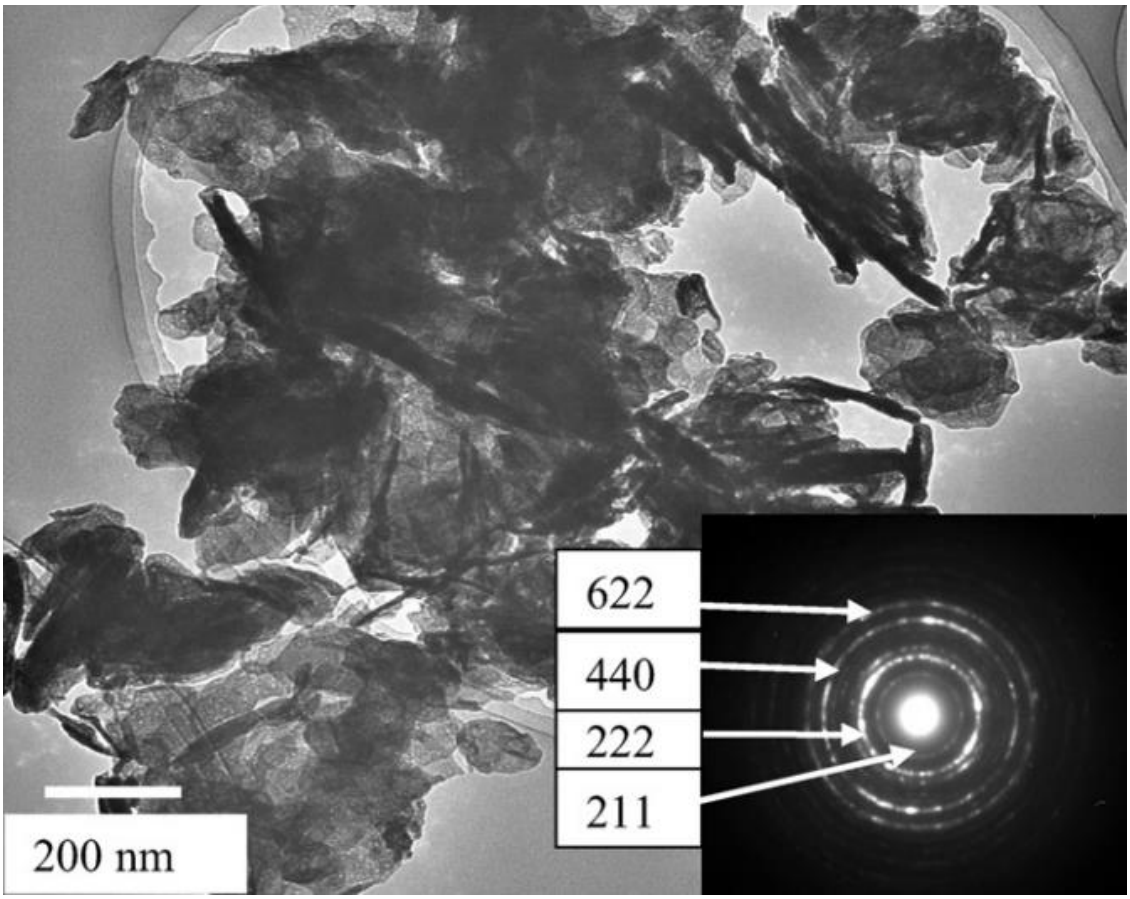

Figure 1.4: TEM micrograph of yttrium oxide NPs doped with Eu for phosphor applications [81].

1.4.3 Iron Nanoparticles

The synthesis of iron (Fe) NPs and their dispersion in various liquid media has been one of the most attractive goals in magnetic nanomaterial research. Iron NPs are a class of ferromagnetic material with a high magnetic-moment density. It is reported that iron NPs in the size range below 20 nm are in the superparamagnetic regime [88]. Fe NPs have important applications in bioseparation, biosensing, drug delivery, experimental cancer treatments [89], and MRI contrast enhancement [88].

Fe NPs are typically prepared using e.g. the thermal decomposition of iron pentacarbonyl ($Fe(CO)_5$) [90], the reductive decomposition of iron(II) bis(trimethylsilyl)amide ($Fe[NSi(CH_3)_3]_2]_2$) [91], and the reduction of iron(III) acetylacetonate ($Fe(acac)_3$) or other iron salts [88].

Most commonly Fe exists in the body-centered cubic (BCC) (ferrite or α-Fe) atom arrangement (Figure 1.5a). However, several studies report that Fe NPs can also crystalize in the face-centered cubic (FCC) crystal structure (austenite or γ-Fe) with interesting magnetic properties (Figure 1.5b).

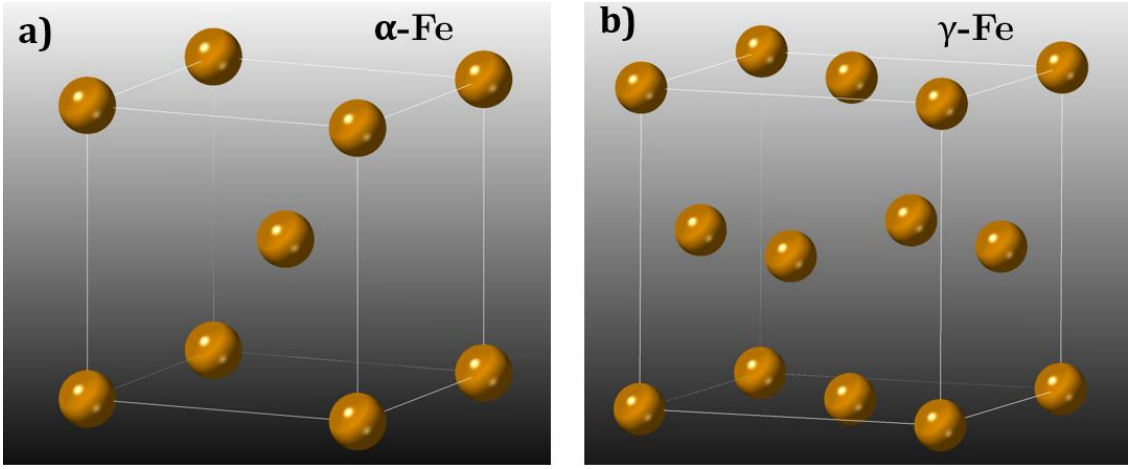

Figure 1.5: Unit cells of two iron allotropes: a) α -Fe and b) γ-Fe.

1.5 Mechanisms of Nucleation and Growth of Nanoparticles

Nucleation is a mechanism in which a new solid thermodynamic phase appears from a liquid phase. Through the process of nucleation, a first random formation of a distinct thermodynamic new phase, referred to as a nucleus, irreversibly grows into the larger sized stable nucleus, i.e., a NP, within the body of a metastable parent phase. Precipitation is a chemical process in which a solid substance is produced from a liquid through the process of nucleation [92]. Various thermodynamic and kinetic parameters will influence the final formation of stable NPs, which can be to a first approximation explained by the Classical Nucleation Theory (CNT). CNT is one of the scientific theories used for the thermodynamic description of the nucleation of NPs. CNT is divided into two mechanisms: homogenous nucleation and heterogeneous nucleation. Homogenous nucleation occurs away from the surface, and heterogeneous nucleation occurs at nucleation sites: e.g., surfaces, pre-existing particles [93]. The most important concepts of CNT, which allow controllable experiments, for example, precipitation synthesis, are excess Gibbs free energy, critical radius, cluster size, and nucleation rate. These parameters can be theoretically and experimentally assessed utilizing LCTEM. It is important to mention that although CNT offers an excellent starting point for understanding the nucleation and early growth stages of NPs, several recent studies, especially related to LCTEM experiments [93], indicate that the formation of a solid from a liquid is a complex process that can undergo several nucleation pathways well beyond the CNT concepts, for example: the LaMer mechanism [67], coalescence [96], oriented attachment [97], Ostwald ripening [98] and self-assembly [99].

The LaMer mechanism is described as the nucleation of NPs that has three distinctive steps [67]. In the first step, a rapid increase in the concentration of free monomers in the

solution occurs, which is followed by a sudden burst nucleation on a relatively short timescale since the concentration of monomers is quickly used. In the last step, there are almost no free monomers in the solution, and consequently, the nucleation rate quickly drops. Coalescence describes how smaller crystals are merged into larger ones. Oriented attachment is a similar process to coalescence, but with a perfect crystallographic alignment of the crystals. This happens either due to Coulomb interaction or the presence of Van der Waals forces at the particle's surface. Ostwald ripening is a thermodynamically controlled phenomenon where larger, energetically favorable, particles will grow on behalf of smaller particles. This is accompanied by the dissolution of small crystals and the redisposition of the dissolved matter on the existing surfaces of a larger solid [67]. Self-assembly is a process in which pre-existing disordered components form an organized structure without external interaction [100].

For the sake of simplicity, we will concentrate on CNT, applying a homogenous nucleation hypothesis, where it is assumed that spherical shaped nuclei crystalize from the supersaturated liquid, with sharp interfaces between phases and well-defined surfaces. For a simple one-atom metallic system, under the right conditions, solute atoms will be reduced into their zero-valence state, which will collide, thus forming meta-stable pre-nucleation clusters or embryos. As embryos are not yet in thermodynamic equilibrium, they will randomly dissolve and pre-nucleate. The excess Gibbs free energy of cluster formation is given by:

$$\Delta G = \tfrac{4}{3}\pi r^3 \Delta G_v + 4\pi r^2 \gamma \tag{1.3}$$

where ΔG is the Gibbs free energy, ΔGv is free energy per unit volume, r is the radius of a spherical nucleus and γ is the surface energy per unit area

The reduction of the excess Gibbs free energy of cluster formation (ΔGr) represents a driving force for both nucleation and growth. It is composed of two competing terms; surface free energy, which is positive (unfavorable), and is related to the creation of a new surface, i.e. the interface between solute clusters and solution. The other term is defined as a volume free energy related to the bond formation within the volume of the cluster. The sign of this term will depend on the S value. If S<1, the solution is not oversaturated, the cluster might form but with further growth will become increasingly thermodynamically unstable, i.e. the term is positive, preventing the formation of nuclei. When the solution is saturated (S>1), the excess Gibbs free energy will start to decrease with the increase of cluster size, providing the initial driving force for nucleation and growth, as shown in Figure 1.6. A detailed graphical analysis implies that ΔGr will first increase and start to decrease at a critical cluster radius (r*). Mathematically speaking, the critical cluster radius is defined when dΔGr/dr equals zero, which is at the maximum excess free energy, ΔG*. This is the critical energy for nucleation that the system must overcome to form a new nucleus. A cluster smaller than r* is therefore thermodynamically unstable and will tend to dissolve. Above r*, clusters are stabilized and are now called nuclei that will continue to grow simultaneously and form NPs. The critical size of the nucleus represents the limit of how small NPs can be synthesized. Typically, the solute concentration and the temperature of the system is varied, which has a direct influence on the excess volume of free energy (ΔGv) and the surface free energy (γ), respectively. The r* and Δ G* are defined by the following equations:

$$r^* = \frac{2\gamma V_m}{RTlnS_r} \tag{1.4}$$

$$\Delta G^* = \frac{16\pi\gamma^3 V_m^2}{3(RTlnS_r)^2} \tag{1.5}$$

where r^* is the critical size of the nucleus, γ is surface energy per unit area, V_m is molar volume of bulk crystal, R is ideal gas constant, S_r is the ratio between solute concentration at saturation, T is temperature and ΔG^* is the critical free energy.

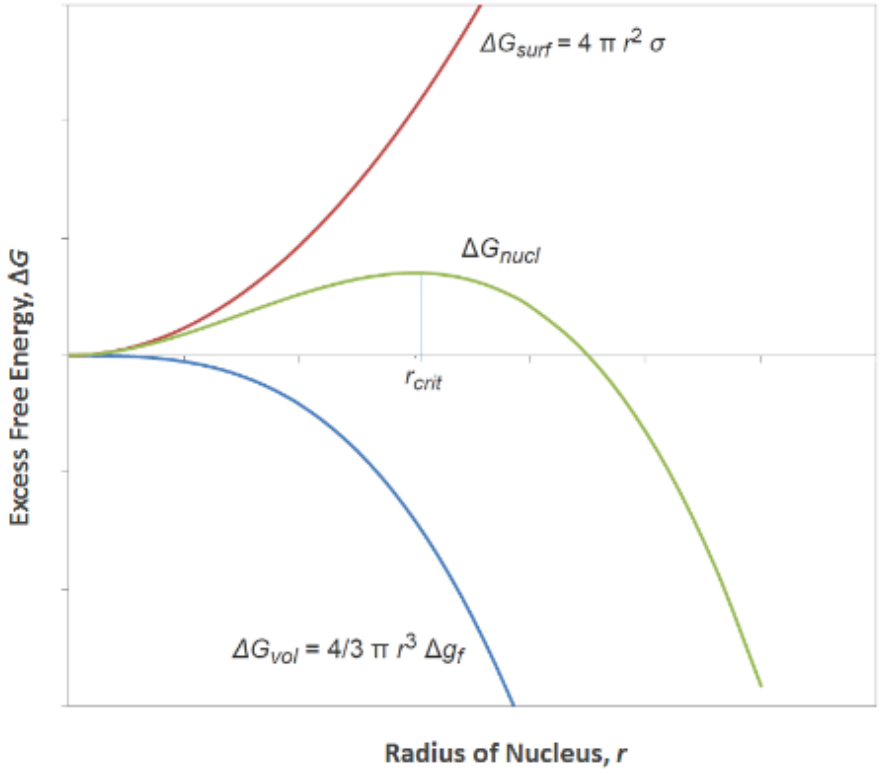

Figure 1.6: Graphical representation of the overall excess Gibbs free energy (ΔGr) as a function of cluster size r (Adapted from [101]).

Further, the number of clusters that reach the critical size (Nr*) and consequently, the nucleation rate, which is defined as ΔNr*/dt are described by the following equations:

$$N_{r^*} = N_A[A]_{eq}S_r\ exp(-\tfrac{\Delta G^*}{RT}) = \ N_A[A]_{eq}S_r\ exp\left(-\tfrac{16\pi\gamma^3V_m^2}{3(RT)^3(lnS_r)^2}\right) \tag{1.6}$$

$$\tfrac{dN_{r^*}}{dt} = f_0N_A[A]_{eq}S_r\exp(-\tfrac{\Delta G^*}{RT}) = \ f_0N_A[A]_{eq}S_r\exp\left(-\tfrac{16\pi\gamma^3V_m^2}{3(RT)^3(lnS_r)^2}\right) \tag{1.7}$$

where N_{r^*} is the number of clusters that reach critical size, N_A is Avogadro's constant, A_{eq} is the solute concentration at equilibrium and t is time.

In contrast to homogeneous nucleation, heterogeneous nucleation does not occur spontaneously. It is triggered by foreign species or surfaces that act as nucleation centers with low activation energy and results in lowering the overall Gibbs free energy (Fig. 1.7). Heterogeneous nucleation occurs at preferential sites, such as phase boundaries, impurities, dust, or on surfaces [102]. Consequently, the critical energy for nucleation is lower than that of the corresponding homogeneous nucleation, resulting in a faster nucleation process. The Gibbs free energy for heterogeneous nucleation is proportional to the homogenous nucleation multiplied by a numerical value lower than Equation 1.9, which is a function of

the contact angle describing the geometric relationships between the heterogeneous nuclei and the corresponding substrate surface onto which it is nucleating by means of the wetting (contact) angle θ, as shown in the equations below:

$$\Delta G_{heteregenous} = \Delta G_{homogenous} * f(\theta) \tag{1.8}$$

$$f(\theta) = \frac{2-3cos\theta+cos^3\theta}{4} \tag{1.9}$$

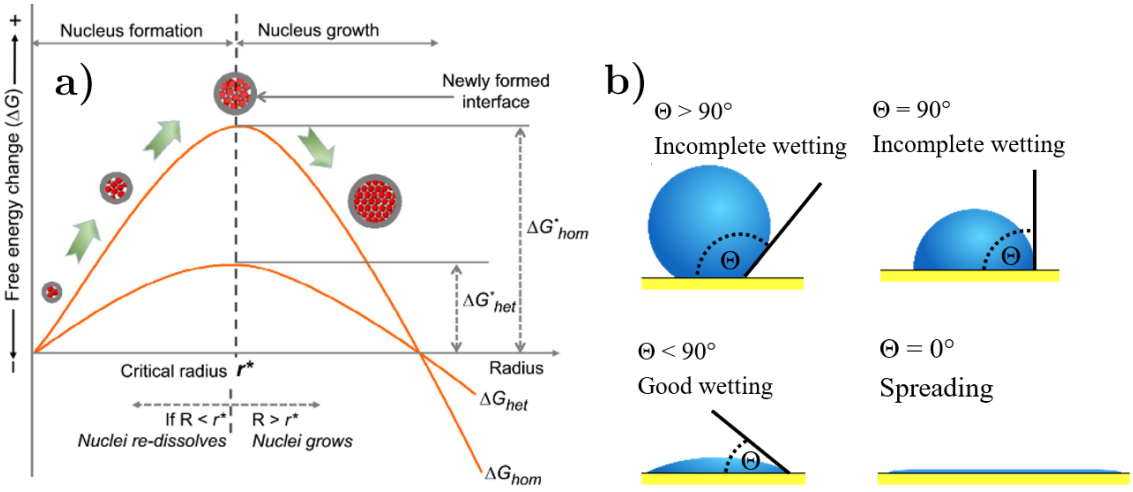

Figure 1.7: a) Difference in the Gibbs free energy needed for nucleation between homogenous and heterogeneous nucleation [103], b) Four droplets on the substrate surface with different contact angles. Note that by decreasing the contact angle from 180° to 0° the Gibbs free energy for heterogeneous nucleation will be lower when compared with that of homogeneous nucleation.

As an example, for θ=180°, there will be no wetting of the surface, therefore preventing nucleation at the surface, implying homogeneous nucleation. In contrast, when θ = 0° full wetting is observed, indicating a minimum barrier for heterogeneous nucleation at the surface [103]. It is worth pointing out that the critical nucleation radiuses (r*) remain unchanged for both heterogeneous and homogenous nucleation. However, the volume V_β of the nucleus in heterogeneous nucleation can be significantly lower than that of the (spherical) nucleus for the case of homogenous nucleation, as a result of the wetting angle affecting the shape of the nucleus, as given below:

$$V_\beta = V_{\beta\,(homogenous)} * f(\theta) = \frac{4\pi r*^3}{3} * \frac{2-3cos\theta+\cos\theta^3}{4} \tag{1.10}$$

Although these thermodynamic and kinetic parameters (ΔG*, r*, Nr*, ΔNr*/dt) are extremely important to quantify as they govern the nucleation process of solids (NPs) from the solution, they are often difficult to assess. In this respect, LCTEM offers the means for the direct evaluation of the parameters mentioned above, therefore providing better control over the processes that govern the NPs synthesis.

1.6 Electrochemistry in LCTEM

Electrochemistry is a sub-discipline of physical chemistry that is based on electron transfer reactions at the solution/electrode interface, i.e., redox reactions. The subject is concerned with the relationship between electrical and chemical energy and the conversion of one to the other [104].

1.6.1 Fundamentals of Electrochemistry

Electrochemical processes are comprised of redox reactions, where the charge (electron) transfer between electrodes (typically metallic) and reactant molecules (usually in a solution phase) occurs across the interface. To ensure the electro-neutrality of the system, at least two electron-transfer reactions take place, i.e. reduction and oxidation. The reduction is determined by the gain of the electrons and the oxidation by the loss of the electrons [105]. Oxidation and reduction always take place at the same time, e.g., when one substance, i.e., atom or molecule, oxidizes (its oxidation state increases), at the same time the other substance is reduced (its oxidation state decreases). For that reason, the reaction is named redox reaction [106],[104]. An example of a redox reaction is described by the following equation:

$$X^{2+} + Y^{4+} \leftrightarrow X^{3+} + Y^{3+} \tag{1.11}$$

In this redox reaction, a substance (e.g., atom or molecule) that donates electrons to another species is called a reducing agent or reductant (X^{2+}) and the substance that has a strong affinity for electrons is an oxidizing agent or oxidant (Y^{4+}). The redox reactions can be divided into two half-reactions and thus show which of the substances gains and which loses electrons [107].

$$\text{Oxidation: } X^{2+} \leftrightarrow X^{3+} + e^{-} \tag{1.12}$$

$$\text{Reduction: } Y^{4+} + e^{-} \leftrightarrow Y^{3+} \tag{1.13}$$

1.6.2 Electrochemical Cells

The oxidation and reduction reactions can be studied by measuring the potentials of an electrochemical cell. An electrochemical cell (Figure 1.8) is a device that generates or consumes electrical energy from redox reactions (e.g., spontaneous or non-spontaneous); it consists of two electrochemical half-cells (Figure 1.8): each composed of a conductor called an electrode which is immersed in an electrolyte solution. The solutions surrounding the electrodes are different and have to be separated in order to avoid a direct reaction between reactants [107]. The half-cells are separated with a salt-bridge that enables the conduction of electricity from one to another electrolyte solution (as seen in Figure 1.8). At a certain concentration of electrolyte and temperature, the half-cell has an exact electrode potential. An electrode potential is defined as the potential of a half-cell in which the electrode in question is a first electrode and the standard hydrogen electrode (SHE) is a second electrode. By convention, the SHE is defined with an absolute potential of zero (E= 0.0 V [104]), at a standard state with ions at an effective concentration of 1 mol/dm^3 and at a pressure of 1 atm [108]. This makes it possible to conveniently report the potential of the other half-cell.

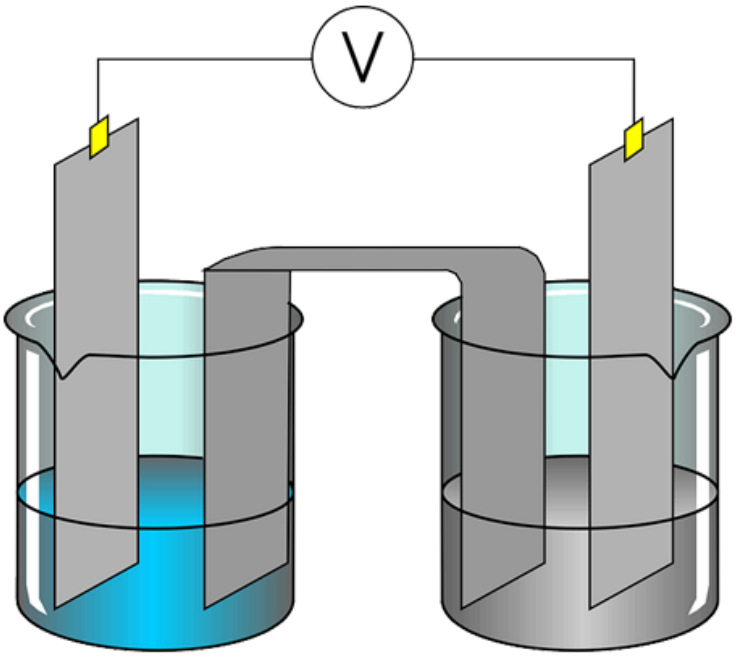

Figure 1.8: Electrochemical cell composed of two half cells, each consists of an electrode and solution that are separated with a salt bridge [109].

The potential that depends upon the relative concentrations of the oxidized (Y^{4+}, see reduction reaction) and reduced (Y^{3+}, see reduction reaction) species, reaches an equilibrium value if no current flows through the electrochemical cell. Nernst showed a mathematical expression for the potential under equilibrium conditions. The established Nernst equation is expressed with the following [105], [110]:

$$E_e = E^0 + \frac{RT}{nF} ln \frac{[Oxidized\ species]}{[Reduced\ species]} \tag{1.14}$$

where E_e is an equilibrium potential [V], E^0 is a standard electrode potential [V] for the case measured relative to the SHE. [Oxidized species] and [Reduced species] are the concentrations of the given species [mol/L=M]. R is the universal gas constant [8.314 J mol/K], T is the temperature [°C], n is the number of transferred electrons, and F is the Faraday constant [96,485 C/mol] [105], [107].

The measurements of electrochemical processes are more complicated if the current flows. The current passes through the electrochemical cell because of the spontaneous or non-spontaneous electrochemical reactions. A redox reaction is spontaneous if the standard electrode potential for the redox reaction is positive. Such a reaction can be used to produce electricity by chemical energy. The type of electrochemical cell for this system is called a galvanic cell. On the other hand, a redox reaction is non-spontaneous if the standard electrode potential for the redox reaction is negative. Such a system enables the conversion of electricity into chemical energy under applying an external source of electrical energy, i.e., electrolysis. The energy-consuming device for this system is called an electrolytic cell. In this thesis we are mainly focused on the electrochemical processes that occur in an electrolytic cell. Performing an electrochemical experiment based on electrolysis requires the cell composed of two or three separate electrodes. The two-electrode system includes a

working electrode (WE) and a counter electrode (CE), while a three-electrode system also includes a reference electrode (RE). The working electrode (i.e., indicator electrode) and counter electrode (i.e., auxiliary electrode) are the electrodes where the redox processes under study occur. The working electrode is typically a cathode where the reduction takes place. The counter electrode helps pass the current flowing through the cell (the current travels between the working and counter electrodes). Typically, no processes of interest occur at the surface of the counter electrode (an example is Pt wire) [110]. The reference electrode maintains a constant and stable potential by which the potential of the working electrode can be monitored. In principle, two electrodes are enough for electrochemical measurements and [107], [111] quantifications. However, the use of three electrodes allows more accurate applications of the potential and currents. When the potential is measured between the working and reference electrodes, the potential drop can be observed. It is defined as the product of the current passing through the cell and the solution resistance. For the systems where the potential drop is small (< 2 mV), the two-electrode system can be used. If the potential drop is large (> 2 mV), a three-electrode configuration must be used. The three-electrode configuration reduces the potential drop because the majority of the current flows between the working and counter electrodes [107], [112].

The measurements of the electrochemical processes in the electrolytic cell can provide detailed information about the mechanism of the redox reactions. The methods that are normally used for studying the electrode processes are the potential sweep methods, the pulse techniques, the impedance methods and the steady-state methods [104], [110].

1.6.3 Cyclic Voltammetry

Cyclic voltammetry (CV) is one of the voltammetric techniques that is usually employed in electrochemical investigations. It can provide quick information about the electrochemical reactions. The CV experiments rely on the diffusion of species to the electrode surface. The shape of the curve in the CV voltammogram (Figure 1.9) can be understood in the following way [107]. Once the potential is swept from its initial value (V_1) and when the equilibrium at the surface starts to alter, the current begins to flow/increase [111]. The current peak ($i_{p,a}$) is observed at the potential of $E_{p,a}$, and is ascribed to the oxidation of species in the electrolyte. Once the diffusion of the electrolyte species becomes limited (slower), the current starts to drop. The current peak observed in the direction from V_1 to V_2 (i.e., forward direction/scan) is positive. When the potential V_2 is reached, the potential is reversed to the opposite direction (reverse direction/scan). The maximum current ($i_{p,c}$) at the potential of $E_{p,c}$ observed in the opposite direction (from V_2 to V_1) represents the reduction of the electrolyte species. Further potential scanning to V_1 causes a decrease in the current value due to the limitation of the electrolyte species at the electrode surface. The current observed in the direction from V_2 to V_1 is negative [105]. The cycle (forward and reverse) can be repeated.

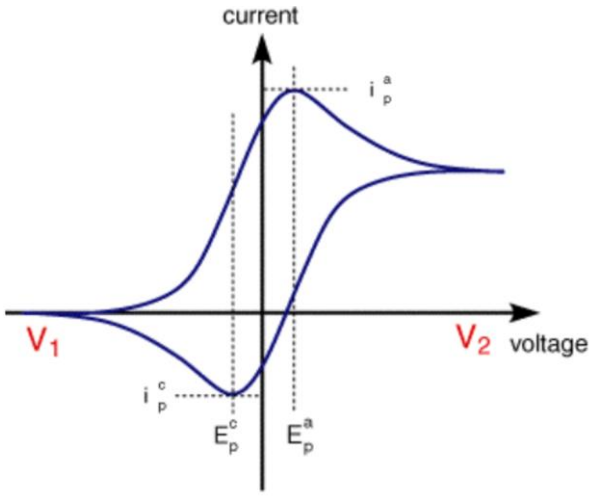

Figure 1.9: Cyclic voltammogram for a reversible system b) relation of scan rate to peak current [113].

1.6.4 Electrochemical Deposition of Metals (e.g., Fe)

Electrodeposition is a unique technique in which different types of nanomaterials can be processed, including metals, polymer, ceramics. It has many advantages, such as low cost, ability to produce coatings on various substrates and structural features with sizes ranging from nm to µm with high industrial applicability. In this thesis, we are mainly focused on the electrodeposition of Fe NPs. The electrodeposition of metals is the electrolysis process, where the main interest is a cathode reaction (reduction), which presents a reaction of charged particles (electrons and metal ions) at the interface between a substrate and a liquid solution, as presented by the following equation 1.15 [111], [114]:

$$M^{n+}(aq) + n\ e^{-}\ (electrode) \leftrightarrow\ M_{solid} \tag{1.15}$$

It is typically performed in a three-electrode cell containing a RE, an anode as a CE and a cathode as a WE, where the electrolyte and deposition parameters control the chemical composition, morphology and porosity of the deposits.

The initial experimental conditions for the electrodeposition of Fe, presented in this thesis, can be deduced from the Pourbaix diagram (Figure 1.10) of Fe, which is similar to phase diagrams and shows phases that are stable at different redox conditions. The Pourbaix diagram or Eh/pH diagram depicts the electrochemical potential versus pH for a given temperature, pressure, and dissolved ion concentration [107]. In this thesis, it will be used for the interpretation of the stability of Fe phases (Figure 1.10). The vertical axis is labeled E_H for the voltage potential in relation to the standard hydrogen electrode (SHE) as calculated by the Nernst equation and the horizontal axis represents the pH values. The lines in the Pourbaix diagram show the equilibrium conditions, where the activities are equal, for the species on each side of that line. On either side of the line, one form of the species will be thermodynamically stable [111]. The stability conditions of the phases are, in many cases, limited by the stability of water. For that reason, lines with a stability regime of water are usually superimposed in the diagrams. More stable species tend to occupy a larger area in the diagram.

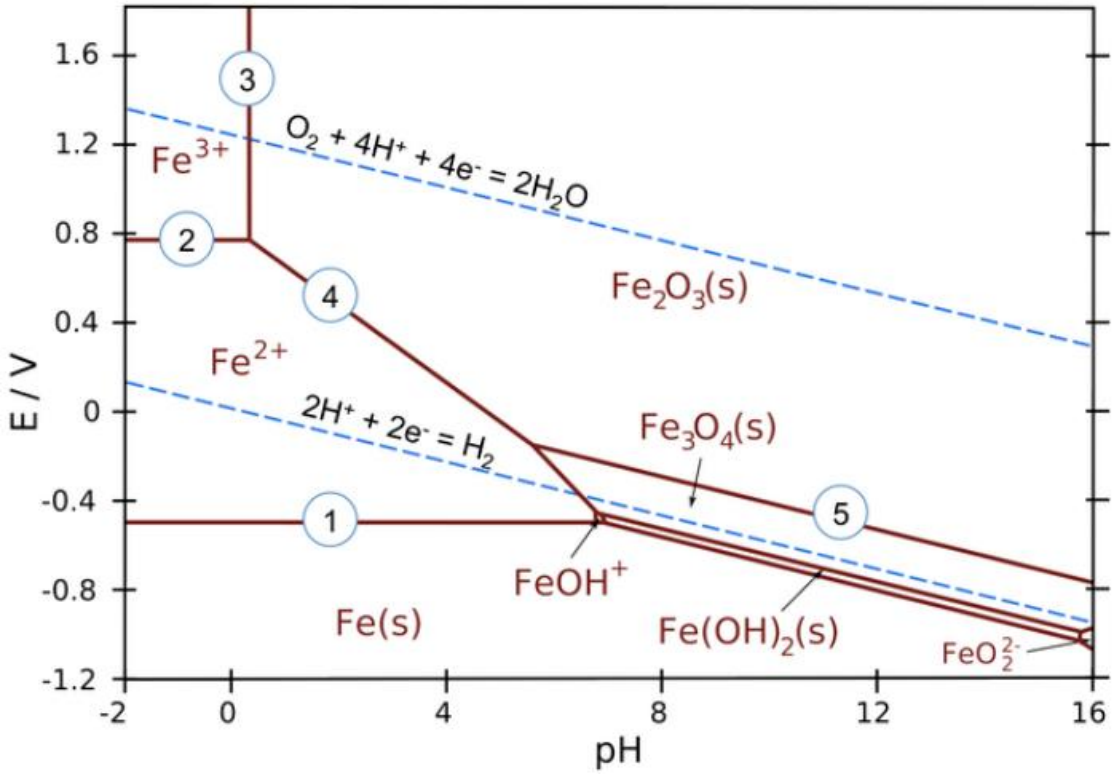

Figure 1.10: Pourbaix diagram of Fe at an ionic concentration of 1 mM. Areas in the Pourbaix diagram mark regions where a single species (e.g. Fe^{2+}) is stable. Lines mark places where two species exist in equilibrium. Pure redox reactions are horizontal lines - these reactions are not pH-dependent. Pure acid-base reactions are vertical lines - these do not depend on potential [111], [115].

In conclusion, the electrochemistry has become an important approach in a wide variety of industrial processes; e.g., galvanization [116], protective coatings [117], batteries [118] and fuel cells [119]. All these processes rely on understanding the electrochemical parameters controlling the structure and chemistry of the deposit. In view of this, the LCTEM technique enables in situ studies of the electrochemical processes, for example, it makes it possible to monitor the electrochemical deposition parameters with sub-nanometer precision at a high temporal resolution, and thus combines the structure-chemistry properties of the deposits with the electrochemical data under dynamic conditions [120], [121]. So far, the LCTEM was used for the in situ electrochemical investigation of Li-ion batteries [122][123][8], [124][125], electrochemical processes in storage systems [126], studies of ionic liquids [127], fuel cells [122][128][129], corrosion [31], lithiation [130] and graphene [131].

Chapter 2

Aims and Hypothesis

Controlling the synthesis parameters, especially in the early stage of NP growth, is of vital importance to obtaining high-quality NPs. Existing ex situ characterization techniques often lack quantitative data about the NP nucleation and early growth stages, which are crucial for a determination of the comprehensive NP synthesis mechanisms. In view of this, the LCTEM technique, combined with in situ heating and electrochemistry experiments, represents a novel state-of-the-art characterization technique. In recent years, this technique gained significant interest in the field of material science as it allows unprecedented, direct high-temporally and high-spatially resolved information about the kinetics of NPs' nucleation and growth from solutions [12],[13],[27]. However, in the current state, the LCTEM method is mainly used in a qualitative manner, which severely limits the quality of the data interpretation. Because of this, in the thesis the procedures for all the relevant experimental parameters, as well as the radiolysis species formed during the specimen observation, were carefully evaluated, and quantitatively determined.

2.1 Aims

The main aim of this Ph.D. is to develop and verify experimental procedures, which will enable controlled LCTEM experiments for in situ dynamic investigations of the nucleation and growth phenomena of NPs in aqueous environments with high spatial and temporal resolution. For that purpose, the liquid cell with heating capabilities will be implemented for studying Au NPs and Y hydroxide NPs nucleation and early growth, while electrochemical cells inside the TEM will be used for studying the early processes of electrochemical deposition of Fe NPs. The influence of radiolysis on the kinetics of NPs' formation in the LCTEM during the specimen observation will be modeled and quantified.

In the thesis, three different systems with different nucleation mechanisms were studied using the LCTEM technique. The first was Au NPs, which are known to precipitate using a single or multistep nucleation mechanism [67]. The second was yttrium hydroxide NPs, which have a complicated nucleation mechanism via an indirect path with the dissolution of urea [68]. And the third was Fe NPs, which are a typical example of electrochemical synthesis [69].

Goal 1

The first goal of the dissertation is to establish an LCTEM experimental setup for assessing the data, to quantify the nucleation and growth kinetics during the in situ synthesis experiments. LCTEM experiments proved to be technically challenging. Many parameters, such as the quality of the SiN window, associated wetting properties, window bulging, and contamination of the solution need to be optimized. Therefore, the procedure for the optimal assembly of the liquid cell will be established, making it possible to achieve reliable, comparable, and repeatable results.

Goal 2

Radiolysis phenomena in the liquid cell are directly related to the electron dose rate. Therefore, an accurate procedure will be established for the precise measurement of the electron dose rate, making it possible to obtain information that will be fed into the newly built radiolysis model.

Goal 3

A new kinetic radiolysis model optimized for LCTEM experiments will be developed. It will be used for the prediction of the growth/dissolution of metal NPs (Au) as a function of temperature and electron dose rate. Consequently, procedures for identifying radiolytically induced phenomena inside the liquid cell will be established. That will include the prediction of H_2 and O_2 bubble formation during LCTEM experiments.

Goal 4

Several different experimental paths will be used for the in situ synthesis of NPs. The synthesis of Au and Y hydroxide NPs will be controlled by changing the process parameters (e.g. temperature) and parameters associated with radiolysis (e.g. electron dose rate). The second synthesis path will include the in situ electrochemical deposition of Fe NPs. The LCTEM technique will be used to directly observe the effect of these parameters on the kinetic behavior during the NPs' nucleation and growth with high spatial and temporal resolution.

Goal 5

From these experiments, the information about the time-dependent growth of NPs will be extracted. The size and volume of the NPs will be measured. The obtained data will be compared and discussed against the existing nucleation theories.

2.2 Hypothesis

Hypothesis 1

Our first hypothesis is that the LCTEM experiments will provide information about the nucleation and growth kinetics of NPs from aqueous solutions and during the electrochemical deposition. Hypothetically, different nucleation pathways will be possible to identify directly.

Hypothesis 2

We hypothesize that with the LCTEM technique it is possible to deposit and dissolve Au NPs in aqueous solutions, which provides a means for quantifying the influence of radiolysis to the heat-induced gold precipitation experiment.

Hypothesis 3

We hypothesize that it is possible to directly observe the nucleation phenomena of Fe NPs using the in situ electrochemistry approach in the TEM, which provides dynamic data during the early stages of electrodeposition.

Hypothesis 4

We further hypothesize that it is possible to develop a kinetic model for radiolysis in the TEM, to differentiate between radiolytically induced and thermally induced phenomena inside the liquid cell.

Hypothesis 5

We hypothesize that the kinetic model for radiolysis can be further expanded into the temperature-dose rate redox potential diagrams for various noble metals (Au) to predict growth/dissolution experimental conditions for noble metals.

Intentionally left blank

Chapter 3

Materials and Methods

3.1 Characterization of Samples

3.1.1 Electron Microscopy

3.1.1.1 Transmission Electron Microscopy Characterization

The JSM-2100 LaB_6 TEM at the Center for Electron Microscopy and Microanalysis (CEMM) at JSI, Ljubljana, Slovenia, was used for the analyses. The TEM was operated at a 200-kV accelerating voltage. The TEM was equipped with a selective-area electron diffraction (SAED) and JED 2300 energy-dispersive X-ray spectroscopy (EDS) detector. A field-emission-gun (FEG) (S)TEM JSM-2100 at the Institute of Low-Temperature Science at the Hokkaido University, Sapporo, Japan was also used in the research of LCTEM artifacts.

Experimental images and videos were recorded using an Orius Model 832 SC1000 CCD camera at 30 frames per second and a theoretical pixel resolution of 0.5 nm. The resolution of the camera was 2672 x 4008 pixels (10.6 MP) with a pixel size of 9 x 9 µm. The video was recorded with a resolution of 650 x 480 pixels using VirtualDub software, which directly captures video from the camera. TEM observation mode (instead of a STEM) was selected to achieve a uniform and parallel illumination of the analyzed area with the electron beam. Imaging and recording of videos of the LCTEM experiments were performed on the exit side of Si_3N_4 windows, where the spatial resolution in TEM mode is known to be the highest [13].

3.1.1.2 Scanning Electron Microscopy Characterization

Scanning electron microscopy (SEM) analysis of the NPs was performed using a FEI Helios Nanolab focused ion beam (FIB)/SEM at the Center of Excellence in Nanoscience and Nanotechnology – Nanocenter (CENN Nanocenter), Ljubljana, Slovenia and a JEOL 7600F FEG SEM at CEMM in JSI. Measurements of chemical composition were performed with an Oxford instruments 50 mm^2 X-max silicon drift detector (SDD) attached to the microscope.

3.1.2 Electrochemistry Techniques

A Gamry Reference 600 potentiostat (Gamry Instruments, Warminster, Pennsylvania, USA) was used for conducting the electrochemical experiments. Electrodes from the potentiostat were attached to the in situ electrochemical holder.

3.1.2.1 Chronoamperometry

Chronoamperometry is an electrochemical technique in which the potential of the working electrode is stepped and the resulting current from faradaic processes occurring at the electrode (caused by the potential step) are monitored as a function of time [132].

3.1.2.2 Cyclic Voltammetry

Cyclic voltammetry (CV) is a type of potentiodynamic electrochemical measurement. In a cyclic voltammetry experiment, the working electrode potential is ramped linearly versus time [133].

3.1.3 Contact-Angle Measurement

Contact angle measurements were performed using a Contact angle meter Theta Lite-Biolin Scientific. The equipment has a measuring range: 0-180 deg. and 0.01-1000 mN/m, accuracy of +/- 0.1 deg., +/- 0.01 mN/m. The results are recorded using a camera with a 640 x 480 resolution and a maximum measuring speed of 60 fps.

3.1.4 X-Ray Powder Diffraction

Samples of ceramic powder were analysed with an X-Ray Powder Diffractometer Siemens D5000 at the National Institute of Chemistry, Ljubljana, Slovenia, with radiation wavelength Cu-Kα1 = 1.5406 Å.

3.1.5 Atomic Force Microscopy

An Atomic force microscope (AFM) Veeco Dimension 3100 at the Department for Nanostructured materials at JSI was used for the surface analysis of Si chips.

3.1.6 Modified TEM Holder for E-chip Analysis

SAED and EDS analyses proved to be challenging in situ using the LCTEM holders due to the strong dissipation of an electron beam in the liquid [134]. Therefore, we have specially modified the Jeol single tilt TEM holder by drilling a space large enough that chips could fit inside (Figure 3.1). With this holder, we were able to perform subsequent TEM analysis of disassembled air-dried chips.

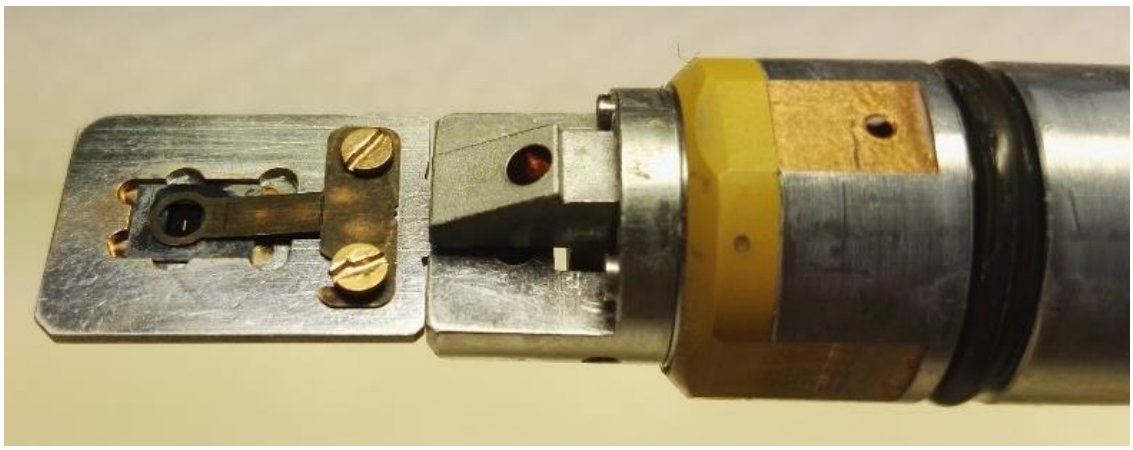

Figure 3.1: Modified TEM holder for e-chips analysis.

Typically, to minimize the effects of water radiolysis, LCTEM experiments were performed at the lowest electron dose rate possible, at which the formation of NPs could still be visually detected. This value was determined experimentally. More details about dose rate measurements are in Section 3.4.

3.1.7 Electrolytic Ex Situ Cell

To test and prove that electrochemical processes work before they were observed in situ in the LCTEM, they were tested using an ex situ cell. Two prototype ex situ cells were built (Figure 3.2). They were built around an electrochemical chip, so that the WE, CE, and RE electrodes could be easily attached, and that the electrolyte was able to wet the electrodes of the chip.

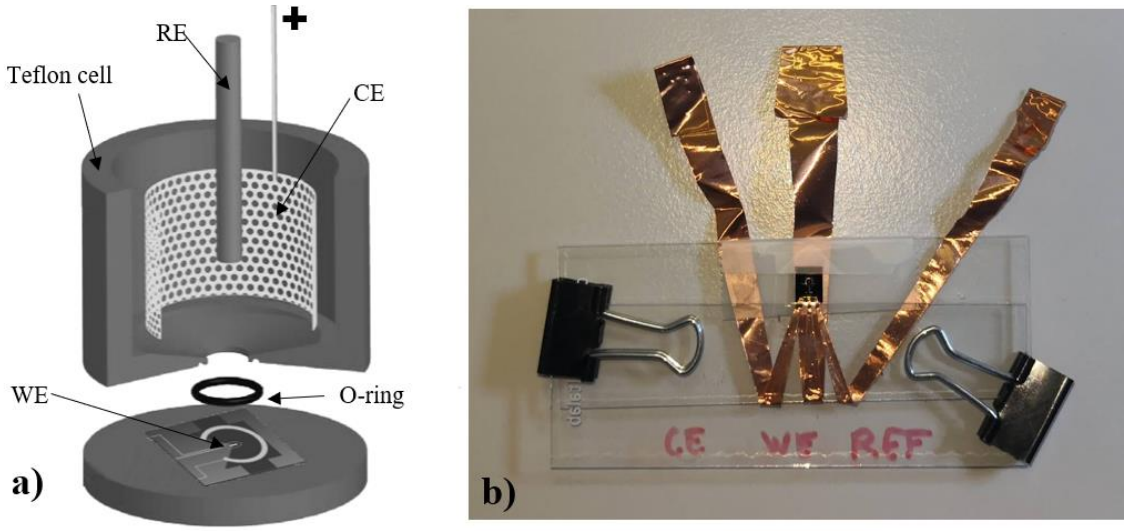

Figure 3.2: Ex situ electrolytic cells: a) the first prototype with "closed" cylindrical design [105] and b) second prototype with open "flat" design.

3.2 LCTEM Experiments

3.2.1 The in Situ LCTEM Specimen Holders

The main tool of our research was a Jeol JSM-2100 TEM equipped with two LCTEM holders: in situ heating holder and in situ electrochemistry holder.

3.2.1.1 In Situ Heating Holder

The in situ heating holder (trademark name P300) (Figure 3.3) was produced by the manufacturer Protochips, Inc., Raleigh, NC.

The most important part of the holder is the titanium tip. The holder tip contains a chamber for the liquid and places for the inner and outer O-rings, which provide the vacuum seal. Through the holder, two intake and one outtake tubes are passing through and they re-emerge at the bottom of the liquid chamber. The inner diameters of intake and outtake tubes are 100 µm and 150 µm, respectively. This is to prevent pressure build-up inside the liquid cell. The intake and outtake tubes are made with polyether ether ketone (PEEK) tubing connected with specialized syringe pumps, which provide the push flow of liquid through the entire system. The holder is designed for the maximum liquid flow of 83 nL/s.

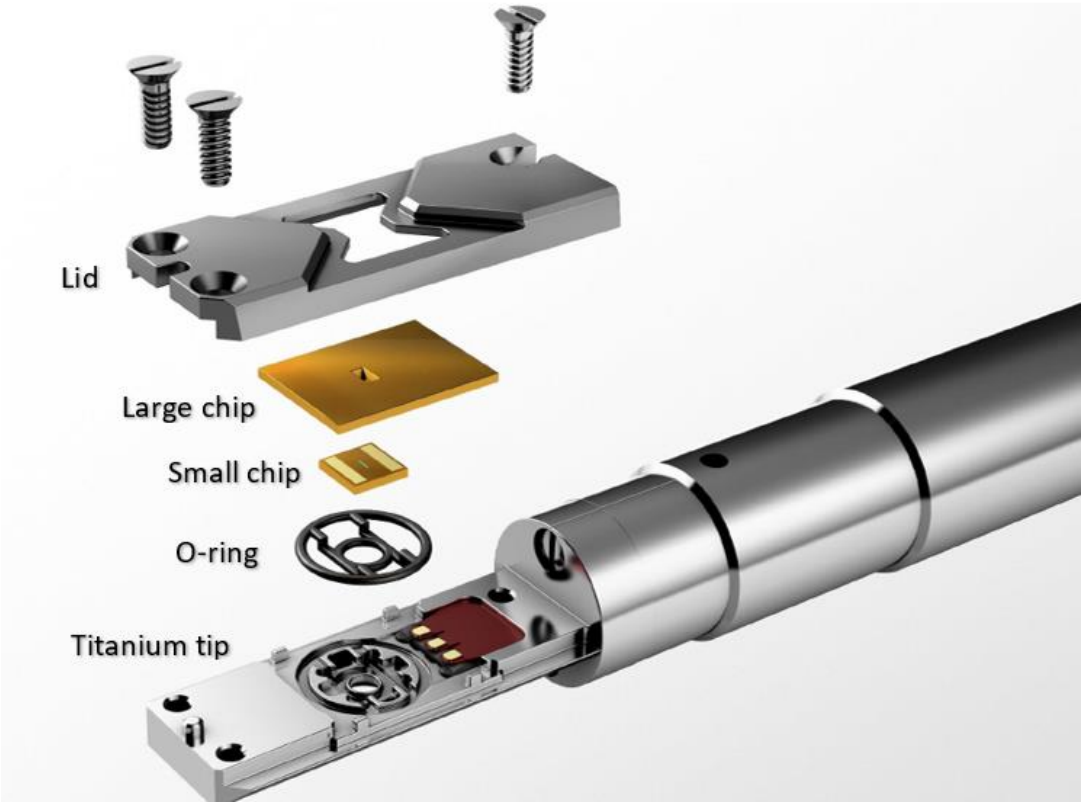

Figure 3.3: The LCTEM holder used in the research [136].

The liquid inside the holder is kept in between two silicon chips (usually called the large and small chips) with a 40-nm-thick Si_3N_4 windows for observing the liquid inside the TEM [135] (Figure 3.4). The large chips (size 2 x 4.5 mm) contain electrodes and tungsten heating coils for the heating of the liquid [137]. The small chips (size of 2.0 x 4.5 mm) contain rectangular shaped gold spacers [76]. The spacers define the thickness of the liquid and the type of experiment (static or dynamic experiments). There are 50 nm, 150 nm, 500 nm, 2000 nm, and 5000 nm thick spacers available. Consequently, the spacers also define the volume of liquid inside the liquid cell. The volumes for the mentioned spacers are: 0.2 nL, 0.6 nL, 2 nL, 8 nL and 20 nL, respectively. Reducing the liquid thickness improved the TEM resolution; however, the effects of the radiolysis in the smaller volume of liquid are higher (se Figure 3.4 for more details).

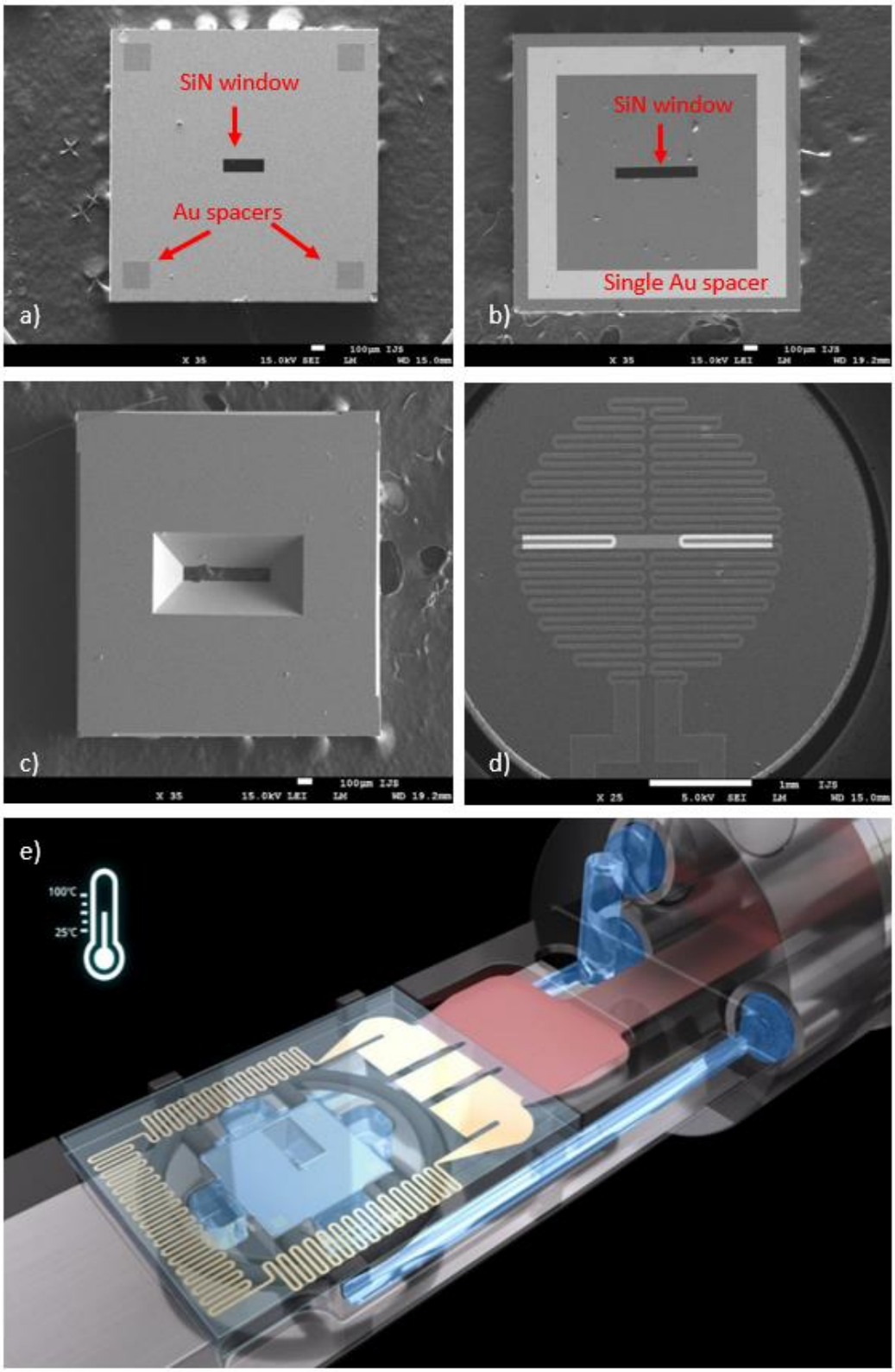

Figure 3.4: Small silicon chip with four Au spacers for dynamic mode experiments (a) and small silicon chip with a closed rectangular spacer for static mode experiments (b) Upper part of a small chip. d) Section of a large chip with integrated heating coils (Credit: Maja Koblar), e) rendering of chips during use in the heating experiments [136].

Due to the rectangular shape of the windows in both chips, two different window geometries are possible: parallel and crossed geometry. Parallel geometry has a larger viewing area (ca. 150 x 30 µm). For comparison, the crossed geometry has a viewing area of 50 x 50 µm. For that reason, the crossed geometry is preferred. The crossed geometry also has less "window bowing effect". Window bowing is an effect of bowing of the Si_3N_4 windows inside the ultra-high vacuum of the TEM, due to the large pressure difference. This bowing increases the liquid thickness defined by the spacers on the chip. Window bowing can be substantial (e.g. in case of 50-nm- and 70-nm-sized windows, it is 2 µm and 3 µm respectively) [136] (Reference: Poseidon Select manual: Protochips, Inc., Copyright 2017, Document Number: M-00001 v1.3). The most prominent bowing occurs in the center of windows. Therefore, the most suitable parts for the analysis inside the TEM were the corners of the chips, where the liquid layer thickness is ≈ as spacer thickness.

The temperature of the liquid in the liquid cell was controlled indirectly by applying an electric current through the tungsten coils located on the large chip. The electrical current was applied with a Keithley controller via the Protochips Poseidon V2.0.4 software with a calibration curve that was also provided by the manufacturer. With this system, the temperature range between 20 °C and 100 °C could be achieved. The heating rate could be set from 0.1 °C/min to a maximum of 10 °C/s. The temperature increase of the liquid as a result of the electron beam irradiation was not taken into consideration, as it was shown in several studies that for the given experimental beam currents the temperature can rise only by a few °C [47], [56]. After heating, electronic cooling was not possible. The samples cooled naturally with heat dissipation. The cooling rates dropped asymptotically, and the average cooling rate at the temperature of 60 °C was ≈ 0.6 °C/s.
Experiments inside the in situ heating holder can be performed in either "static" or "dynamic" mode. Static mode refers to the pouring of a liquid drop between the chips and sealing all the tubing with specialized plastic plugs. For "static" mode experiments, special chips with spacers that encircle the entire chip were required [76]. Dynamic modes refer to the flow of liquid through the holder tip. It is possible to flow one type of liquid through the first intake pipe and different types of liquid through the second intake pipe and consequently observe how the two liquids are mixed and observed inside the liquid cell. One of the two intake pipes could also be vacuum sealed, which allows observation of the flow of only one single type of liquid through the holder. All the heating experiments in this thesis were in the static mode.

3.2.1.2 In Situ Electrochemistry Holder

In situ electrochemistry holder (trademark name Poseidon 510) (Protochips Inc., Raleigh, NC, USA) (Figure 3.5) was used in our in situ electrochemistry experiments. Many of the features of these holders are similar to the in situ heating holder. The holder tip is similar to the in situ heating holder. The liquid is pushed through the holder with the help of syringe pumps. At the backside of the holder, there are attachments for the electrode cables, connecting the holder with the Gamry Reference 600 potentiostat.

Figure 3.5: In situ electrochemical holder with two closed ports for liquid intake/outtake and ports for attaching the RE, CE, and WE electrodes. b) holder inserted in TEM c) Whole experimental setup with TEM, Gamry potentiostat and two syringe potentiostats.

The most important part of the in situ electrochemistry holder is the special large chips with integrated WE, CE, and RE electrodes (Figure 3.6). The WE is integrated into the SiN window, enabling observations of the chemical deposition/dissolution of the NPs. WE electrodes from glassy carbon and Pt were available.

Data about the holder were obtained from the User Manual Poseidon 210, version 1.1. (Protochips, 2015).

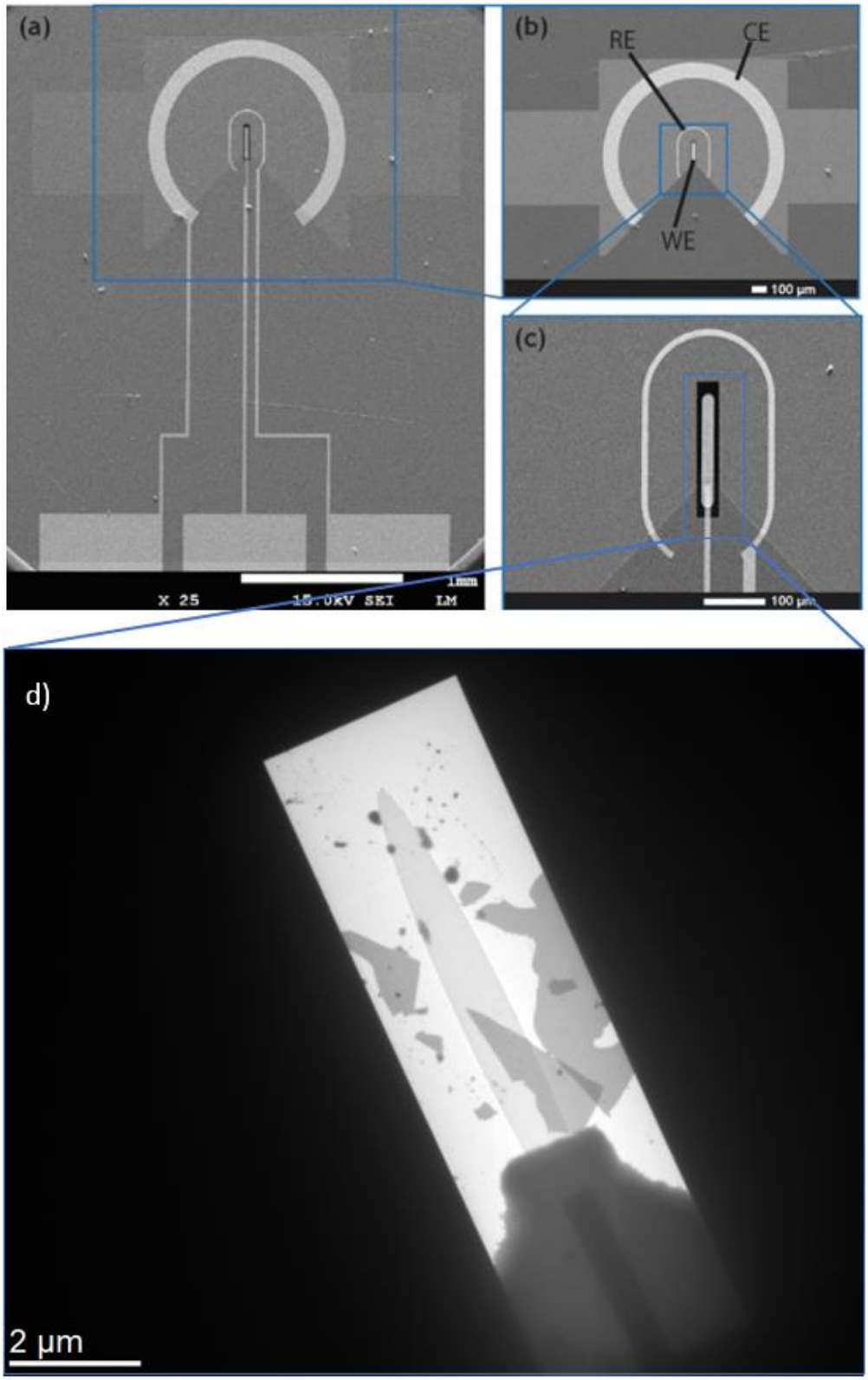

Figure 3.6: Electrochemistry chip (Credit: Maja Koblar): a) Whole electrochemical chips, b) electrodes (RE = reference electrode, CE = counter electrode, WE = working electrode), c) window with transparent glassy carbon electrode, d) Glassy carbon electrode viewed in a TEM.

3.2.1.3 LCTEM Experimental Procedures

Here the full experimental procedure for the LCTEM experiments is shown. One of the aims of our experiments was to observe homogenous nucleation. For this process to occur all possible nucleation agents (e.g. dust, contaminants, etc.) must be removed. Therefore, the tools and the sample preparation room were as clean and dust-free as it was possible. A special laboratory for LCTEM sample preparation was established at the Department for Nanostructured Materials at the JSI.

The outlined procedure took around half to a full day to complete, not including the preparation of the sample. The same chips could be used in several different experiments. But due to the above-mentioned risk of contamination, this was strictly avoided. Steps 1-5 were similar in the case of both holders (in situ heating and in situ electrochemistry). However, steps 6 and 8 were different for each holder.

Step 1: Preparation of the chips

The procedure started with the preparation of the experimental solution used in the LCTEM experiments. SiN chips were shipped protected with a protective photoresist, which was removed before the use of the chips. We removed the photoresist by rinsing the chips in acetone and methanol for 1 minute (Figure 3.7). After the rinsing the chips were air-dried. Careful measures were taken, so that during these procedures the electrodes or W coils were not scratched with tweezers.

Initially, the chips are hydrophobic. For that reason, they were plasma cleaned (see Section 4.1.1 for more details) for achieving good wetting of the sample liquid.

Figure 3.7: Initial cleaning of chips in a petri dish with an alcohol solution.

Step 2: Assembly of the holder

After the plasma cleaning of the chips, the delicate process of holder assembly took place. The first part of the assembly was placing the small chip on top of both O-rings inside of

the in situ heating holder (Figure 3.8a-b). On the small chip sample, a drop of solution was pipetted with a precise pipet (Figure 3.8c). The volume of the pipetted solution was always several orders of magnitude larger than the available space between the chips. Therefore, the solution was squeezed out during the assembly of the holder. The chips were covered with the titanium lid, which in correlation with the O-rings and brass screws provided the vacuum seal. The lid was screwed into place with three small brass screws (Figure 3.8e-f). Even the slightest mistake in the described holder assembly procedure resulted in the total failure of the experiment. Especially delicate were the thin SiN windows. An optical microscope was used to check if the window was intact (Figure 3.8g).

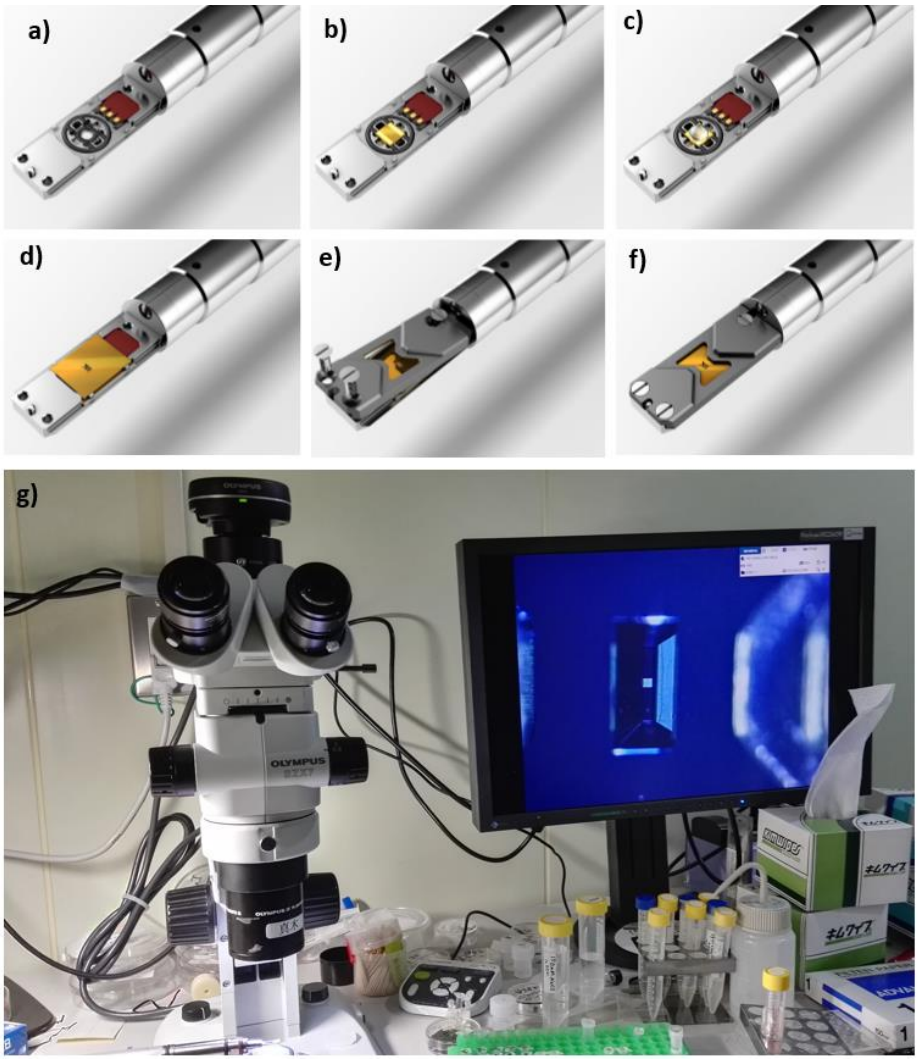

Figure 3.8: Sequence of assembly of the LCTEM holder: a) Placing the O-ring, placing the small chip on O-ring, c) dropping the liquid on the surface of the chips, d) placing large e chip, e) and f) closing the lid [136] g) optical microscope check of the window of the chip at the end of the assembly.

Step 3: Leak check

After the holder was assembled it was inserted for 10 min into the vacuum leak check (Figure 3.9) to check for possible leakage and to simulate the high-vacuum environment of a TEM. At the same time, it also acted as a drying agent to evaporate any remaining

liquid and moisture that escaped between the O-rings. After that, the holder was removed from leak check and inserted into the TEM.

Figure 3.9: LCTEM heating holder performing a leak check.

Step 4: Insertion in the TEM
Once inside the TEM (Figure 3.10), the holder was connected to the tubing, syringe pumps, and (in case of in situ heating experiments) to the Keithley controller (in situ heating holder) /Gamry potentiostat (in situ electrochemistry holder) and laptop computer. After that, the system was ready for in situ liquid cell experiments.

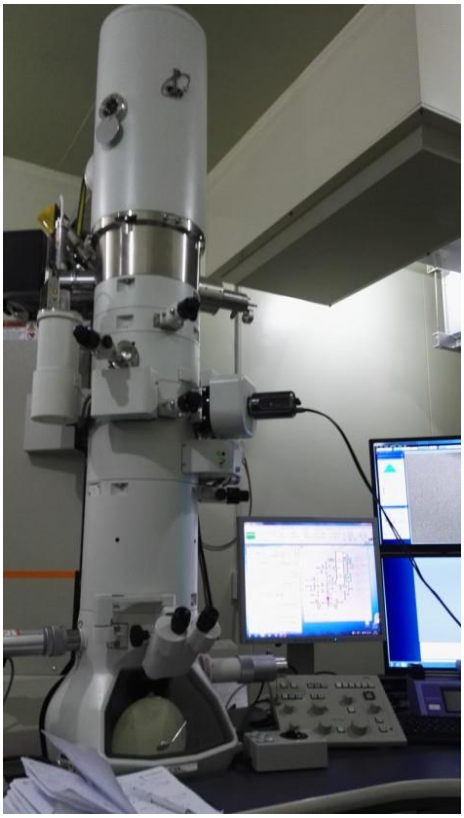

Figure 3.10: Insertion of LCTEM holder into TEM.

Step 5: TEM alignment
An important, however, frequently neglected, step related to a TEM is the microscope alignment. Usually, when performing conventional TEM analysis, the microscope is aligned and calibrated after the sample is already inserted into the microscope. However, in the case of LCTEM experiments, there were severe difficulties with this procedure due to the shifting liquid and radiolysis effects. Therefore, most calibration steps were performed before the insertion of the in situ holder.

Step 6: LCTEM experiments
After that, the LCTEM holder containing the sample was inserted into the TEM, and the in situ experiments were performed (Figure 3.11). In the case of the in situ heating experiments, the sample was usually investigated, i.e., observed by using the electron beam during the whole length of the experiment, by means of video capturing. That allowed further analysis of the obtained videos, which provided important data for the interpretation of the videos.

In the case of the in situ electrochemistry experiments, the electron dose rate was reduced with the so-called: "single exposure technique", where the sample is observed with an electron beam only periodically only every few (depending on the experiment) minutes or few hours. Resulting in a very low electron dose rate (100–5000 $e^-/nm^2/s$), comparable with a cryo-TEM [35]. The obvious disadvantage of this method is that sample can be observed/imaged only for a very short amount of time, which means that important events could be missed when the beam is blanked. Therefore, this method was only used when the expected reaction kinetics during the experiment was relatively low.

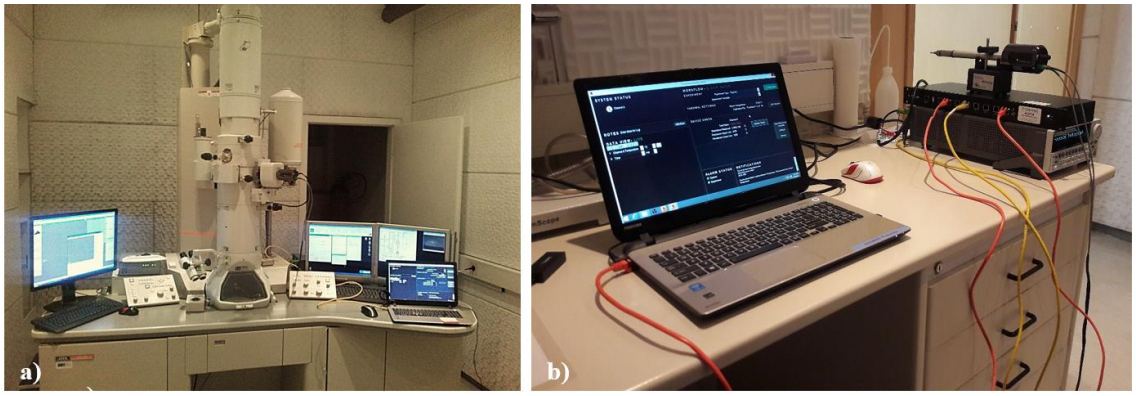

Figure 3.11: Fully assembled LCTEM set up (a) is controlled by a laptop computer connected to the Keithly controller (b).

Step 7: Obtaining the correct dose rate
One of the most important experimental parameters prior to the LCTEM experiments is related to the selection of the correct electron dose rate. The electron density, which has the greatest influence on the electron dose rate, during the experiments was changed using the combination of the condenser aperture in a TEM and by focusing and spreading the electron beam using the objective lens of a TEM. Calibrations were performed at the regular intervals so that the correct required electron densities were used during the experiments.

Step 8: Disassembly and cleaning
After the experiments were finished and all the data successfully obtained, the holder was disassembled (Step 2 in reverse order). The chips were cleaned with deionized water and air-dried. They were stored in the vacuum desiccator before they were reanalyzed using a conventional TEM. The holder, on the other hand, was cleaned using ethanol/deionized water and placed in the leak check to avoid contamination and future problems with vacuum systems of the TEM.

Step 9: Data storage and analysis
The data were kept uncompressed in order not to degrade the original information. For data analysis see the section 3.5 for more details.

3.3 Synthesis Procedures

3.3.1 In Situ Synthesis of Gold NPs

For the synthesis of the Au NPs, the LCTEM technique was used. Gold(III) chloride trihydrate (chloroauric acid) (Sigma-Aldrich, >99.9% purity), particles were mixed with deionized water (Milli-Q) to produce a 1.5-mM water solution. The solution was prepared a few minutes before it was inserted into the liquid cell to prevent any potential spontaneous Au NPs' formation. In the experiments, small chips with 50-nm-thick enclosed spacers were used combined with large heating chips. The experiments were carried out in a static mode. Electron dose rates between 10^8 and 10^{12} Gy/s and temperatures of 25–40 °C were used.

After the initial in situ LCTEM experiments, the chips were air-dried and inserted into the TEM in a dried state with a specially modified holder. With this technique, the morphology, composition, and crystal structure of the precipitates that were formed during the in situ LCTEM experiments were subsequently analyzed in a dried state by using the conventional TEM, SAED and EDS analysis.

3.3.2 Ex Situ and in Situ Synthesis of Yttria NPs

For the synthesis of yttrium oxide NPs the method of Qin et al. [68] was used. A few drops of 0.2-molar nitric acid (HNO_3) (Sigma-Aldrich, HNO_3, ≤5 ppm ign. residue) were added to adjust the pH to 4.5. After yttrium acetate hydrate (YAc) (Sigma-Aldrich, >99.9 % purity) was completely dissolved using ultrasonication, urea (Sigma-Aldrich, >99.5 % purity) was added to the solution. A molar ratio of 1: 20: 5555 = YAc: Urea: water was used. Urea decomposes following the chemical reactions:

Equation 3.1 shows the decomposition of urea. Equations 3.2– 3.4 represent the subsequent dissociation of the reaction products, OH^- and CO_3^{2-} ions.

$$NH_2COHN_2 + 4H_2O \rightarrow 2NH_4OH + H_2CO_3 \quad (3.1)$$
$$NH_4OH \leftrightarrow NH_4^+ + OH^- \quad (3.2)$$
$$H_2CO_3 \leftrightarrow H^+ + OH^- \quad (3.3)$$
$$HCO_3^- \leftrightarrow H^+ + CO_3^{2-} \quad (3.4)$$

Yttrium acetate hydrate dissolves in water following the chemical reaction:

$$(CH_3CO_2)_3Y{\cdot}xH_2O \rightarrow Y^{3+} + 3{*}CH_3COO^- \quad (3.5)$$

Precipitation of yttrium NPs can be described by following the possible reactions:

$$3Y^{3+} + 2CO_3^{2-} + OH^- \leftrightarrow YOH(CO_3) \leftrightarrow YOH(H_2O)^{2+}\ YOH(H_2O)^{2+} \quad (3.6)$$
$$3Y^{3+} + 2CO_3^{2-} + OH^- \leftrightarrow Y_2CO_3 \quad (3.7)$$
$$3Y^{3+} + 2CO_3^{2-} + OH^- \leftrightarrow Y(OH)_3 \quad (3.8)$$

The experiments were initially performed ex situ in a regular lab. After that, they were repeated in situ with the LCTEM.

The experimental solution was heated in a glass beaker at 80 °C. When (after 15 min) the first NPs appeared, the solution was quenched in cold water, preventing further growth of the NPs. NP powder was collected using centrifugation (6500 rpm, 10 min). The powder was subsequently analyzed using XRD and SEM. The powder was also put on the surface of SiN chips and observed in TEM. The phase composition was determined using SAED and the chemical composition using EDS.

In the second step, the same chips were then placed in a furnace in an oxygen-rich atmosphere and annealed for 2 h at 700 °C. After that, they were re-analyzed in the TEM.

The same solution used in the ex situ experiments was also used in the LCTEM experiments. In this case, small chips with 150-nm spacers were used and large chips with heating coils. To properly evaluate the electron-beam effect during the in situ observation, the so prepared solution was first observed for 30 minutes at room temperature and a dose rate of 5000 $e^-/nm^2/s$. During this period, no NP precipitation occurred, indicating that the electron beam had a negligible effect.

The samples were in situ LCTEM heated for 500 s at 80 °C (facilitating the formation of amorphous Y NPs). When the NPs stopped growing the liquid cell was disassembled

and the chips were carefully rinsed with water and air dried. The air-dried chips were placed in a furnace in an oxygen-rich atmosphere and annealed for 2 h at 700 °C (the same procedure as in the ex situ synthesis). The chips containing the annealed NPs were placed in specially modified holders and reanalyzed using the conventional TEM.

3.3.3 In Situ Electrochemical Synthesis of Iron NPs

For the electrochemical synthesis of iron NPs, a solution of 0.1-mM Iron(II) sulfate heptahydrate (Sigma-Aldrich, ≥99 % purity), 0.1-mM sodium citrate (Sigma-Aldrich, ≥99 % purity), and 1.0-mM sodium sulfate (Sigma-Aldrich, ≥99 % purity) was prepared in a glass beaker. The solution has a pH value of 2.8. The solution was inserted into an in situ electrochemistry holder. A small chip with 50-nm spacer was used and a large chip containing glassy carbon WE and Pt WE and CO. A Gamry Reference 600 potentiostat was used for conducting the electrochemical experiments. To minimize artifacts such as the beam-induced radiolysis of water, the electron beam was blocked with a condenser aperture during the electrodeposition.

3.4 Measurements of the Dose Rate in the TEM

There is no accepted consensus in the TEM community about whether the electron dose rate of the radiation dose rate is to be used to unequivocally define the experimental parameters during the LCTEM experiments. The main reason for choosing SI-derived units, generally accepted by radiation chemists, is to make a clear differentiation between the electron dose typically defined in the TEM community, as the charge density hitting the specimen, and the electron dose rate, which is defined as the energy absorbed per unit volume (J/kg = Gy). In the first case the electron dose is typically expressed as the number of electrons per unit area (e^-/nm^2), neglecting the energy transfer of the electron per unit path length as a function of the investigated material, defined as the stopping power. In both cases the dose rate is then defined as the dose rate per unit time ($e^-/nm^2\,s$, Gy/s). Another more practical reason is that almost all the kinetic models for radiolysis are using SI-derived units and it would therefore be extremely difficult to make a direct correlation with previous studies.

Since our TEM (Jeol 2100) was not equipped with a Faraday cup that would enable us accurate measurements of the electron current, we have used a different approach for measurement the dose rate. For the selected microscope conditions (magnification and spot size) we have inserted a CCD camera into TEM. The calibration factor is the inverse of the known number, showing us how many individual electrons need to hit each pixel of the camera to produce an intensity of 1. The manufacturer of the camera (Gatan) provided us with the calibration factor for our camera (0.367). This means that on average 2.7 electrons need to hit each pixel of the camera to produce an intensity value of one. In the second step, we recorded the image of the empty holder with an exposure time of 1 second. Then we used DigitalMicrograph software to measure the average intensity of the image. From the average intensities, using the calibration factor, we were able to calculate the electron dose rate for the selected microscope operating conditions, as shown in Figure 3.12.

The following equations were used to properly combine the electron-dose rate, as an electron exposure per unit time, which can be directly assessed during the TEM experiments and the corresponding dose rate as the energy absorbed per unit mass and time:

$$D\left[\frac{\frac{electrons}{nm^2}}{s}\right] = \frac{R_{pix} * I * c_{cal}}{t} \tag{3.9}$$

, where D is the dose rate, R_{pix} is the relative pixel size, I is an average measured intensity and c_{cal} is the calibration factor (0.367) and t is time.

To convert the electron dose rate from electrons/nm^2/s to Gy/s we have used the following equation:

$$D\left[\frac{Gy}{s}\right] = \frac{D\left[\frac{\frac{electrons}{nm^2}}{s}\right] * S}{q_e} \tag{3.10}$$

, where D is the dose rate, S is the stopping power of water (2.78 *10^5 eV/m^2*s/e$^-$) and q_e is the elementary charge (1.6 * 10^{-19} C).

As an example, the dose rate of 10^9 Gy/s would convert to an into electron-beam exposure of approximately 200 e$^-$/nm^2/s, assuming the 200 kV electrons.

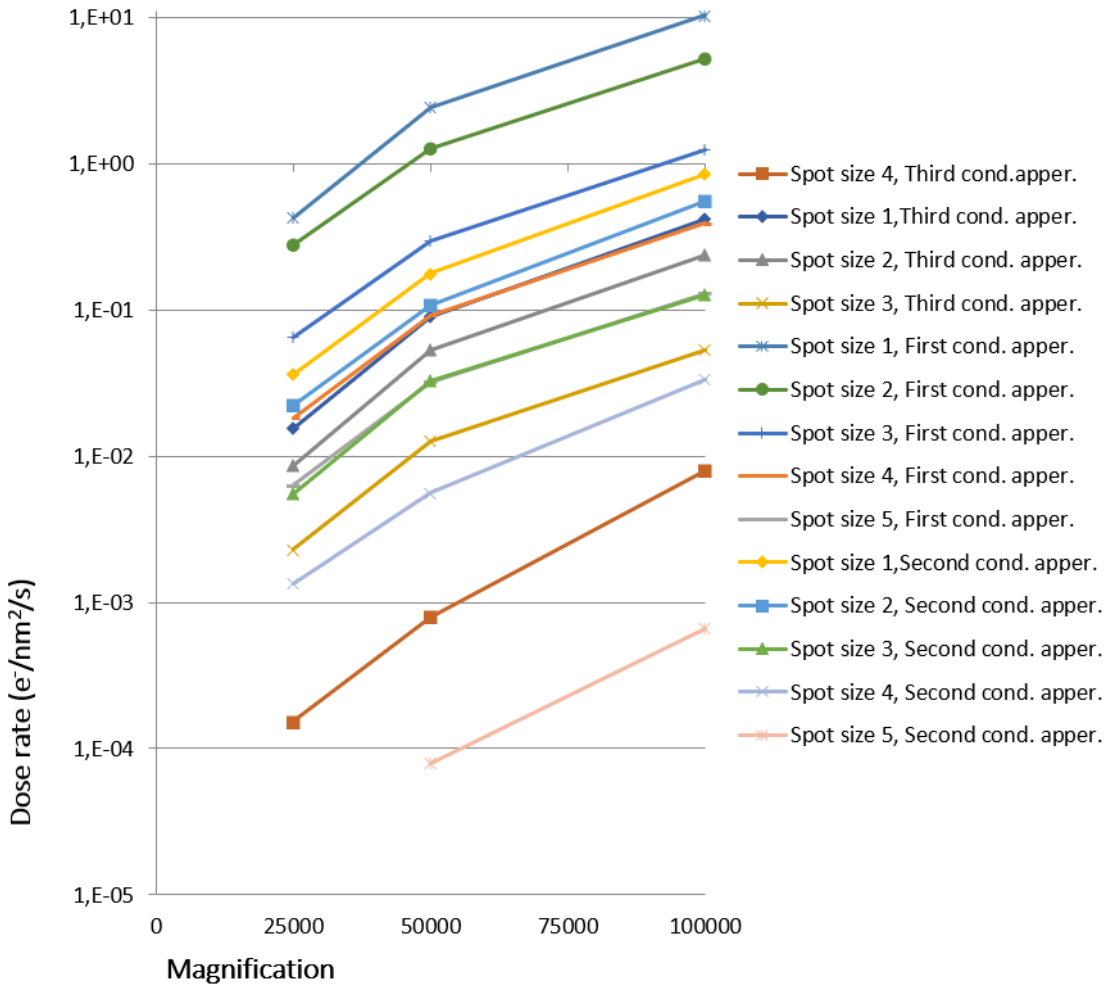

Figure 3.12: Measured dose rate as a function of microscope conditions: spot size, aperture size, and magnification. Physical size of the probe was uniform and was defined by the exact diameter projected on the phosphorus viewing screen, which was controlled by the condenser lens (i.e., beam brightness).

3.5 Procedures for Obtaining Quantitative Data From the LCTEM

With the LCTEM technique, data are obtained either in the form of a spectral analysis (EDS, electron loss spectroscopy (EELS), etc. or in the form of images/videos. Videos represent a challenge, since videos take a lot of space and represent very large datasets, which are difficult and time-consuming to analyze.

ImageJ software [138] was used for the analysis and extraction of quantitative data from the videos. The Measure tool inside the software enabled us to accurately measure the growth/dissolution rate of the NPs, with a millisecond temporal resolution. The same software was also used for tracking the NPs. Quantitative data were also extracted using software and plugins in the DigitalMicrograph software [139].

3.6 Electron Radiolysis Modeling

The extensive simulations algorithms for the radiolysis inside the LCTEM environment were developed using the MATLAB software platform (MATLAB 2016b, The MathWorks, Inc., Natick, Massachusetts, United States).

Intentionally left blank

Chapter 4

Results and discussion

4.1 Development of Procedures and Method for the Successful Execution of the LCTEM Experiments

One of the important aims of this Ph.D. thesis was to establish procedures for producing reliable and repeatable results.

4.1.1 Plasma Cleaning

Plasma cleaning was a necessary step before the LCTEM experiments. Therefore, the chips were plasma cleaned in a plasma cleaner using O_2/Ar gas (Figure 4.1a). However, it was not known for how long after the plasma cleaning procedure the chips remain hydrophilic. For that reason, some experiments were performed where the hydrophilic effect was measured by contact-angle measurements at different periods after the plasma cleaning (Figure 4.1b). The contact angle θ of non-plasma cleaned chips was measured to 60°. In the experiments, 30 s of O_2-Ar plasma was used. Up to 30 min after the plasma cleaning perfect wetting ($\theta = 0°$) was achieved. One hour after the experiment began the contact angle had increased to 15°. The chips remained reasonably hydrophilic ($\theta<20°$) for ≈ 24 hours. The contact angle slowly increased over time until it finally stalled at $\theta = 40°$ after the period of 40 h.

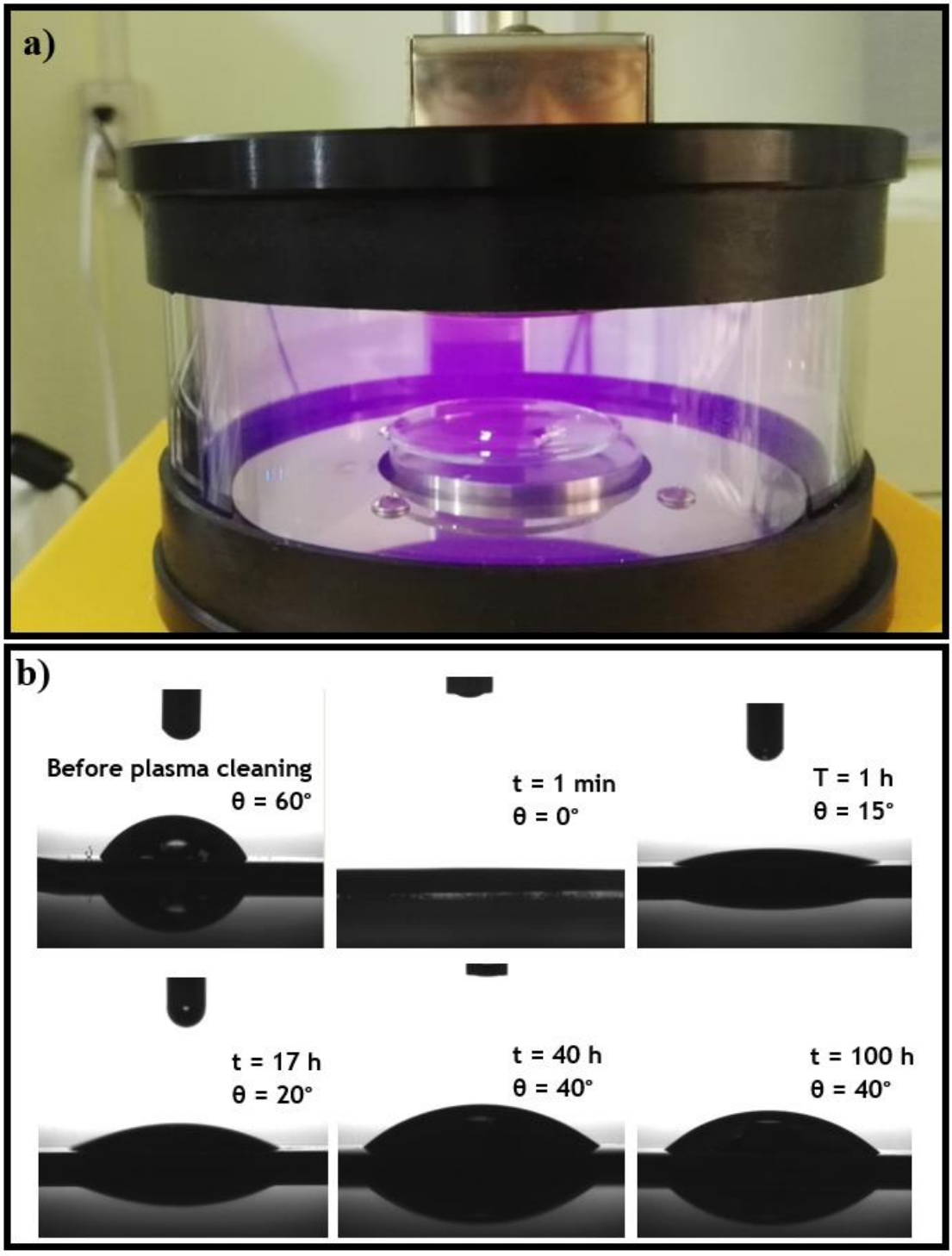

Figure 4.1: a) Plasma cleaning of the chips, b) Contact angles of silicon chip: before plasma cleaning, b) 1 min, 1 h, 17 h, 40 h and 100 h after plasma cleaning.

AFM analyses of the surface roughness of the chips before and after the plasma cleaning were also performed (Figure 4.2). There was no statistically significant difference in the average measured surface roughness (4.561 nm and 4.698 nm, respectively), confirming that the plasma cleaning has a primarily chemical effect.

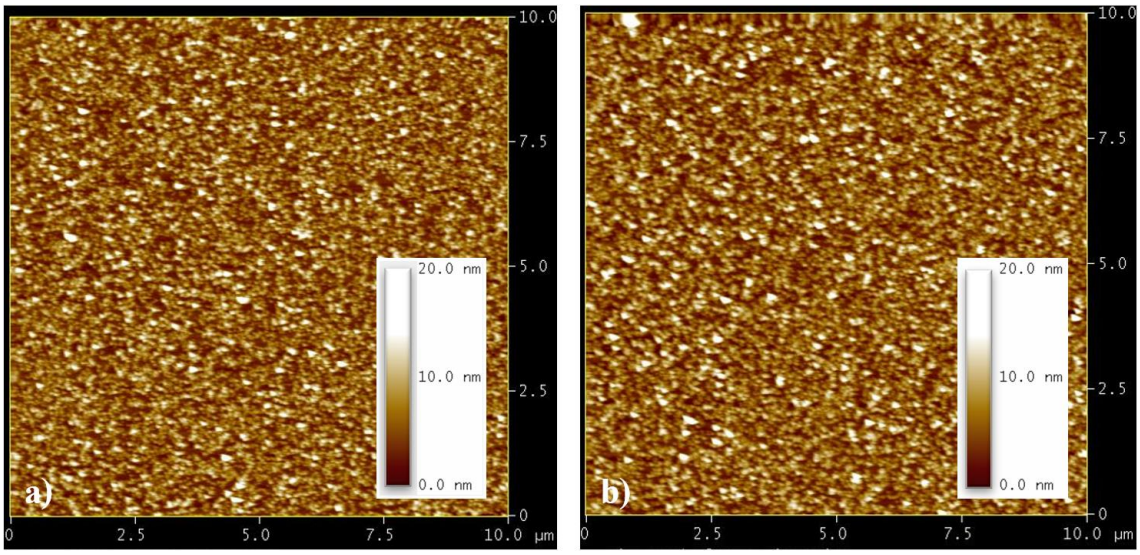

Figure 4.2: AFM measurement of surface roughness before (a) and after (b) plasma cleaning indicates there is no difference

4.1.2 Visualizing the Flow of the Liquid

For these experiments, a silicon chip has been replaced to a glass sheet (Figure 4.3). This allowed us to see the entire liquid chamber of the holder tip, instead of only the typical 150 x 30 µm viewing area of the SiN windows. These experiments were performed using colloidal gold suspended in water and deionized water. The experiments showed that liquids do mix well before they reach the liquid cell and that they are diffusionally mixed inside the PEEK tubing [12]. This is a result of the chamber of the holder where mixing should occur being very thin (ca. 100 nm), compared to the surrounding chamber (ca. 1 mm). Therefore, most of the volume of the liquid flows around the area where mixing should occur.

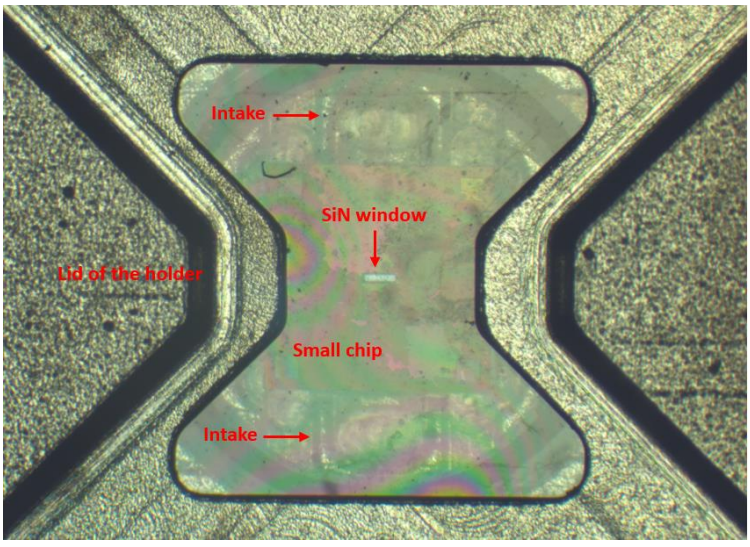

Figure 4.3: LCTEM holder tip with closed lid and a thin glass sheet as a replacement for a large silicon chip. Small silicon chip with SiN window could be seen through the glass, and intake pipes could be seen.

4.1.3 Measurements of the Open Circuit Potential

Open circuit potential (OCP) was measured using the LCTEM technique (Figure 4.4a). 0.1 M HCl was used as an electrolyte. The current was initially set to 0 A. The dose rate was changed using different apertures and spot sizes in the TEM (blue line in Figure 4.4a). After a period of 3600 s the OCP value reached 0 (Figure 4.4a) as a result of bubble formation (Figure 4.4b), proving OCP as an indicator for the presence of liquid in the liquid cell.

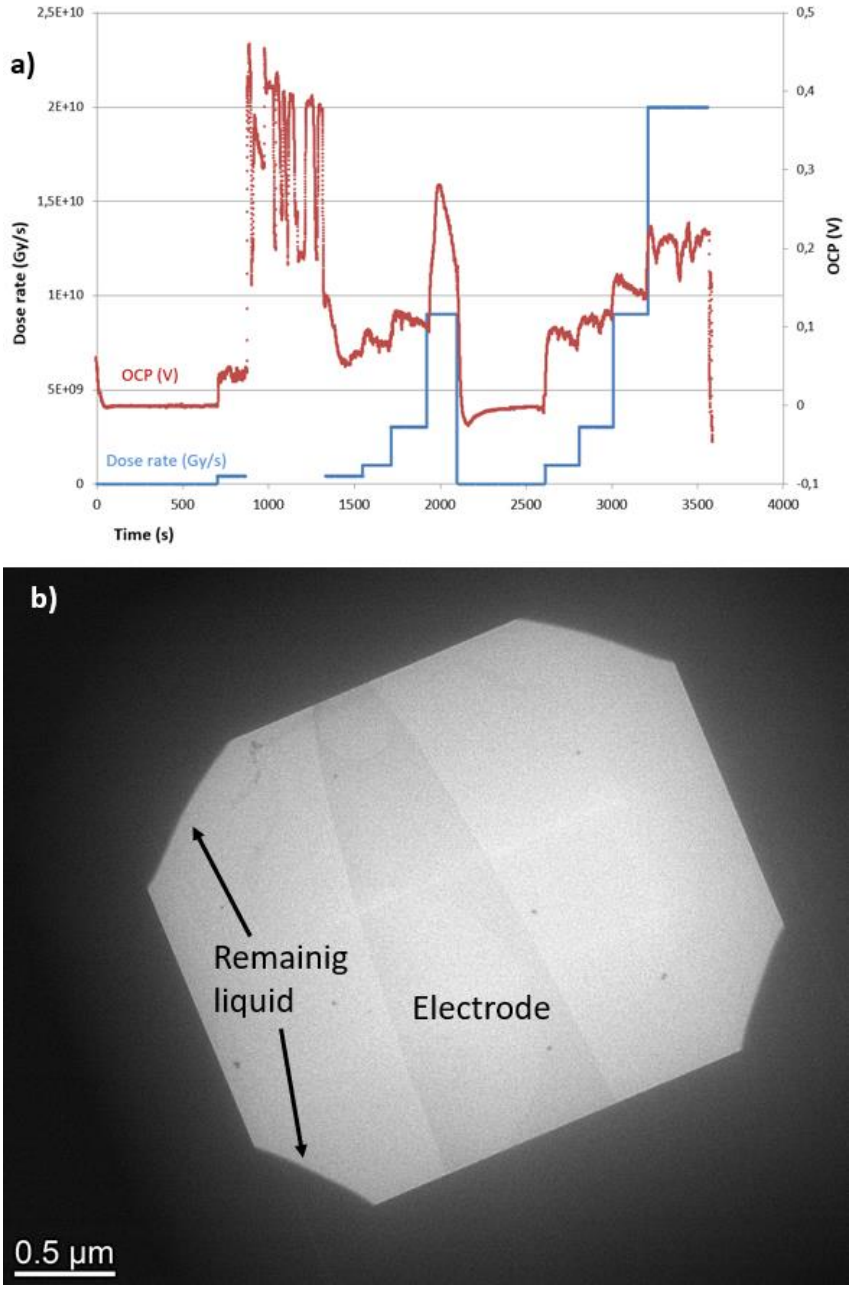

Figure 4.4: a) OCP (red line) as a function of dose rate (blue line). Note, that between 800 and 1200 s OCP is erratic due to the microscope alignment procedure, which rapidly changes the dose rate. Each subsequent change of the dose rate at the same time changed the OCP. After the period of 3600 s the bubble formation caused the OCP to reach a 0 value (b) – liquid is observed only on the edges of the window, where there is no electrode.

4.2 Kinetic Model of Radiolysis, the Case Study of Gold NP Nucleation

This section is partially based on an article of Ambrožič et al., [134] and presents an overview of the calculation for the kinetic radical-induced redox model.

4.2.1 The Description of the Kinetic Radical-Induced Redox Model for Gold

This section presents an overview of the calculation for the kinetic radical-induced redox model. The details of the chemical kinetics, the reaction-rate constants, the primary yields, and the evaluation of various model parameters, which are experimentally difficult to assess, are included.

The temperature-/doserate-dependent kinetic water-radiolysis model consists of reactions between the Au and the radiolytic species, being valid in the temperature range 20–100 °C for acidic and neutral initial solutions. For clarity, the calculated diagrams that are compared with the LCTEM are shown in the same temperature range 20–60 °C, matching the experimental conditions. The model includes the following species: e_{aq}^-, $H^\bullet$, $OH^\bullet$, H_2, H_2O_2, $HO_2^\bullet$, HO_2^-, H^+, O_2, $O_2^{\bullet-}$, and OH^-. The reaction-rate coefficients were taken from the literature [140] and rewritten in the form of the Arrhenius relation. The primary yields, i.e., the G-values for the water radiolysis for the temperature range 20–100 °C were linearly interpolated from the tabulated G-values at 20 °C and 100 °C, [140] respectively.

The kinetic model was further corrected to take into account the presence of the gaseous phase. A common phenomenon observed during LCTEM is the formation of gas bubbles, [27], [49], [58], [141] implying that the solubility of the formed gases in the liquid is exceeded during LCTEM. This is mainly due to the formation of molecular hydrogen and oxygen during the radiolysis. Figure 4.5 shows the pressure due to the dissolved H_2 and O_2 in a temperature-/dose-rate-dependent diagram for the equilibrium state. The temperature-dependent solubility values for H_2 and O_2 were obtained from the National Institute of Standards and Technology (NIST) [142], [143] and the initial pH was 2.8, assuming that all the liquid in the cell was evenly irradiated by the electron beam (Figure 4.5). The acidic initial pH was desirable since it is the least prone to radiolysis effects [43]. The initial pH of 2.8 was chosen beacuse the radiolytic species do not have a significant influence on the pH of the acidic solutions [43]. The desired pH value was achieved by preparing 1.5 mM $HAuCl_4$ solution (more details in Section 3.3.1). The inset shows a schematic of the LCTEM system, including the gaseous phase, where the thin liquid film (~ 50 nm [58]) enables O_2 and H_2 transfer between the liquid and the gas in a period of μs.

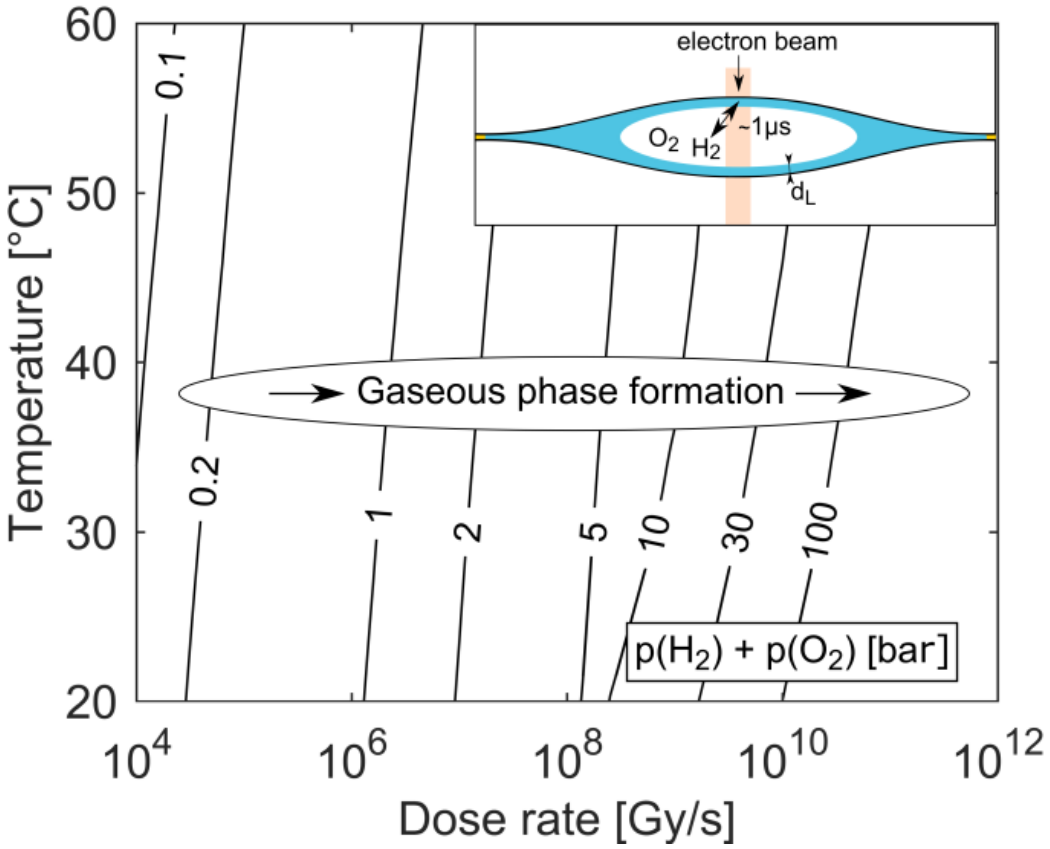

Figure 4.5: Pressure due to dissolved H_2 and O_2 in the equilibrium state for the water-radiolysis simulation. The initial pH is set to 2.8, with no initially dissolved O_2 or H_2. The inset shows a schematic representation of the LCTEM system with the gaseous phase. The liquid layer is very thin ($d_L \sim 50$ nm), allowing O_2 and H_2 transfer between the liquid and the gas in a period of µs.

As the partial pressure of water only changes from 0.023 bar at 20 °C to 0.199 bar at 60 °C we can assume that the influence of the water's partial pressure on the overall pressure in the gas phase is negligible. This suggests that the pressure increase in the closed-cell is predominately controlled by the electron dose rate, which provokes the formation of H_2 and O_2 due to water radiolysis. It was experimentally confirmed that a liquid cell with similar dimensions can withstand a pressure of 4 bar [144]. In practice, a large pressure increase is only expected at high dose rates, since only a small portion of the solution is irradiated by the electron beam. The pressure can also be partially compensated by bowing of the SiN window[19].

Figure 4.6 shows the equilibrium concentrations of the radiolysis products under typical LCTEM conditions for the Au system: a dose rate of 10^7 Gy/s and an initial pH of 2.8 in the temperature range 20–60 °C. The equilibrium concentrations of the radiolysis species were calculated at two limiting pressures in the liquid cells, i.e., at 1 bar and 5 bar (Figure 4.5). The pressure-dependent differences in the equilibrium concentration of the radiolysis species are visible (Figure 4.6). The concentrations of $H^{\bullet}$, $e^-_{aq,}$ and $OH^{\bullet}$ decrease by 20–50% when the pressure increases from 1 bar to 5 bars. Moreover, these graphs also indicate that the temperature affects the equilibrium concentrations of the radiolysis species (notice that the concentrations in Figure 4.6 are on a logarithmic scale). Importantly, all of them exhibit the same decreasing trend with the temperature increase.

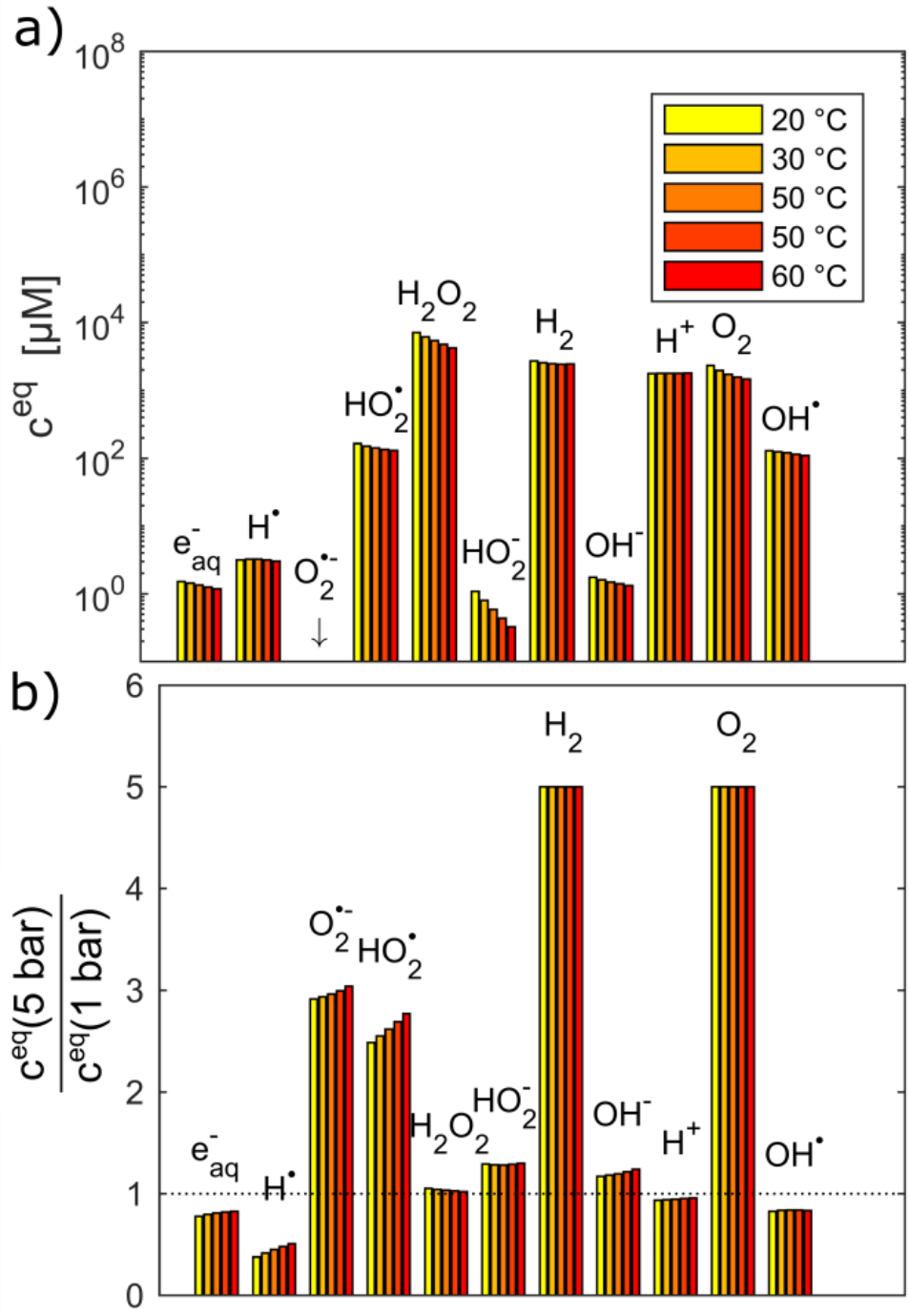

Figure 4.6: Equilibrium concentrations of radiolysis species in water at a dose rate of 10^7 Gy/s, $pH_{init} = 2.8$ and the temperature range 20–60 °C calculated at a) 1 bar and b) relative difference of equilibrium concentrations between 1 and 5 bar.

To estimate the influence of the radiolysis products on the precipitation/dissolution of Au the standard reduction potentials vs. SHE of the relevant half-cell reactions are listed in Table 4.1.

Table 4.1 Standard electrode and Nernst electrode potentials vs. SHE of the involved half-cell reactions.

Half cell	E_0 [V]	E_{NERNST} [V]	**Source** E_0
$e^- + [AuCl_2]^- \rightleftharpoons Au^0 + 2\ Cl^-$	1.15	0.97 ± 0.03	[145]
$e^- + H_2O \rightleftharpoons e^-_{aq}$	-2.79	-2.28 ± 0.36	[146]
$e^- + H^+ \rightleftharpoons H^\bullet$	-2.23	-2.09 ± 0.15	[146]
$O_2 + H^+ + e^- \rightleftharpoons HO_2^\bullet$	-0.04	-0.27 ± 0.12	[147]
$2\ H_2O + 2\ e^- \rightleftharpoons H_2 + 2\ OH^-$	-0.83	-0.26 ± 0.42	[148]
$2\ H^+ + 2\ e^- \rightleftharpoons H_2$	0.00	-0.09 ± 0.05	[148]
$O_2 + e^- \rightleftharpoons O_2^{\bullet -}$	-0.33	0.05 ± 0.14	[147]
$O_2 + 2\ H^+ + 2\ e^- \rightleftharpoons H_2O_2$	0.70	0.49 ± 0.12	[148]
$O_2^- + H^+ + e^- \rightleftharpoons HO_2^-$	1.02	0.65 ± 0.16	[147]
$O_2 + 2\ H_2O + 4\ e^- \rightleftharpoons 4\ OH^-$	0.40	0.78 ± 0.28	[148]
$HO_2^\bullet + e^- \rightleftharpoons HO_2^-$	0.73	0.88 ± 0.24	[147]
$O_2^{\bullet -} + 2\ H^+ + e^- \rightleftharpoons H_2O_2$	1.73	0.92 ± 0.28	[147]
$O_2 + 2\ H^+ + 4\ e^- \rightleftharpoons 2\ H_2O$	1.27	0.98 ± 0.12	[148]
$H_2O_2 + 2\ H^+ + e^- \rightleftharpoons 2\ H_2O$	1.76	1.05 ± 0.25	[148]
$HO_2^\bullet + H^+ + e^- \rightleftharpoons H_2O_2$	1.46	1.18 ± 0.13	[149]
$OH^\bullet + e^- \rightleftharpoons OH^-$	1.83	1.95 ± 0.12	[147]

The reductive potentials vs. SHE using the Nernst equation for various in situ equilibrium conditions that are experimentally more relevant are additionally calculated. The average E_{NERNST} was calculated for the following conditions: $pH_{initial}$ 2.8, dose rates 10^6–10^{12} Gy/s, temperature 20–60 °C. From the reductive potentials of the half cells for Au and different radiolysis products, it is clear that the Au species can be reduced in the presence of e^-_{aq}, $H^\bullet$, H_2O_2, HO_2^-, H_2, $HO_2^\bullet$, $O_2^{\bullet -}$ and can be oxidized in the presence of $OH^\bullet$ radicals. The strongest reducing agents are e^-_{aq} ($E_{0=}$ -2.79 V_{SHE}, $E_{NERNST=}$ -2.28 ± 0.36 V_{SHE}) and $H^\bullet$ ($E_{0=}$ -2.23 V_{SHE}, $E_{NERNST=}$ -2.09 ± 0.15 V_{SHE}), which cause rapid metal precipitation,[150] while $OH^\bullet$ ($E_{0=}$ 1.83 V_{SHE}, $E_{NERNST=}$ 1.95 ± 0.12 V_{SHE}), as a strong oxidative agent, causes metal dissolution[44]. The reaction-rate coefficients between the radiolysis products and the Au species indicate that the $H^\bullet$, $OH^\bullet$ radicals, and e^-_{aq} have a much stronger effect on the gold species compared to the other solutes (Table 4.2).

Table 4.2 Reaction-rate constants of radiolysis products with gold species.

Au spec.	**Radiolysis spec**	k_{20} **°C** [$M^{-1}s^{-1}$]	E_A [**kJ/mol**]	$A_{calculated}$
Au^+	e^-_{aq}	8.0×10^9	12.98	1.64×10^{12}
	$H^\bullet$	8.0×10^9	15.09	3.91×10^{12}
	H_2O_2	0	0	0
	HO_2^-	1.89	25.8	7.46×10^4
	H_2	7.4×10^{-3}	94.1	4.28×10^{14}
	$HO_2^\bullet$	1.89	25.8	7.46×10^4
	$O_2^{\bullet -}$	1.89	25.8	7.46×10^4
Au^0	$OH^\bullet$	1.83×10^9	13.0	3.80×10^{11}

The primary aim of this study is to model and control the radical-induced redox chemistry in a LCTEM that is based on the precipitation/dissolution of Au NPs, which we used as a model system. Accordingly, we have simplified the model to a homogeneous system, which means the reduced Au species are introduced in the form of concentration and are all available for oxidation reactions. Additionally, it is assumed that all the Au ions are in the form of Au^+, as we want to observe only the transition between the Au^0 atoms and the Au^+ ions. The concentrations of the Au species are incorporated into the model like any other component, where the reaction-rate constants between the radiolysis products and the Au species were taken from Table 4.2. The corresponding rate of Au-species production is shown in equation 4.1:

$$\frac{dc_{Au^+}}{dt} = -\frac{dc_{Au^0}}{dt} = \sum_i k_{i-Au^0} c_i c_{Au^0} - \sum_i k_{i-Au^+} c_i c_{Au^+}, \tag{4.1}$$

where c_{Au^+} and c_{Au^0} represent the concentrations of gold ions and gold atoms, respectively. The reaction-rate constants for the reactions between the i compound with the gold species are indicated by k_{i-Au^0} and k_{i-Au^+}. Using this equation, we estimated that the steady-state, i.e., the equilibrium concentration of the gold species, is achieved after 10^{-3} s.

The resulting equilibrium ratio of $[Au^0]/[Au^+]$ in our model can be taken as an indicator of the reductive/oxidative ratio between the ionic, i.e., dissolved, and the solid, i.e., precipitated, gold. The latter will form in the liquid cell as Au NPs. These theoretically obtained values can be translated into the LCTEM experiment by assuming that the Au precipitation or dissolution is directly related to the equilibrium ratio $[Au^0]/[Au^+]$, thus providing the same kind of information. For example, a $[Au^0]/[Au^+]$ gradient increase indicates the gold's tendency for precipitation and growth, resulting in the formation of Au NPs. In contrast, a $[Au^0]/[Au^+]$ gradient decrease signifies either the inability of Au to precipitate or the dissolution of the already-formed Au NPs (Figure 4.7). These are the phenomena that can be easily observed during the LCTEM.

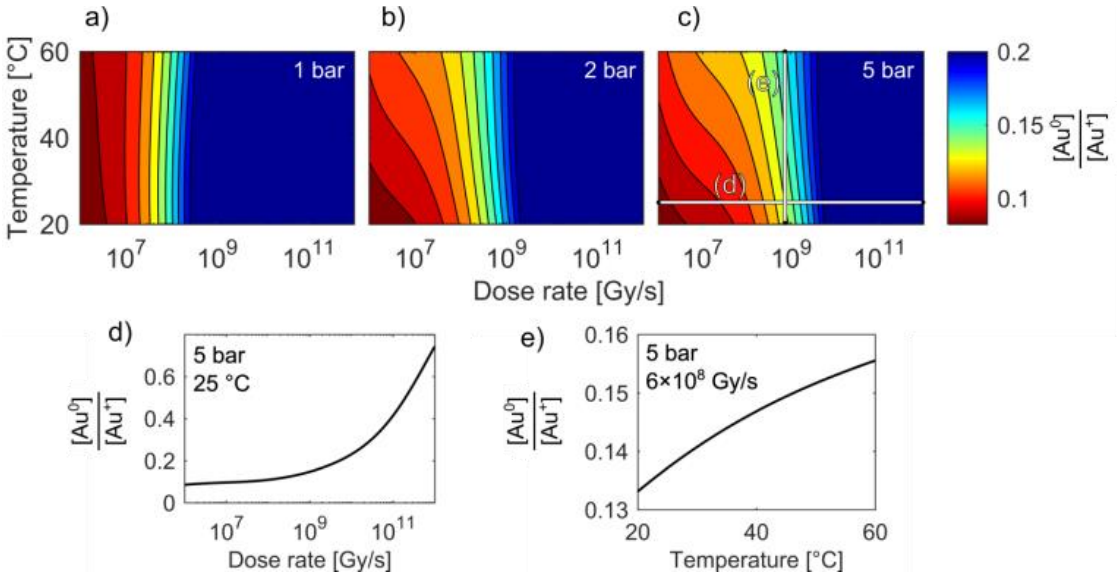

Figure 4.7: Temperature/Dose-rate Redox ratio (TDR) diagrams (a-c). Note that the stability regions for the equilibrium $[Au^0]/[Au^+]$ concentrations in the LCTEM are, in addition to dose-rate and temperature, also pressure dependent. Initial $[Au^+]$ = 1.5 mM, $pH_{initial}$ = 2.8. Figures d) and e) show sections of the Au redox ratio trends from diagram c).

Temperature/Dose-rate Redox ratio (TDR) diagrams, showing different redox $[Au^0]/[Au^+]$ stability regions, are shown in Figure 4.7. The TDR diagrams are calculated for the dose-rate range 10^6–10^{12} Gy/s, temperature range 20–60 °C, and at the H_2+O_2 pressures 1 bar, 3 bar, and 5 bar, with the molar ratio in the gaseous phase H_2/O_2 = 2. The resulting equilibrium redox concentration ratio of $[Au^0]/[Au^+]$ was obtained for an initial concentration of Au^+ species of 1.5 mM and a corresponding pH of 2.8. The calculated TDR diagrams are characterized with distinctive regions where the conditions in the LCTEM tend towards a reducing environment that will promote the precipitation of Au NPs (blue). In contrast, the oxidative environment (dark red) will either prevent the formation of Au NPs or promote the Au NPs' dissolution. The following "rainbow" color code indicates the intermediate conditions between the oxidative and reductive extremes.

When the pressure in the cell is set to 1 bar the temperature does not have any significant effect on the Au redox ratio (Figure 4.6). In that case, a change in the dose rate has a much larger impact on the Au redox ratio when compared with a temperature change. This implies that the precipitation of gold is positively and monotonously correlated with an increase in the dose rate, as was previously reported by Schneider et al. [43].

However, our results indicate that even at intermediate dose rates the saturation concentration for the solubility of H_2 and O_2 in the aqueous solutions will be exceeded and the radiolysis model is better defined by considering the elevated-pressure regimes inside the LCTEM system. The resulting model at elevated pressure (5 bars) indicates that the effect of temperature on the Au redox ratio starts to become significant, which is most pronounced at the low and intermediate dose rates that are typically used during LCTEM. The effect of the temperature on the redox conditions can be explained by the scavenging effect of the H_2 and O_2 species, i.e., H_2 is a strong $OH^\bullet$ scavenger, while O_2 is a strong scavenger of $H^\bullet$ and e^-_{aq}. Due to the presence of the gaseous phase, the concentrations of H_2 and O_2 are mainly dependent on the finite pressure and solubility limits. Moreover, with a temperature increase, the O_2 solubility will decrease at higher rates when compared to the H_2 solubility. As a result, a smaller amount of $H^\bullet$ and e^-_{aq} scavengers at higher

temperatures pushes the system towards more reductive conditions, as is evident in Figure 4.5 for pressures of 3–5 bars. The sensitivity analysis of the temperature-dependent part of the H_2 and O_2 solubility supports this explanation and is elaborated.

4.2.1.1 Model Verification by Low-Dose Experiments Using γ Radiation

Before the LCTEM, the model was validated with a quantitative comparison using literature reports [151]–[153] of radiolysis products obtained by irradiating water with low-dose γ-radiation. Electron radiation is a low-LET (linear energy transfer) radiation and is similar to γ-radiation. Hill [52] calculated the primary yields for different electron energies and observed constant yields above 10 keV. Temperature-dependent primary yields were obtained for water at neutral *pH* from Elliot and Bartels [140]. The experiments were performed at different dose rates and solute concentrations. Figure 4.8 shows different sets of experimental H_2O_2 concentration data obtained by irradiating water with low-dose γ-radiation under various experimental conditions as a function of time. It is worth mentioning that every data set is obtained from a different literature source [151]–[153]. Only the experimental data for concentration variations of H_2O_2, H_2, and O_2 are reported here. Individual experimental data points are represented by color-coded dots, while the corresponding color-coded solid lines are obtained from the kinetic radiolysis model developed in this study using the given low-dose γ-radiation experimental conditions. For example, Figure 4.8 shows the concentration variations of H_2O_2 for different initial concentrations of H_2, while Figure 4.8 shows H_2O_2 variations for different initial values of H_2O_2. Figure 4.8 indicates the concentration changes of H_2O_2 when varying the initial concentration of both H_2 and O_2. Remarkably, although not at the same time, our model accurately predicts the abrupt drop of the H_2O_2 concentration for the case of initial H_2 and O_2 concentrations of 7.31×10^{-4} and 7.50×10^{-5} M, respectively (shown in the yellow-coded color). By comparing the result of our kinetic radiolysis model with the experimental data for low-dose γ radiation (Figure 4.8) (~1 Gy/s), [151]–[153] it is evident that the proposed radiolysis model fits very well with the experimentally obtained data.

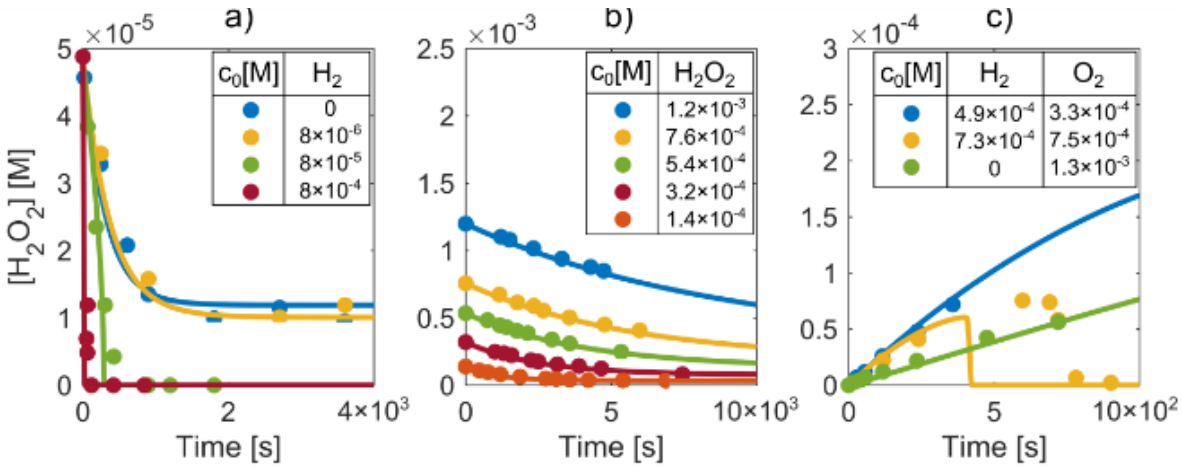

Figure 4.8: Determination of H_2O_2 concentrations during the irradiation of water with low-dose γ radiation for different initial a) H_2, b) H_2O_2, and c) H_2 and O_2 concentrations (marked by color-coded dots). The corresponding color-coded solid lines represent the prediction of our radiolysis model.

The conditions used for our model verification were collected from several sources [151]–[153] for the bulk water radiolysis in solutions of H_2O_2, O_2, and H_2 by using γ rays as a source of radiation, which is similar to electron radiation low-LET (linear energy transfer). The experiments were performed at different dose rates and solute concentrations (Table 4.3).

Table 4.3 Detailed conditions of the radiolysis model's verification.

source	**Line**	**Dose rate [Gy/s]**	T [°C]	c_{init} [M]			
				pH_{init}	H_2O_2	O_2	H_2
Pastina, LaVerne 2001 [151]	1	0.250	25	7	4.88×10^{-5}	0	0
	2	0.250	25	7	4.88×10^{-3}	0	8.00×10^{-6}
	3	0.250	25	7	4.88×10^{-5}	0	8.00×10^{-5}
	4	0.250	25	7	4.88×10^{-5}	0	8.00×10^{-4}
Hayon 1963[152]	1	0.205	25	7	1.20×10^{-3}	0	0
	2	0.205	25	7	7.57×10^{-4}	0	0
	3	0.205	25	7	5.35×10^{-4}	0	0
	4	0.205	25	7	3.20×10^{-4}	0	0
	4	0.205	25	7	1.39×10^{-4}	0	0
[153] Hochandel 1952 [153]	1	0.653	25	7	0	3.32×10^{-4}	4.90×10^{-4}
	2	0.653	25	7	0	7.50×10^{-5}	7.31×10^{-4}
	3	0.653	25	7	0	1.25×10^{-3}	0

4.2.1.2 General Model Description of Water Radiolysis:

The $O^{\bullet-}$, O_3, $HO_3^{\bullet}$, $O_3^{\bullet}$ species were not included in the model due to the lack of any corresponding kinetic data at higher temperatures. These species are predominantly formed in basic solutions. This is due to the deprotonation of the hydroxyl radical ($OH^{\bullet}$) into $O^{\bullet-}$ ($pK_a \approx 11$ [140]) and H_2O_2 into HO_2^- ($pK_a \approx 11$ [140]). The presence of the oxygen anion and the hydroperoxyl anion is responsible for the formation of the ozone anion and subsequently other ozonide species [140]. To justify the model's simplification, we calculated the ratio between the sum of the equilibrium concentrations of $O^{\bullet-}$, O_3, $HO_3^{\bullet}$, O_3^- and the equilibrium concentrations of the $OH^{\bullet}$ radical, using the correlations for equilibrium concentrations in a homogenous solution [43] at an initial pH 7 and 20 °C. At 10^{10} Gy/s (upper limit of the power-law model) the ratio is 0.012; therefore, there are approximately 80-times more $OH^{\bullet}$ radicals than other strong oxidizing species. Due to the

lower deprotonation rate at lower pH, the ratio of these concentrations is even lower, leaving the $OH^{\bullet}$ radical as the main strong oxidizing agent.

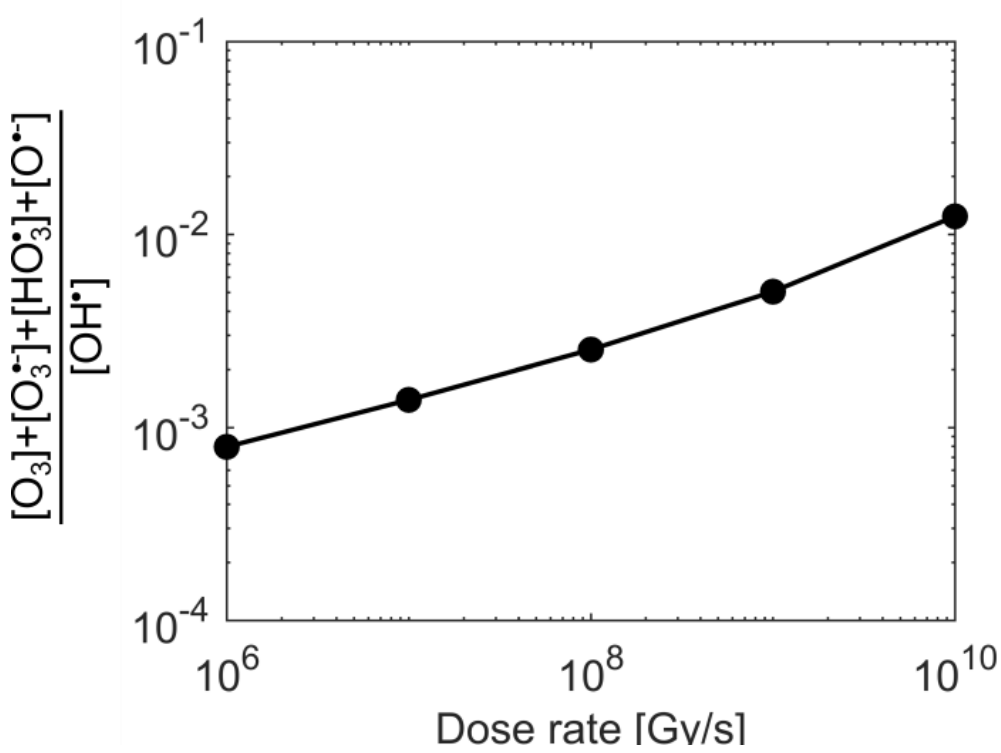

Figure 4.9: Validity of the simplification of the reaction scheme: the dose-rate dependence of the ratio of the equilibrium concentration between $O^{\bullet-}$, O_3, HO_3, O_3- and $OH^{\bullet}$ radicals at an initial pH = 7 and 20 °C.

According to the Arrhenius plots in Elliot et al. [140], all the reaction-rate constants linearly follow the relation $\ln(k) \propto T^{-1}$ below 100 °C. Therefore, the temperature dependence is written in the form of activation energies and pre-exponential factors. The processes in the irradiated matter can be described with a mass-balance equation with the reaction parts and the radiolysis primary yields:

$$\frac{dc_i}{dt} = -\sum_j k_{ij}\, c_i c_j + \sum_{j,k\neq i} k_{jk}\, c_j c_k + R_i, \tag{4.2}$$

where c_i represents the concentrations of the individual species, k_{ij} represents the reaction-rate constant and R_i represent the radiolytic yield. The first part of the right-hand side of the equation describes the consumption rate of the i compound, while the second part describes the formation of the i compound. The radiolytic yield R_i is the formation or consumption rate of the j compound by radiolysis.

$$R_i = \frac{\rho \psi G_i}{F}\ \left[\frac{M}{s}\right] \tag{4.3}$$

In the above equation 4.3, ρ represents the solvent density, F is the Faraday constant, ψ is the

the dose rate of the radiation and G_i is a G value, which represents the primary yield of the i compound in the first 1 µs from the start of the radiation. This value is given as a number of molecules created or destroyed per 100 eV of energy deposited. The G values depend on the type of radiation, the media exposed to the radiation, and the temperature. They are given in Table 4.4. The temperature dependence of the G values is calculated using linear interpolation.

The dose rate ψ is calculated from equation 4.4:

$$\psi = \frac{S\ 10^5 I_b}{\pi a^2}\ \left[\frac{Gy}{s}\right] \qquad 4.4$$

where S [MeV cm^2/g electron] is the density-normalized, stopping power in the medium, I_b is the beam current and a is the beam radius.

Table 4.4: Reaction-rate constants for the temperature range between 20 °C and 100 °C [140].

Reagents	**Products**	A [*]	E_A [kJ mol^{-1} K^{-1}]
$H^+ + OH^-$	H_2O_2	1.88×10^{13}	12.62
H_2O	$H^+ + OH^-$	1.70×10^{6}	62.37
H_2O_2	$H^+ + HO_2^-$	4.12×10^{6}	43.77
$H^+ + HO_2^-$	H_2O_2	5.59×10^{12}	11.73
$H_2O_2 + OH^-$	$HO_2^- + H_2O$	3.66×10^{12}	13.98
$HO_2^- + H_2O$	$H_2O_2 + OH^-$	4.54×10^{11}	31.74
$e^-_{aq} + H_2O$	$H^\bullet + OH^-$	5.58×10^{6}	31.73
$H^\bullet + OH^-$	$e^-_{aq} + H_2O$	8.52×10^{13}	37.36
$H^\bullet$	$H^+ + e^-_{aq}$	2.84×10^{12}	66.66
$H^+ + e^-_{aq}$	$H^\bullet$	1.98×10^{12}	11.17
$HO_2^\bullet$	$O_2^{\bullet-} + H^+$	2.63×10^{8}	14.58
$O_2^{\bullet-} + H^+$	$HO_2^\bullet$	5.59×10^{12}	11.73
$HO_2^\bullet + OH^-$	$O_2^{\bullet-} + H_2O$	7.13×10^{9}	60.93
$O_2^{\bullet-} + H_2O$	$HO_2^\bullet + OH^-$	3.66×10^{12}	13.98
$e^-_{aq} + OH^\bullet$	OH^-	2.64×10^{12}	10.65

$e^-_{aq} + H_2O_2$	$OH^\bullet + OH^-$	7.75×10^{12}	15.72
$e^-_{aq} + H_2O + O_2^{\bullet-}$	$HO_2^- + OH^-$	4.43×10^{10}	12.98
$e^-_{aq} + HO_2^\bullet$	HO_2^-	2.45×10^{12}	12.98
$e^-_{aq} + O_2$	$O_2^{\bullet-}$	2.53×10^{12}	11.66
$e^-_{aq} + e^-_{aq} + H_2O + H_2O$	$H_2 + OH^- + OH^-$	1.01×10^{10}	20.74
$e^-_{aq} + H^\bullet + H_2O$	$H_2 + OH^-$	2.06×10^{11}	14.93
$H^\bullet + H_2O$	$H_2 + OH^\bullet$	7.39×10^{12}	98.24
$H^\bullet + H^\bullet$	H_2	2.69×10^{12}	15.51
$H^\bullet + OH^\bullet$	H_2O	4.19×10^{11}	9.03
$H^\bullet + H_2O_2$	$OH^\bullet + H_2O$	1.76×10^{11}	21.01
$H^\bullet + O_2$	$HO_2^\bullet$	9.01×10^{11}	10.52
$H^\bullet + HO_2^\bullet$	H_2O_2	5.05×10^{12}	15.09
$H^\bullet + O_2^{\bullet-}$	HO_2^-	5.05×10^{12}	15.09
$OH^\bullet + OH^\bullet$	H_2O_2	9.78×10^{10}	7.48
$OH^\bullet + HO_2^\bullet$	$O_2 + H_2O$	1.31×10^{11}	6.68
$OH^\bullet + O_2^{\bullet-}$	$OH^- + O_2$	8.75×10^{11}	10.84
$H_2 + OH^\bullet$	$H^\bullet + H_2O$	6.55×10^{10}	18.45
$OH^\bullet + H_2O_2$	$HO_2^\bullet + H_2O$	7.72×10^{9}	13.82
$OH^\bullet + HO_2^-$	$HO_2^\bullet + OH^-$	1.00×10^{12}	11.92
$HO_2^\bullet + O_2^{\bullet-}$	$HO_2^- + O_2$	2.62×10^{9}	8.09
$HO_2^\bullet + HO_2^\bullet$	$O_2 + H_2O_2$	2.77×10^{9}	20.07

*for the reactions with one molecule the unit is $[s^{-1}]$, for two molecules $[M^{-1}s^{-1}]$, for three molecules $[M^{-2}s^{-1}]$ and for four molecules $[M^{-3}s^{-1}]$. We used 55.56 M as the molar concentration of water.

Table 4.5: Primary yields, G values, for the temperature range between 20 °C and 100 °C.

species	$G_{i\text{-}20}$ **°C** [N_i/**100eV**]	$G_{i\text{-}100}$ **°C** [N_i/**100eV**]	**Source**
e^-_{aq}	2.73	3.10	[140]
H^+	3.19	3.61	[a]
OH^-	0.46	0.51	[a]
H_2O_2	0.72	0.59	[140]
$H^\bullet$	0.60	0.71	[140]
$OH^\bullet$	2.75	3.57	[140]
H_2	0.43	0.47	[140]
H_2O	-4.65	-5.26	[b]

[a] H^+ primary yield is calculated using the ratio between $G(H^+)$ and $G(e^-_{aq})$ obtained from experimental measurements [154], [155] that are summed in the work of Hill and Smith [52]. Using this ratio the charge-balance yield $G(OH^-)$ to 0.46 at 25 °C and 0.51 at 100 °C, which is a similar value to $G(OH^-) = 0.50$ for low LET radiation. [151]

[b] Mass-balance calculation.

4.2.1.3 The Interaction Between the Radiolysis Products and the Gold Species in the LCTEM System:

Influence of chloride ions: the chloride is an $OH^\bullet$ scavenger. The main reaction product due to the presence of chloride is $ClOH^{\bullet-}$,[156] which is also a very strong oxidizer ($E_0(ClOH^{\bullet-}/(Cl^- + OH^-)) = 1.91\ V_{SHE}$[149]) and can also oxidize Au particles. Due to the large difference in the standard electrochemical potentials between $ClOH^{\bullet-}$ and Au^0, it is assumed that the rate of Au oxidation with $OH^\bullet$ and $ClOH^{\bullet-}$ is similar, which is approximated to a negligible influence on the trends of the Au oxidation state. However, for an accurate assessment of the chloride influence, all the significant reactions with the chloride species should be added.

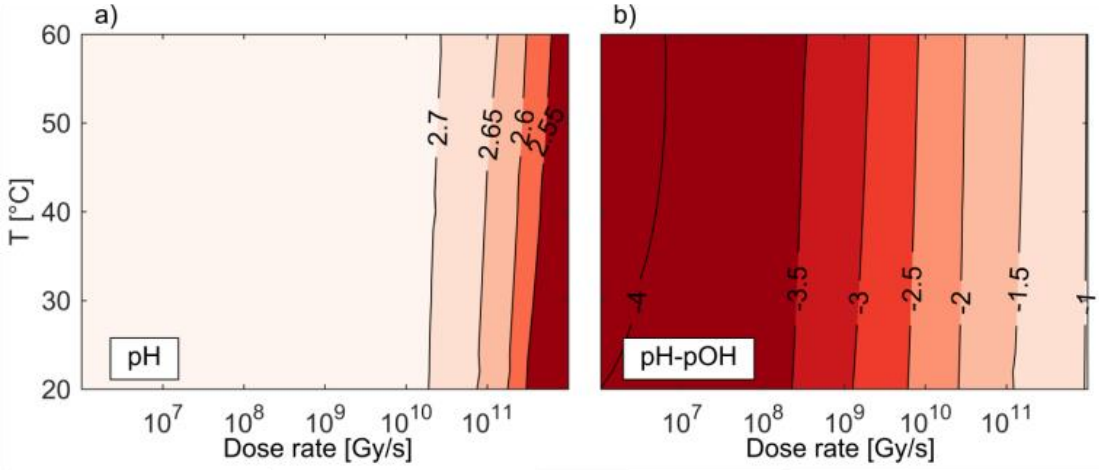

Figure 4.10 a) Equilibrium pH of the solution containing Au species. b) Equilibrium difference between pH and pOH. Initial pH = 2.8, maximum pressure 1 bar.

Calculation of pH and pOH (Table 4.6): The Au ions can form hydroxide species and other aureate species at higher values of pH (>7) and at high redox potentials [157]. In order to evaluate the most stable gold species for the set experimental conditions, the values of the pH and pH-pOH were calculated. The graph indicates that the pH is stable at the initial pH value of 2.8 for the broad range of dose rates from 10^6 up to 10^{10} Gy/s. Above the indicated dose rate the pH value decreases from 2.7 to 2.55, when the dose rate is increased from 10^{10} to 10^{12} Gy/s, respectively. Relative to the dose rate, it was concluded that the pH variations are not significantly influenced by a change of the temperature in the LCTEM. However, to determine the chemical state of the gold species the OH^- concentration is also important. The difference pH-pOH is equal to $\log_{10}([OH^-]/[H^+])$ and ranges between -4 and -1, mainly influenced by the changes in the dose rates. Due to the relatively low pH value (2.7-2.6) and the pH-pOH value between -4 and -1 (more acidic solution) at all dose rates and temperatures, this study confirms that the dissolved Au species are in the form $[AuCl_2]^-$.

Table 4.6: Reaction-rate constants of the radiolysis products with gold species.

Au spec.	Radiolysis spec.	$k_{20\ °C}$ [$M^{-1}s^{-1}$]	Reference	E_A [kJ/mol]	Reference	$A_{calculated}$
Au^+	e^-_{aq}	8.0×10^9	[150]	12.98[b]		1.64×10^{12}
	$H^\bullet$	8.0×10^9 [a]	[150]	15.09[c]		3.91×10^{12}
	H_2O_2	0 [j]	[158]	/	[158]	0
	HO_2^-	1.89[d]	[158]	25.8 [d,e]	[158]	7.46×10^4
	H_2	7.4×10^{-3} [d, f]	[159]	94.1[d,g]	[160]	4.28×10^{14}
	$HO_2^\bullet$	1.89 [d,h]		25.8 [d,h]		7.46×10^4

	$O_2^{\bullet-}$	1.89 [d,h]		25.8 [d,h]		7.46×10^4
Au^0	$OH^\bullet$	1.83×10^9 [i]		13.0 [i]		3.80×10^{11}

[a] Assumed the same k_{20} °C, as for the reaction between e^-_{aq} and Au^+, because the reaction rate constants of $Au^{+3}+H^\bullet / e^-_{aq} \rightarrow Au^{+2}+H^+/H_2O$ are similar ($(5.7 +/- 1.5) \times 10^9$ $M^{-1}s^{-1}$ [150]).

[b] E_A assumed the same as for the reaction $e^-_{aq}+O_2^{\bullet-}(+ H_2O)\rightarrow HO_2^-+OH^-$ because both reactions are diffusion-controlled and $O_2^{\bullet-}$ as the $[AuCl_2]^-$ negatively charged.

[c] E_A assumed the same as for the reaction $H^\bullet + O_2^{\bullet-}\rightarrow HO_2^-$, because both reactions are diffusion-controlled and $O_2^{\bullet-}$ is as the $[AuCl_2]^-$ negatively charged.

[d] Rate for the presence of a gold catalyst, as given in the literature.

[e] E_A from the overall observed constant is used (apparent activation energy). [158]

[f] Rate expression $k[Au^0][H_2]$, at $pH = 7$ [159].

[g] E_A assumed for the H_2 dissociation on Au (211) [160], since it is the dissociation step.

[h] Assumed the same rate and activation energy as for the reaction $HO_2^-+Au^+\rightarrow HO_2^\bullet+Au^0$. $HO_2^\bullet$ and $O_2^{\bullet-}$ are thermodynamically much stronger reducing agents (E_{NERNST} = -0.27 and 0.05 respectively (Table 4.1)) than HO_2^- (E_{NERNST} = 0.65 (Table 4.1)). However, in the density functional theory (DFT) study on Au (111) [161] they show, that the reaction $H_2O_2^*\rightarrow HO_2^*+H^*$ has a lower activation energy (E_A = 113 kJ/mol, ΔE = 106 kJ/mol) than the reaction $HO_2^*\rightarrow O_2^*+H^*$ (E_a = 141 kJ/mol, ΔE = 85 kJ/mol). Also, it is found that at higher pH (10-13) the reduction of $HauCl_4$ with H_2O_2 is more significant and much faster than at neutral pH (7–8)[158]. This can be due to a larger amount of HO_2^- and $O_2^\bullet$. The electron-transfer reactions are generally fast, and it is expected that $O_2^\bullet$ will reduce the Au species with a rate similar to $H^\bullet$ or e^-_{aq}. However, in the case of low pH, $O_2^\bullet$ is protonated to $HO_2^\bullet$, which needs to be broken on the Au surface to form O_2 and H*, and this is a much slower process, as seen from the DFT calculations[161]. Because of the lack of experimental data on the kinetics of $HO_2^\bullet$ and $O_2^{\bullet-}$ with Au^+ we assume the same rate as for the case of the reaction of HO_2^- with Au^+. However, for the experiments at high pH, where the amounts of HO_2^- and $O_2^\bullet$ are significant, corrected reaction rates should be used.

[i] Assumed the same rate coefficient as for the reaction of $Au^+ + OH^\bullet \rightarrow Au^{+2} + OH^-$. The rates of dissolution of Au^0 with a strong oxidizing or complexing agent without stirring are usually diffusion controlled [162]. Because of zero stirring, the reaction is diffusion controlled. For the case of the dissolution of Au in a cyanide solution, the activation energies are 12–21 kJ/mol [162]. The temperature dependence of the diffusivity constant for water self-diffusion, which is similar to the $OH^\bullet$ diffusion constant, is used to calculate the activation energy [140].

[j] The value is 0 because the mechanism of Au-ion reduction proceeds through HO_2^- [158]. In the kinetic model, we have already included the reversible reaction between H_2O_2 and HO_2^-, and therefore the contribution to the reduction of the H_2O_2 is 0.

4.2.1.4 Explanation of Redox Trends Due to Temperature Change:

The influence of the temperature on $[Au^0]/[Au^+]$ increases with increasing pressure (Figure 4.5) which points to the influence of the H_2 and O_2 solubility in the liquid phase. The temperature dependence of the O_2 solubility is significantly higher when compared with the solubility of H_2 in water (Table 4.7).

Table 4.7: Solubility of the H_2 and O_2 gases in water.

T	$\frac{1}{K_H}\Big\vert_{O_2}\left[\frac{mol}{L\ bar}\right]$	$\frac{1}{K_H}\Big\vert_{H_2}\left[\frac{mol}{L\ bar}\right]$
20 °C	1.40×10^{-3}	8.08×10^{-4}
60 °C	0.88×10^{-3} (decreased by 37% relative to 20 °C)	7.28×10^{-4} (decreased by 9.9% relative to 20 °C)

To prove the impact of the solubility's temperature dependence we performed a sensitivity analysis for the temperature-dependent part of the solubility relation (of both gases at the same time). We calculated the Au redox ratios for the different *factor* values: 0.5, 1, and 2:

$$H_i(T(K)) = \exp\left(-A + \frac{B}{factor(T - 293.15\ K) + 293.15\ K}\right. \\ \left. + C\log_{10}((factor(T - 293.15\ K) + 293.15\ K)/100))\ \frac{55.5\frac{mol}{L}}{1\ bar}\right. \quad (4.5)$$

Table 4.8: Parameters of the temperature-dependent Henry constant [163], [164].

Coef.	**H_2**	**O_2**
A	48.1611	66.7354
B	5528.45	8747.55
C	16.8893	24.4526

From Figure 4.11 we can see that the temperature dependence of the solubility influences the Au redox ratio. When we increase the temperature dependence of the gases' solubility (factor = 2) the redox ratio increases faster with temperature, and when we decrease the temperature dependence of the gases solubility (factor = 0.5) the redox ratio increases more slowly. The concentration of O_2 in the liquid phase decreases much faster than the concentration of H_2. Because H_2 is a strong $OH^{\bullet}$ radical scavenger ($k_{20\ °C} = 3.4\times10^{7}\ M^{-1}s^{-1}$) and O_2 is a strong scavenger of $H^{\bullet}$ and e^-_{aq} ($k_{20\ °C} = 1.2\times10^{10}$,$2.1\times10^{10}\ M^{-1}s^{-1}$, respectively),

the ratio $\frac{[H^\bullet]+[e^-_{aq}]}{[OH^\bullet]}$ (consequently Au redox ratio), depends on the concentrations of O_2 and H_2.

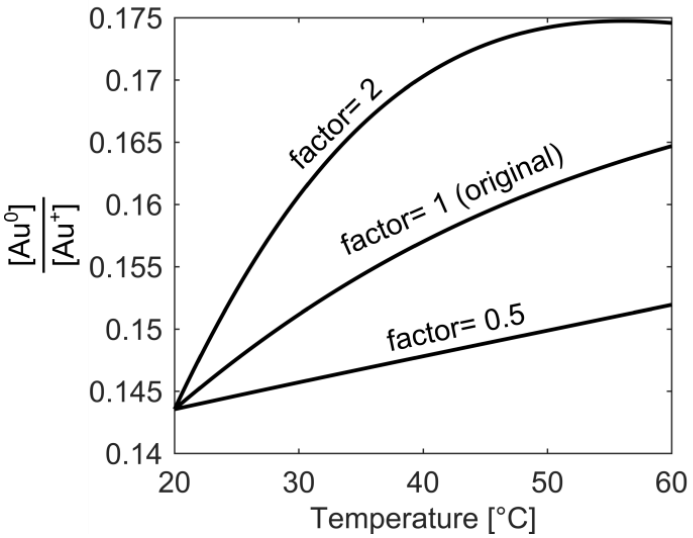

Figure 4.11: Temperature dependence of the Au redox ratio at different sensitivity factors of the H_2 and O_2 solubilities. Dose rate 10^9 Gy/s, total concentration of gold species is 1.5 mM with an initial pH 2.8, and pressure 5 bar.

4.3 LCTEM Nanoparticle Synthesis

4.3.1 Synthesis of Gold Nanoparticles

Figure 4.12 shows a time sequence of the precipitation and dissolution dynamics of Au NPs at a constant dose rate of 10^9 Gy/s and a temperature of 20 °C. A region where representative Au NPs exhibit precipitation, growth, and dissolution on a time scale of 5 s is marked by an arrow or a dashed-line circle. At time 0 s, the Au NPs are not yet formed, it appears at 1.8 s., and remains stable for a period of approximately 3 s, followed by complete dissolution at 5.1 s.

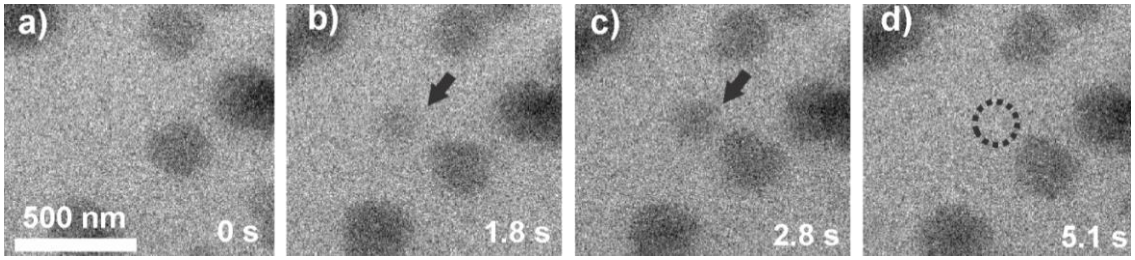

Figure 4.12: TEM micrographs indicating the precipitation and dissolution of Au NPs at a constant dose rate of 10^9 Gy/s and a temperature of 20 °C. The encircled areas and arrows indicate the sequence of precipitation and dissolution for a single Au NP under equilibrium conditions.

Knowing the equilibrium conditions from the previous experiment, we started to verify the proposed radiolysis model of radical-induced redox chemistry in the LCTEM by varying the electron dose rate at ambient temperature. The results of the experiment are shown in Figure 4.13. The experimental dose rate was set to 10^8 Gy/s, just below the expected dose

rate of the Au NPs' precipitation, as determined in the previous experiment. Accordingly, at the dose rate of 10^8 Gy/s no NPs were formed. After 12 seconds the dose rate was increased from 10^8 Gy/s to 10^{12} Gy/s for a period of 15 s, which initiated the precipitation of the Au NPs, reaching their average size of 60 nm. After this period, the dose rate was rapidly reduced back to the initial 10^8 Gy/s. At that point, the Au NPs start to shrink, and in less than 10 s the NPs were completely dissolved. The experiment was repeated at the same observation area 100 s later to verify whether the phenomenon was repeatable. In this new experiment, the area was exposed with a dose rate of 10^{12} Gy/s for 5 s, instead of 15 s, as in the previous experiment. A shorter exposure time resulted in the formation of NPs with an average size of 20 nm. When the dose rate was decreased for the second time to 10^8 Gy/s, NPs were again dissolved in approximately 10 s. A quantitative evaluation of the whole experiment is presented in Figure 4.13. It shows the variations of the Au NPs' size as a function of the electron dose rate at room temperature. The black line in the image represents the selected dose rate, while the circles symbolizes the measured average size of the NPs. These results confirmed that the electron dose-dependent LCTEM experiments are highly reversible and correlate with the predictions obtained from the TDR diagrams, where the Au NPs' precipitation or dissolution at ambient temperature is positively correlated with the variations of the Au redox concentration ratio, i.e., $[Au(0)]/[Au^+]$ as a function of the electron dose rate. Similar precipitation/dissolution trends were also observed in previous studies by Schneider et al. [43] and Ahn et al. [36].

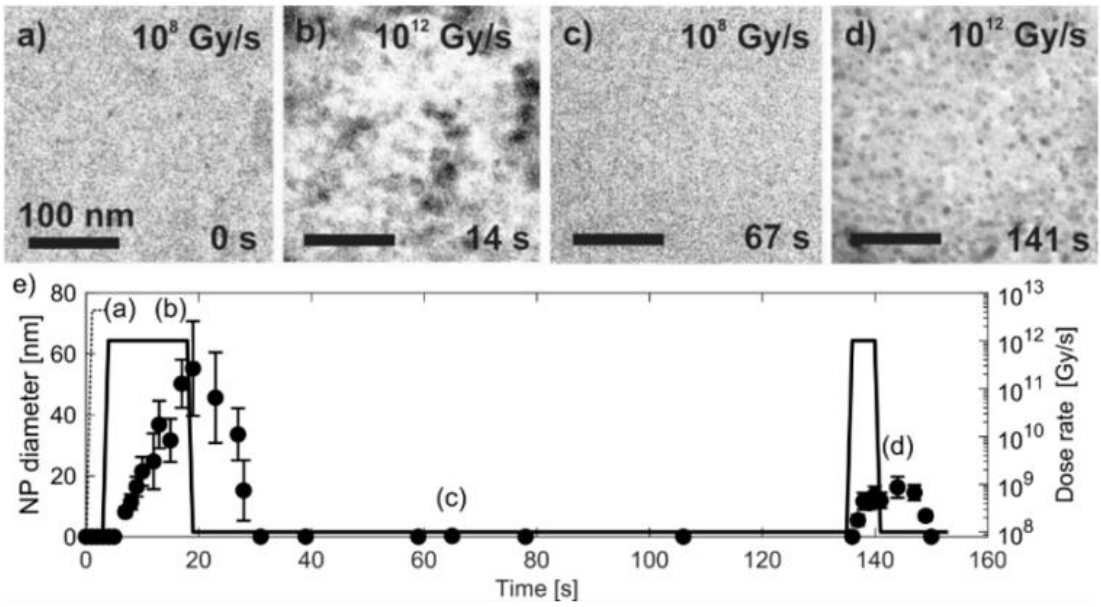

Figure 4.13: Time-sequenced TEM micrographs acquired from the same specimen area at 25 °C and different electron dose rates (a) 10^8 Gy/s, (b) 10^{12} Gy/s, (c) 10^8 Gy/s, (d) 10^{12} Gy/s (e). Corresponding graphical representation of the Au NPs precipitation and dissolution. The average NPs diameters at every indicated time slot were determined from 10 NPs.

In the next set of the experiments the electron dose rate was fixed at $6*10^8$ Gy/s, at an initial temperature of 20 °C, just below the experimentally determined boundary conditions for the Au NPs' precipitation. The temperature-dependent experiment started at 25 °C, where the same specimen area was observed for 300 s (Figure 4.14), which is a several orders of magnitude longer time than needed to reach the equilibrium concentration of the

radiolysis species [165]. This experiment demonstrates that the Au-based aqueous solution is stable at electron dose rates of around 10^8 Gy/s and 20 °C. After a relatively long exposure to the observed specimen area, the temperature was initially increased to 30 °C for a period of 81 s. These conditions did not yield any Au NPs precipitation, which is in accordance with the relatively broad $[Au^{(0)}]/[Au^+]$ gradient field in the temperature domain, as indicated in the TDR diagrams at elevated pressures. When the temperature was increased to 40 °C (t=556s) the Au NPs started to form with an average diameter of around 20 nm (Figure 4.14b). When the temperature was decreased back to 25 °C, these precipitated Au NPs were completely dissolved (t=734 s) (Figure 4.14c). The reversibility of the phenomenon was again checked by the repeated temperature variations. First, the temperature was raised again to 40°C (t=923s), which resulted in the precipitation of Au NPs with an average diameter of around 20 nm (Figure 4.14d). After that, the temperature was lowered back to 25 °C (t=1146s) and the previously precipitated Au NPs were again completely dissolved (Figure 4.14e), thus confirming the temperature-dependent reversibility of the Au precipitation-dissolution mechanism.

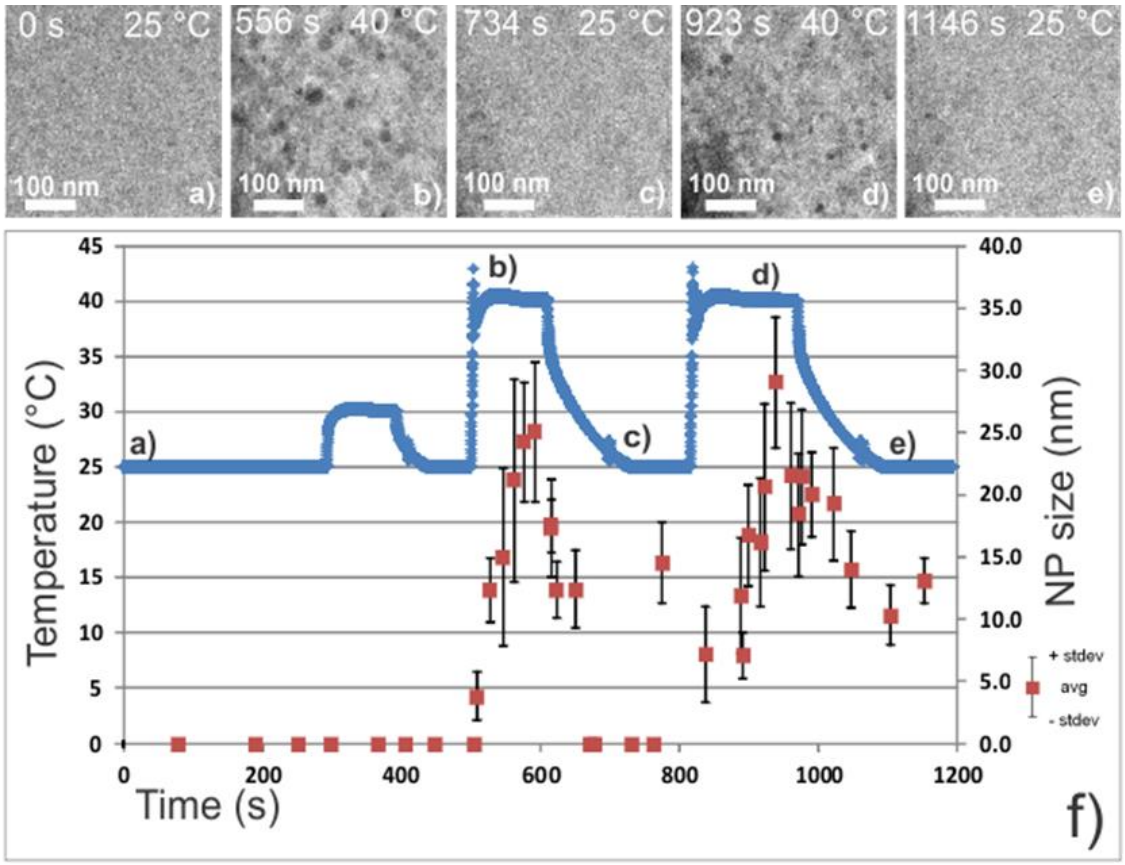

Figure 4.14: TEM micrographs of the precipitation/dissolution trends of Au NPs as a function of temperature variations between 25 °C and 40 °C on a progressive time scale. Time-sequenced TEM micrographs acquired from the same specimen area at a fixed electron dose rate of $6*10^8$ Gy/s and different temperatures of (a) 25°C, t=0, (b) 40°C, t=556s, (c) 25°C, t=734s, (d) 40°C, t=923s and (e) 25°C, t=1146s (f). The temperature-time profile is indicated by the blue line. The average NPs diameters at every indicated time slot were determined from 10 NPs.

These observations contradict the basic understanding of precipitation/dissolution trends that would typically be observed in comparable ex situ tabletop experiments, if we neglect

the radiolysis-induced redox chemistry. Namely, it is well accepted that the precipitation of Au NPs from a Au aqueous solution at low pH values is typically provoked by the elevated temperature [43].

However, this process is not reversible and cannot lead to Au NPs' dissolution during a temperature drop in the system. Consequently, this phenomenon can only be explained by the fact that temperature changes provoke significant variations in the equilibrium concentration of the radiolysis species, yielding substantial changes to the Au redox concentration ratios, finally resulting in the reversible precipitation/dissolution of Au NPs. These experimental results are therefore consistent with the [Au(0)]/[Au^+] trends indicated in the TDR diagrams for elevated pressure values.

The ex situ SAED and EDS analyses confirmed that the observed NPs belong to face-centered cubic gold (Figure 4.15).

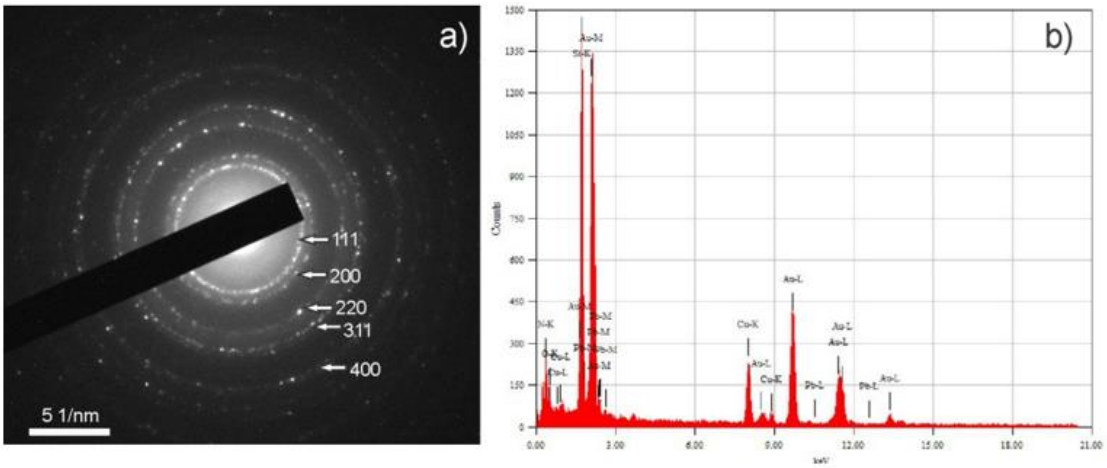

Figure 4.15: TEM analysis of Au NPs of air-dried samples. a) SAED analysis shows they are FCC Au (ICSD = 52249), b) which was confirmed with an EDS analysis.

4.3.2 Synthesis of Yttrium Nanoparticles

For the synthesis of yttrium oxide NPs, the method of Qin et al. [68] was used. For this method, a water-based solution of urea and yttrium acetate hydrate (YAc) is used. Urea decomposes in the water at elevated temperatures. Urea is not stable in water at temperatures above 83 °C. The decomposition rate of urea was precisely controlled by its heating temperature. For example, the decomposition constant of urea in the water at 25 °C is calculated to be 6.65 x 10^{-8}/s, which is about 1/15000 of its value at 90 °C [87]. The activation energy for this decomposition process is 135.5 kJ. Details on decomposition mechanism are given in equations 3.1-3.4.

Before the LCTEM experiments, the experiments were performed ex situ under normal laboratory conditions. At first, we have made a solution of deionized water and YAc. A few drops of 0.2 molar sulphuric acid (H_2SO_4) was added so that the pH of the solution reached 4.5. Only at this pH did the YAc dissolve completely. We further dissolved YAc using ultrasonication. When YAc was fully dissolved, urea was added into the solution. In the experiments, the YAc concentration was fixed. We have varied the concentration of urea and the temperature. Our goal was to find the ratio where nucleation would occur quickly (few minutes) and at a temperature < 100 °C. To achieve conditions for homogenous nucleation stirring inside the holder is not possible; so, we also did not stir in our ex situ experiments. Our experiments showed that the best ratio for our liquid cell

TEM is: 1: 20:5555 = YAc: Urea: Deionized water solution. At this ratio, particles do appear in 15 min at 80 °C. So, this solution was chosen for our first in situ LCTEM experiments. Our ex situ experiments (Table 4.9) proved that at a higher temperature, particles precipitate faster. This is because urea decomposes faster. Also, a higher urea concentration in the solution, speeds up the reaction and subsequent precipitation of the yttrium-based NPs, following this simplified reaction in an acid solution:

$$Y^{3+} + OH^{-} + CO_3^{2-} \xrightarrow[T>80\ ^\circ C]{} Y(OH)CO_3 \tag{4.6}$$

Table 4.9: Results of several different experiments for yttrium nanoparticle growth

Solution	The ratio of the reactants			Magnetic stirring	Temperature (°C)	The outcome of the nanoparticle synthesis
	YAc	Urea	H_2O			
Solution 1	1	10	5555	Yes	95	Particles appeared after 90 min
Solution 1	1	10	5555	No	95	No particles
Solution 1	1	10	5555	No	60	No particles
Solution 2	1	20	5555	No	60	No particles
Solution 2	1	20	5555	No	80	Particles appeared after 15 min
Solution 3	1	100	5555	No	60	No particles
Solution 3	1	100	5555	No	95	Particles appear after 1 min

For the experiment, chips with 150-nm static spacers were used, where a 2.5-nm point-to-point resolution was achieved.

During the initial ex situ experiments a solution with a molar ratio of 1:20:5555 = YAc: Urea: water was used, and the solution was heated to 80 °C in a glass beaker. First, visually observed particles formed after 15 min of heating at 80 °C. At that moment, the solution was quenched in cold water. Subsequent SEM analyses showed the particles were spherical and monodispersed (Figure 4.16) with an average size of 300-500 nm. EDS and XRD analysis confirmed they are amorphous yttria (Figure 4.16). This is in accordance with previous studies reported in the literature, the as-synthesized NPs being an amorphous $Y(OH)CO_3$ [68], neglecting the $Y_2(CO_3)_3$, which is less likely to be formed [166].

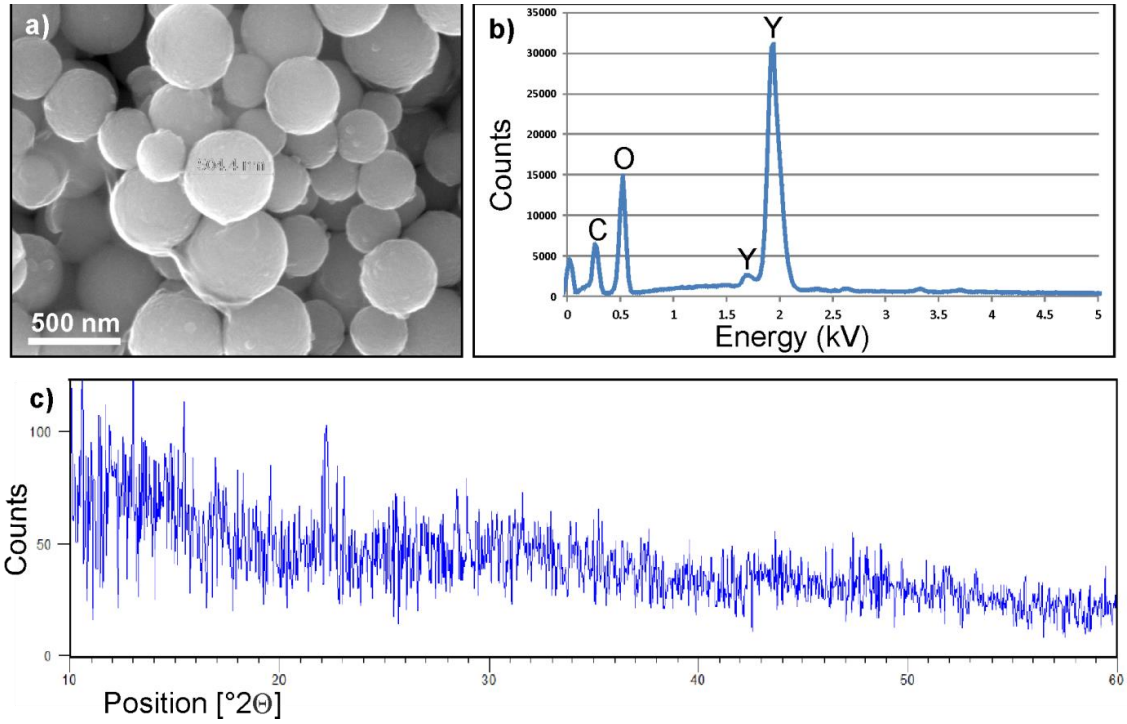

Figure 4.16: Amorphous yttria NPs synthesized using a conventional approach a) SEM, b) EDS, c) XRD.

Transformation of amorphous yttria into the crystalline phase was observed indirectly, by annealing as-synthesized NPs (Figure 4.17) in an oven for 2 h at 700 °C in an oxygen-rich the atmosphere. A subsequent TEM/SAED analysis showed that annealing transformed initial amorphous NPs (Figure 4.16) into crystalline $Y(OH)_3$ (ICSD=24309) (Figure 4.17).

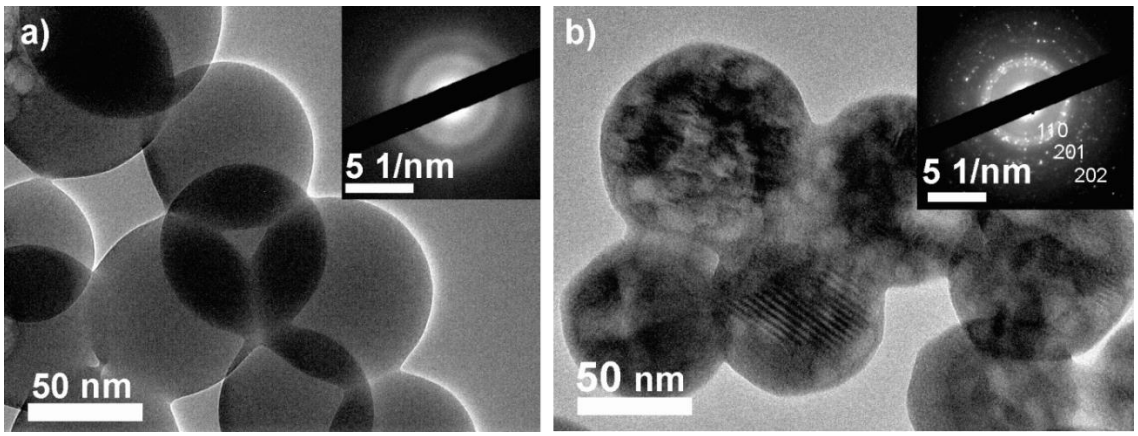

Figure 4.17: Ex situ synthesized yttria: a) before annealing, b) after annealing for 2 h at 700 °C

The same solution as in the ex situ experiments (1: 20: 5555 = YAc: Urea: water) was also used in the LCTEM experiments. The solution was in situ heated to 80 °C (same temperature as in the previous ex situ experiments) in the LCTEM cell at a dose rate of 5000 $e^-/nm^2/s$. 350 s after the temperature of 80 °C was reached (Figure 4.18) the first

NPs precipitated (Figure 4.18). The NPs continued to grow for 150 s once they reached the maximum size of 100 nm (Figure 4.18).

TEM analyses revealed the NPs are amorphous yttria (Figure 4.18), chemically and crystallographically identical to the NPs formed with conventional ex situ experiments. The NPs formed with the LCTEM technique are $1/10^{th}$ of the size of the particles formed using the conventional approach. This is probably due to the effect of the confinement of the liquid cell.

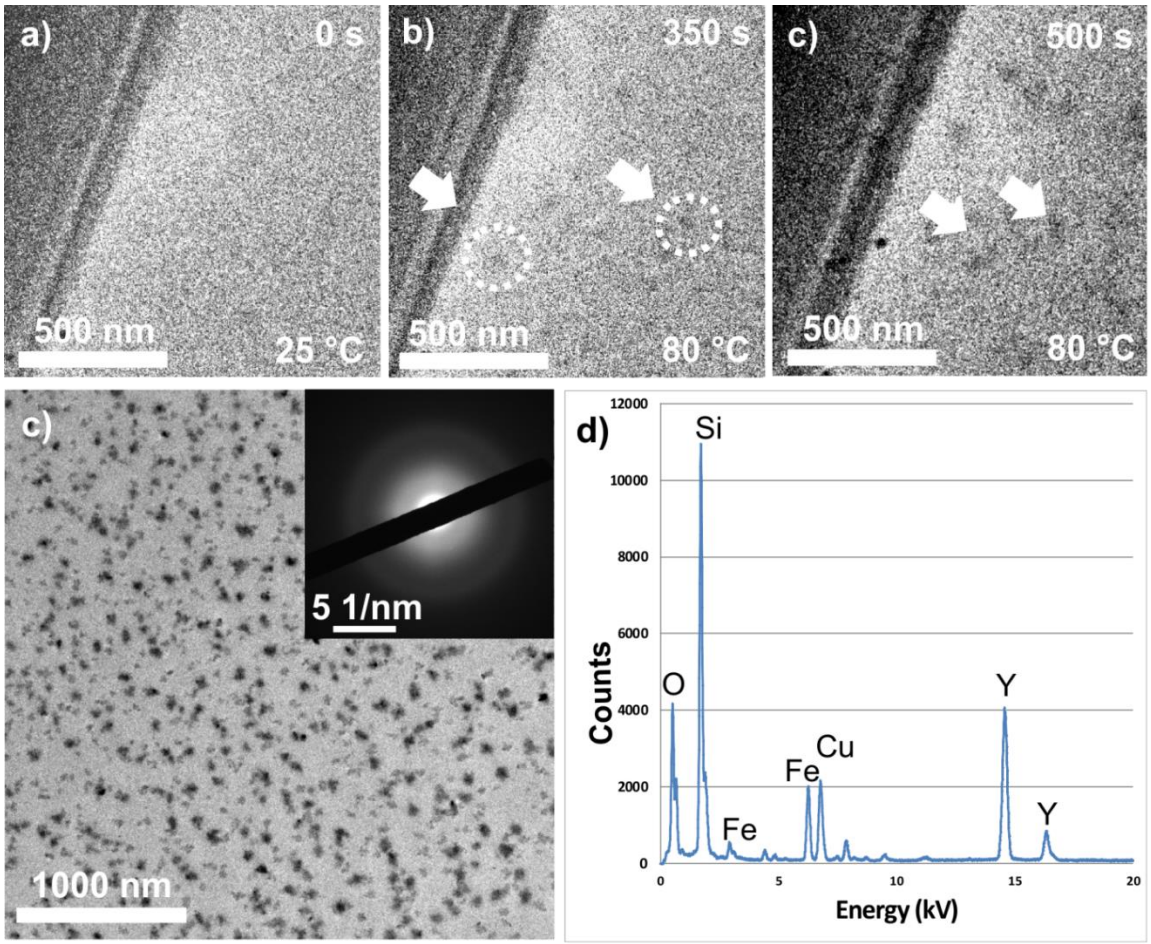

Figure 4.18: The sequence of frames showing the process of synthesizing yttrium NPs using the LCTEM technique (a-c). The black straight part is the edge of the Si chip, which is not transparent to electrons. TEM analyses using SAED (c) and EDS (d) confirmed that the NPs are amorphous yttria.

When the NPs stopped growing the liquid cell was disassembled and the chips were carefully rinsed with water. The chips were then annealed at 700 °C for 2 h, placed in a modified holder and subsequently analyzed using conventional TEM. The SAED analysis of the annealed (700 °C for 2 h) chips showed that amorphous NPs in the process of the calcination became crystalline yttrium hydroxide $Y(OH)_3$ (ICSD = 24309) (Figure 4.19), the same as in the conventional ex situ experiments (Figure 4.17).

In the literature, it was reported that the transformation happens at 700 °C [79] and that hexagonal yttrium hydroxide forms at 90 °C, which is further transformed into yttrium oxide at 800 °C [167].

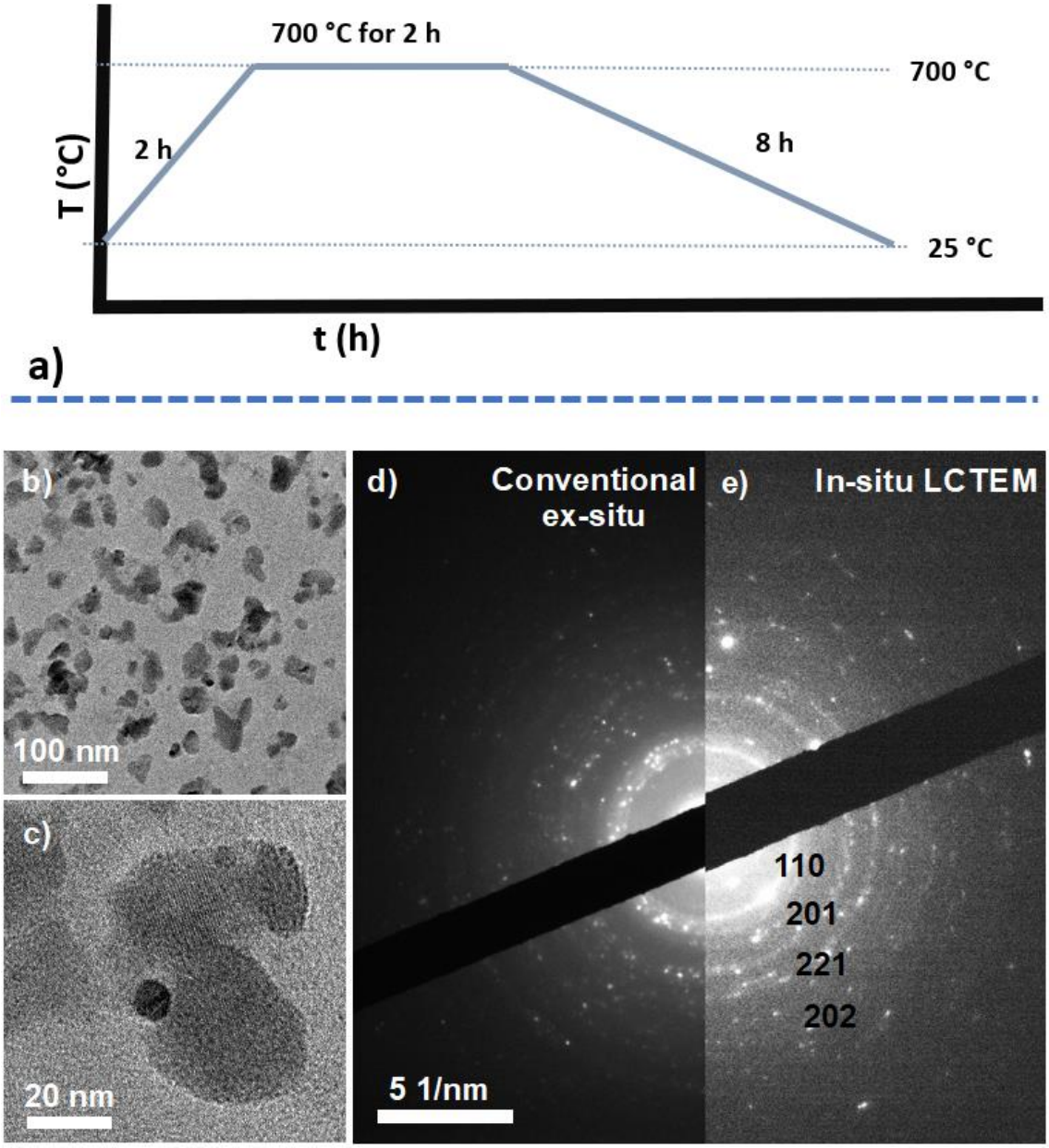

Figure 4.19: a) Annealing profile of amorphous NPs that were synthesized both conventionally and using LCTEM. Amorphous NPs (b) synthesized with LCTEM become crystalline $Y(OH)_3$ (ICSD = 24309) (d-e) after annealing for 2 h at 700 °C. In situ (conventional) synthesized NPs (d) are the same as the as-synthesized using the in situ LCTEM technique (e).

Conventional ex situ experiments and LCTEM experiments both yielded the precipitation of amorphous yttrium NPs. After the process of annealing for 2 h at 700 °C, in both cases the NPs were transformed into crystalline yttrium hydroxide. This is believed to be one of the first reports of the synthesis of ceramic powders using the LCTEM technique.

4.3.3 Electrochemical Synthesis of Iron Nanoparticles

For the electrochemical synthesis of Fe NPs, the following electrolyte was prepared: 5 mmol/L $FeSO_4$ was added into the 5 mmol/L Na_3-Citrate and 10 mmol/l Na_2SO_4 solution. The pH of the electrolyte was measured to be 2.8. Firstly, the liquid cell experiments were performed ex situ in an ex situ electrochemical cell (see Section 3.1.7 for more details). The CV measurement was performed in the potential range from -2 V in the forward scan. Then the scan was reversed back to 1 V. For this CV experiment, 3 cycles were collected at a scan rate of 100 mV/s. As seen from Figure 4.20, three cathodic and one anodic peaks were observed indicating different events. In the forwards scan, the first increase in the cathodic current was observed at -1.55 V / -1.6 mA and represents the hydrogen evolution reaction (H_2O is reduced to H_2). The next increase in the cathodic current was observed at -1.1 V / -1.1 mA, where the reduction of Fe^{2+} to Fe^0 resulted in the deposition of Fe NPs. At -0.8 V / - 0.6 mA the H_2 gas evolution occurs. At 0.4 V / -0.1 mA O_2 gas is reduced to the O^- ion. In the reverse scan, the current increase in the anodic region (at -0.8 V / 0.5 mA) represents the oxidation of Fe^0 to Fe^{2+}.

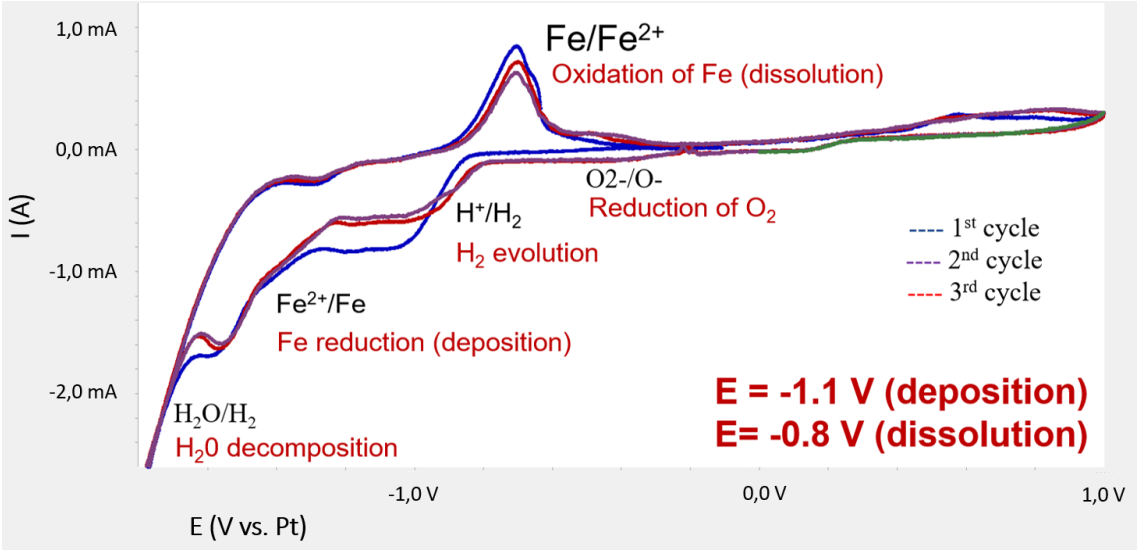

Figure 4.20: CV voltammogram of the ex situ synthesis of Fe NPs.

After a successful ex situ experiment, in situ LCTEM experiments were performed using the same solution. The CV voltammogram (Figure 4.21) shows the presence of the reduction peak of Fe^{2+} to Fe^0 at the potential of -0.8V / -12 mA, which is in agreement with the ex situ experiments. At -0.55 V/ -12mA H^+ to H_2 (hydrogen-evolution reaction occurs) and at -0.3 V / -8 mA Fe^{3+} to Fe^{2+} reduction. Furthermore, at 0.1 V / 0 mA O^{2-} /O^- occurs. In the anodic region a dissolution peak at -0.8 V Fe^0 to Fe^{2+} was not observed. This could be due to the effect of the liquid cell's size confinement.

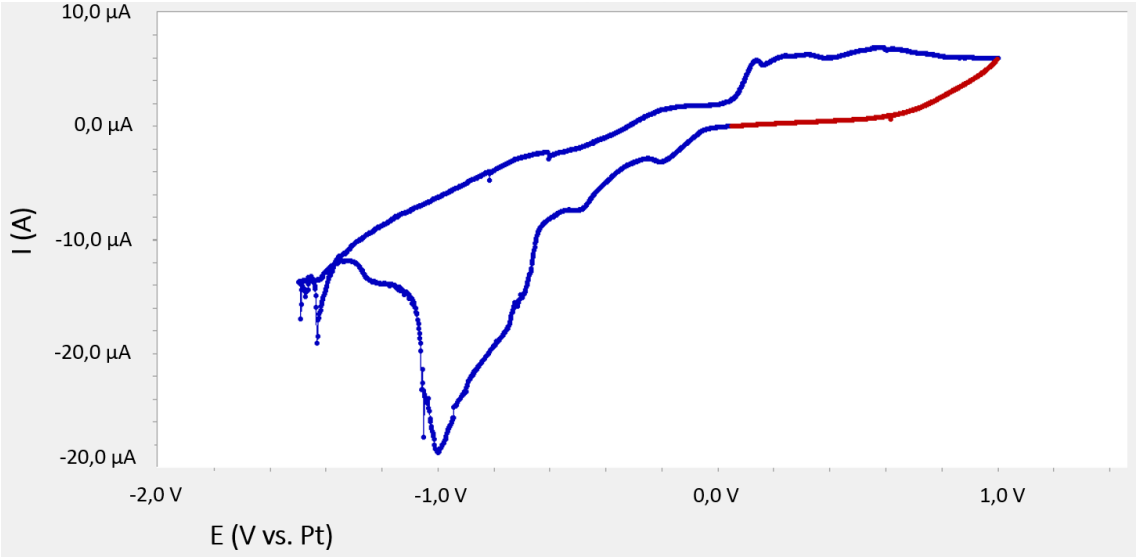

Figure 4.21: CV voltammogram of LCTEM synthesis of Fe NPs.

On the basis of the CV voltammograms (Figure 4.21),), the potential for Fe NPs' deposition was selected to be E= -1.1. Also, the dissolution potential was selected to be E= - 0.8 V. To minimize the effect of radiolysis, the solution was observed only during the imaging. During all the other sections of the experiment, the electron beam was blocked with a condenser aperture.
Applying the potential of -1.1 V vs. Pt for 1500 s (Figure 4.22) stimulated the electrodeposition of islands of Fe, preferably at the edges of the glassy carbon working electrode. The nucleation of the crystal growth occurred instantaneously upon reaching a critical potential. The resulting deposition is discontinuous. Switching the potential to -0.8 V vs. Pt leads to the dissolution (Figure 4.22) of the previously formed species. After 300 s (Figure 4.22a) of applying the dissolution potential, the Fe NPs began to dissolve. After 1200 s (Figure 4.22b) the NPs were almost completely dissolved. The remains of Fe NPs after the experiment could indicate an irreversible electrochemical reaction in the charge-discharge process, as noted by Su et al. [168].

After the above-mentioned experiment, the potential was switched back to -1.1 V (deposition potential) (Figure 4.22c). It facilitated the precipitation of NPs in the same area, where previously NPs were dissolved. When the potential was reversed to the dissolution potential for the second time (Figure 4.22) the NPs were dissolved, indicating that these experiments are reversible and repeatable.

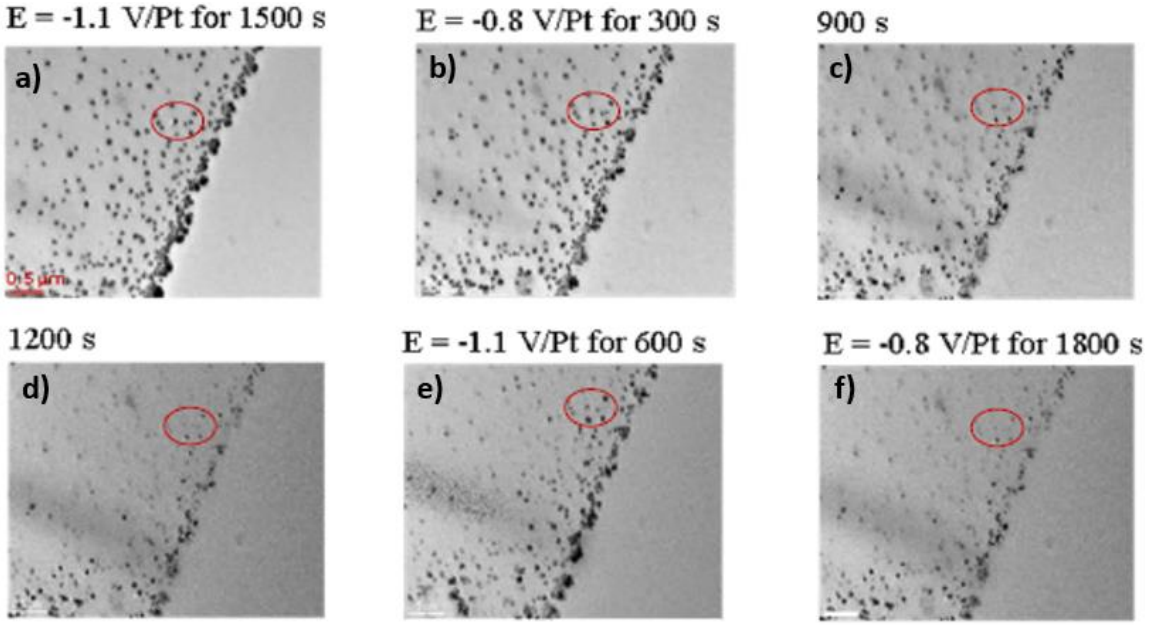

Figure 4.22: Series of TEM images showing two cycles of reversible deposition (E= -1.1 V) and dissolution (E= -0.8 V) of Fe particles in the same area of the glassy carbon working electrode.

However, as seen from the series of TEM images observed in the first cycle, the figures do appear "clear", which indicates the presence of a bubble (bubbles, most probably hydrogen gas, are formed due to the radiolysis). This means that only a thin film of liquid is wetting the electrodes as it is impossible to have an electrochemical reaction without the contact of liquid with electrodes. In the second cycle, the images appear dull. This is because the absence of the hydrogen bubble and the presence of the liquid throughout the whole experiment. In the second cycle, the NPs were deposited predominantly on the edge of the electrodes, as seen in Figure 4.23.

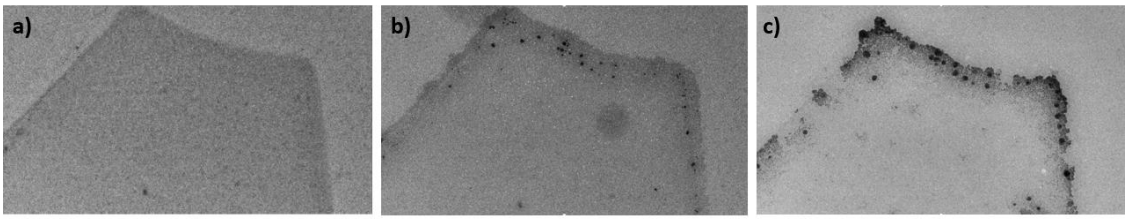

Figure 4.23: Precipitation of Fe NPs occurs predominantly on the edge of the electrode.

After the in situ experiments, the chips were air-dried and inserted into the specialized modified holder (for more information look se Section 3.2.1.3) and reinserted into the TEM. Radial integration of the electron diffraction patterns (Figure 4.24) revealed the presence of crystalline γ-Fe (FCC), which was confirmed by fitting the experimental SAED pattern.

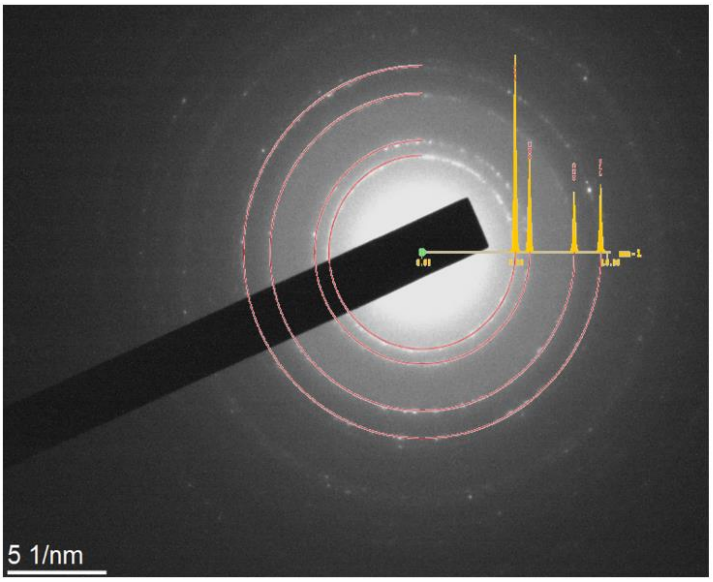

Experimental SAED (nm^{-1})	γ-Fe 44862 (FCC) (nm^{-1})
4.66	4.75
5.37	5.48
7.62	7.75
8.96	9.09
11.8	11.95
14.06	14.0
16.2	16.05

Figure 4.24: Experimental and fitted/integrated SAED pattern revealing the existence of crystalline γ-Fe.

The Fe NPs synthesis can be easily explained with the Pourbaix diagram (see Section 1.6.4, Figure 1.10): once we decrease the potential from -0.8 V to -1.2 V at pH=2.8, the precipitation of metallic Fe is expected as the Fe NPs are thermodynamically (electrochemically) stabilized. However, the observed formation of γ-Fe (FCC) was not expected as the α-Fe (BCC) allotrope is known to be a thermodynamically stable crystalline form [169]. This can be partially explained by fact that the Fe FCC structure is energetically stabilized in the nanometer size range, i.e., in the form of NPs [170]. Other factors that can provoke the formation of FCC Fe are the presence of impurities, the influence of the radiolysis and the formation of H_2 bubbles at the WE.

4.4 Radiolysis-Induced Artifacts Inside LCTEM

During the LCTEM experiments several artifacts were observed that if not readily recognized could be interpreted as real results. The most important is the radiolytically induced growth of the Au NPs. It was shown that Au NPs can, in some cases, grow even in the solutions which, before the insertion in the liquid cell, did not contain any (even minor) concentration of the Au ions. Artifacts were observed in the systems of YAc and urea and $TiCl_4$.

4.4.1 Radiolytically Induced Growth of Gold Nanoparticles

In the case of the Yac-urea experiments, when the temperature was raised above 90 °C at a dose rate of 5000 $e^-/nm^2/s$, the abrupt nucleation of faceted Au NPs was observed (Figure 4.25). In the second case (Figure 4.26) with the same initial conditions applied, resulting in the precipitation of Au dendrites. While the hexagonal faceted NPs did not experience significant morphological changes during the observation, this was not true for the dendritic nanostructure. The dendrites first experience rapid growth by developing a highly branched, hierarchical structure up to their final size of 50 nm in the first 45 s of the observation. In the second stage, in a period of about 45 s, the dendrites undergo rapid fragmentation, resulting in the formation of several spherically shaped particles within the

original dendrite volume that were dynamically changing, either by coalescence or Ostwald ripening. Finally, the spherical particles experience a complete dissolution within the observed area, accompanied by the appearance of faceted, 150-nm-sized NPs in the vicinity of the observation area. SAED patterns showed that these NPs were not crystalline yttria, as expected, but indeed artifacts - gold NPs.

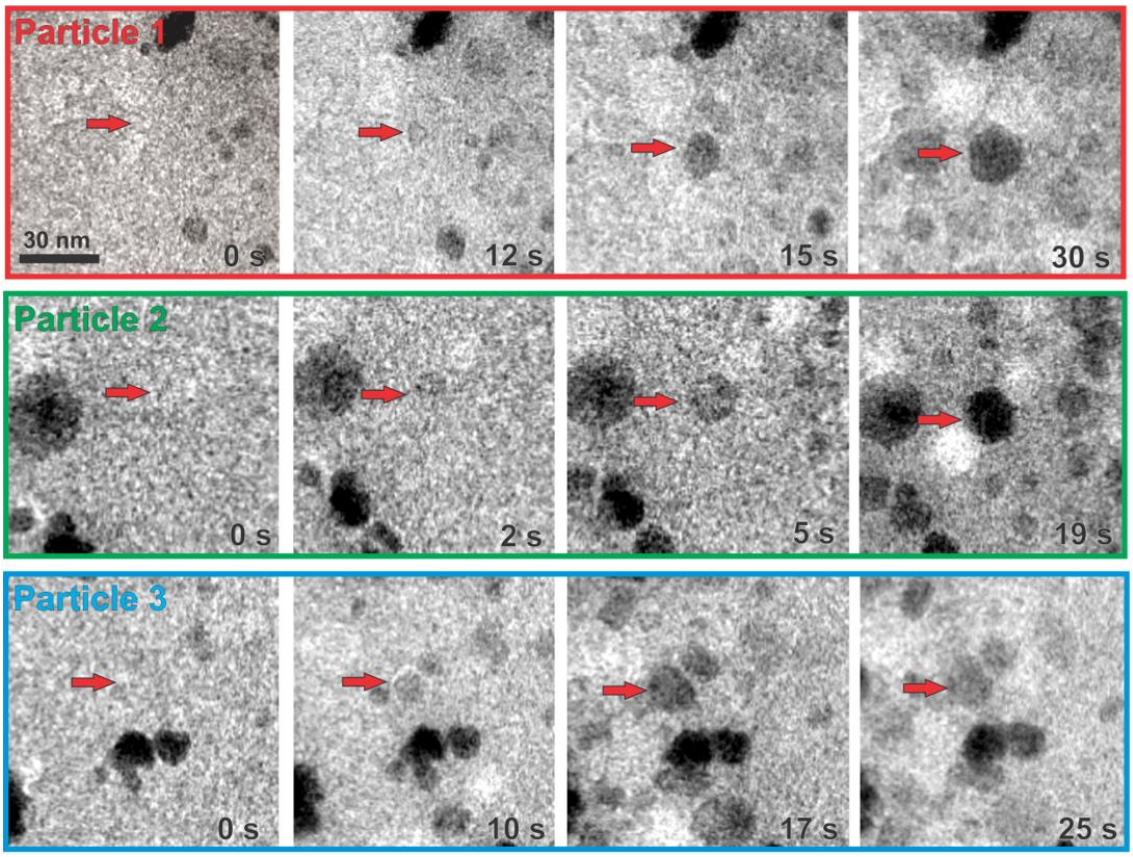

Figure 4.25: Formation of artifacts – hexagonal shaped Au NPs from the solution which initially did not contain any dissolved Au ions.

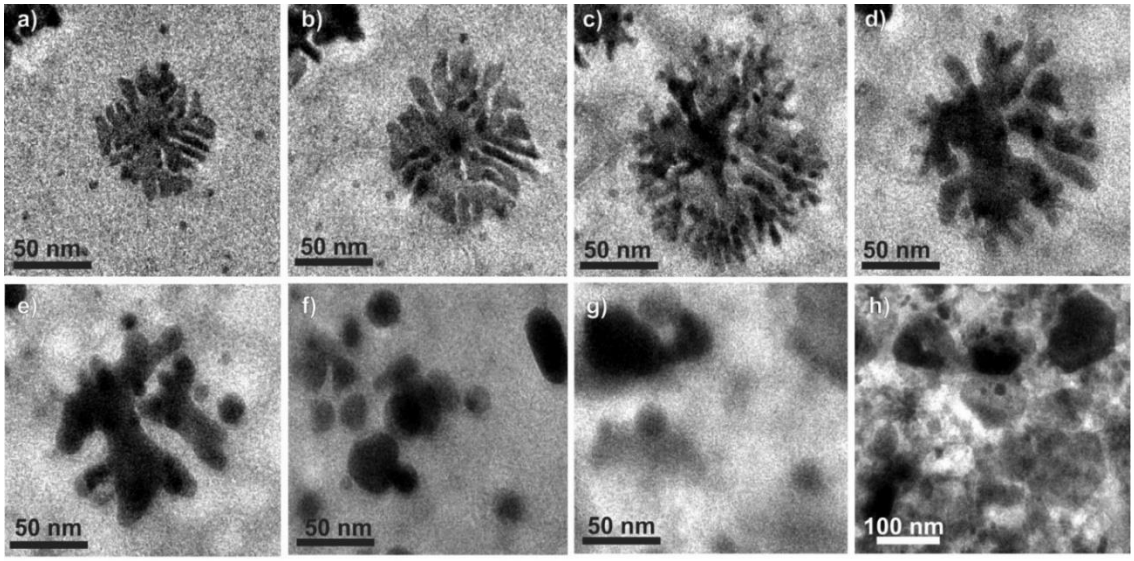

Figure 4.26: Growth sequence of Au NP artifacts: initial growth of dendrites (a–c), which is followed by the defragmentation of dendrites to small spherical NPs (d–f), either with a process of coalescence or Ostwald ripening. In the final stage spherical NPs are fully dissolved (g) and in their vicinity faceted NPs appear (h).

Artifacts also appeared during the LCTEM synthesis of TiO_2 with synthesis procedure of Park et al. [171]. All the chemicals were of high purity: none of them contained any measurable amounts of Au. The solution was inserted in to the in situ heating holder. Small chips with a 150-nm static spacer were used.

The solution was observed in the TEM at a dose rate of ca. 10^8 Gy/s and 100 °C. When the dose rate was increased to 10^{10} Gy/s, Au NPs started to precipitate and grow. In some cases, rotations of the Au prisms were observed (Figure 4.27). Possibly due to the nanobubble formation, forcing the crystal to turn.

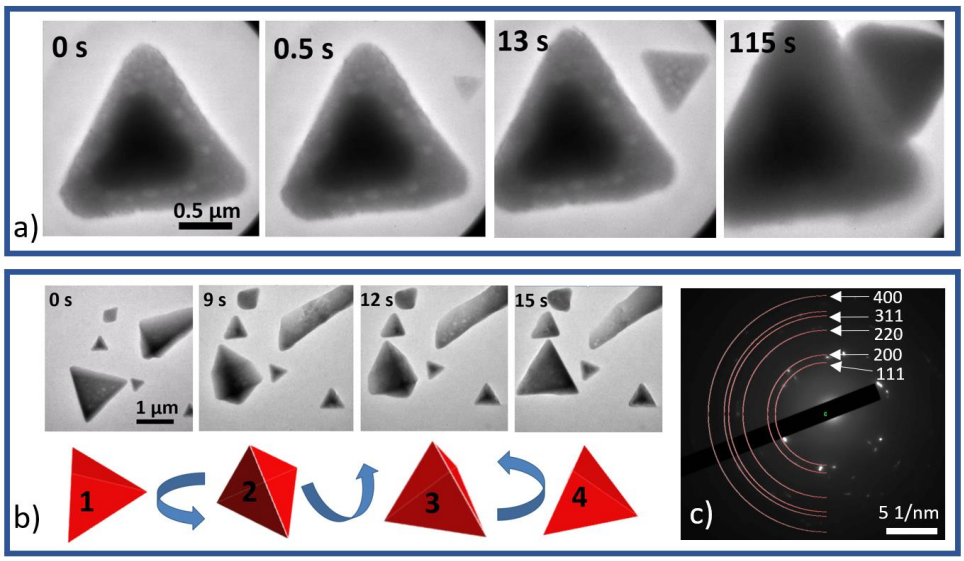

Figure 4.27: a) Growth of Au NPs and b) rotation of NPs. Both at a temperature of 100 °C and a dose rate of 10^{10} Gy/s, c) corresponding SAED pattern showing Au crystal structure.

Precipitation of Au NPs from both solutions not containing any Au ions could be explained by the following path. As a result of the radiolysis, radicals form and diffuse from the region of the electron beam to the gold spacer. Since radicals are strong reducing agents, they react with gold and dissolve it. By this mechanism, the gold enters the solution and it is subsequently deposited in the region of the electron beam. High dose rates inhibit faster radiolysis-induced Au precipitation and in higher quantities. Since the formation of Au happens almost instantly, this shows the speed of diffusion of the radicals inside the liquid cell. Radiolytically grown Au NPs were further proved when the liquid cell was observed at the low-magnification setting – where it was observed that NPs grew only within the area illuminated by the electron beam (Figure 4.28).

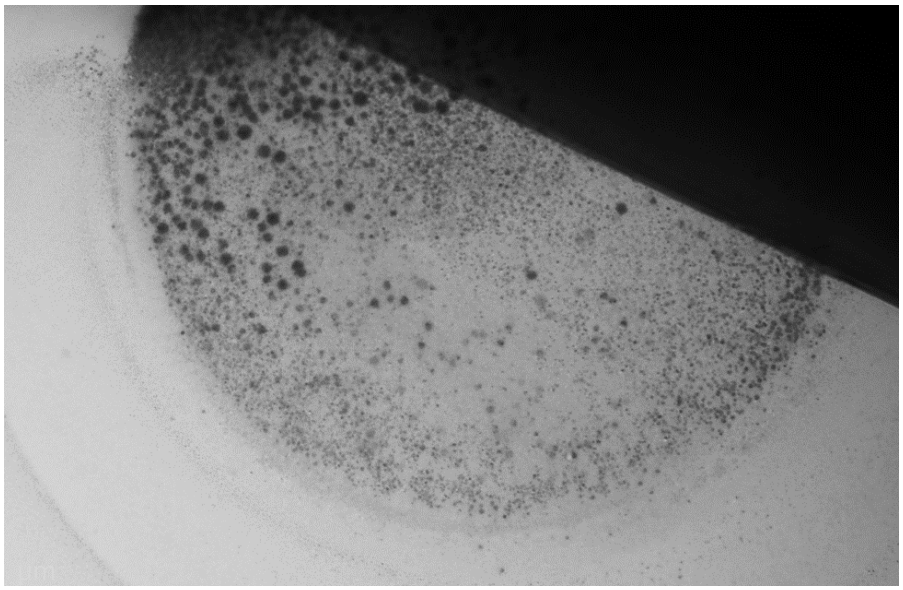

Figure 4.28: NPs appeared only in the circular area that was illuminated by the electron beam. The black part is the edge of the Si chip, which is not transparent due to its thickness.

4.4.2 Bubble Formation

One of the most readily observed radiolysis artifacts in the LCTEM is the formation of bubbles. The size of the bubbles in the water was directly related to the dose rate. When the dose rate was increased, the bubble starts nucleating and inflating. When the dose rate was decreased, the bubble deflated and completely annihilated (Figure 4.29).

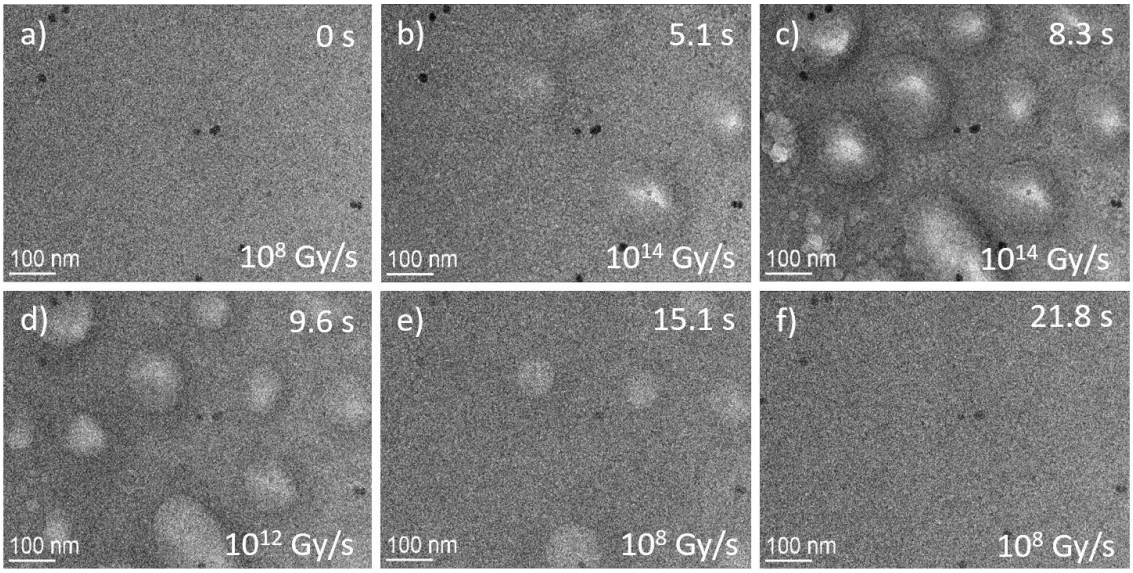

Figure 4.29: Formation of bubbles in relation to the dose rate: a) at the dose rate of 10^8 Gy/s the deionized water is stable and no bubble could be observed. When the dose rate was increased to 10^{14} Gy/s, nucleation of the bubbles could be observed (b-c). When the dose rate was decreased the bubbles started to deflate (d-e) and completely annihilated back into the water (f).

If the dose rate was increased for a prolonged time, the bubble becomes so large, that it forced the liquid out partially or completely out of the viewing area (Figure 4.30). One advantage of bubble formation is the formation of the meniscus - a thin nanometer-thick layer of liquid which is enough that some of the experiments could be performed and the same time the microscope resolution and brightness was improved because the liquid layer is so thin.

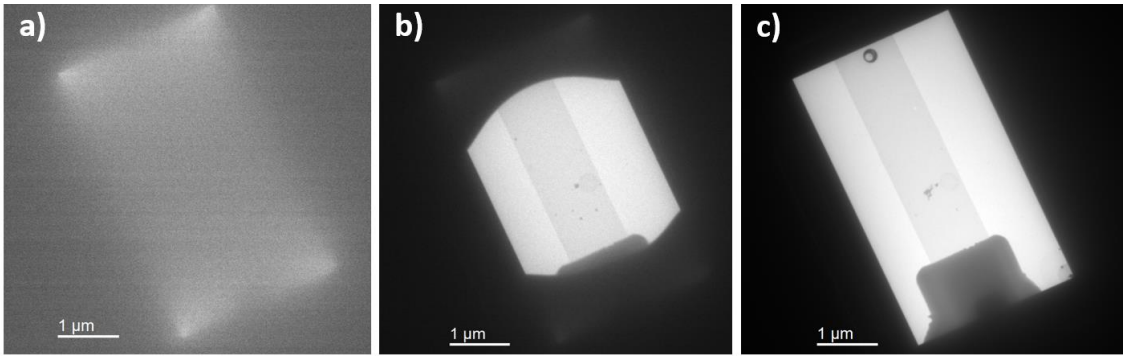

Figure 4.30: Sequence of images showing the formation of the hydrogen gas bubble and subsequent escape of the liquid: a) liquid cell filled with liquid – the images appear blurry due to electron scattering in water, b) liquid cell with meniscus of hydrogen bubble, c) bubble is larger than window area. Note the substantial increase in resolution/brightness when the liquid is forced out of the liquid cell.

Intentionally left blank

Chapter 5

Conclusions

The main goal of this PhD study, i.e., to develop and verify the experimental procedures that enable controlled LCTEM experiments for the in situ dynamic investigation of the nucleation and growth phenomena of NPs in aqueous environments at high spatial and temporal resolution, was achieved. For that purpose, a liquid cell with heating capabilities was successfully implemented for studying Au NPs' and Y hydroxide NPs' nucleation and early growth, while the electrochemical cell inside the TEM was used for studying the early processes of the electrochemical deposition of Fe NPs. The influence of radiolysis on the kinetics of a NP´s formation in the LCTEM during specimen observation was thoroughly modelled and quantified.

The proposed paradigm of modeling the complex redox chemistry inside the LCTEM represents an important contribution to real-time nanoscale visualization and manipulation of the nanostructured systems in a liquid environment. The TDR diagrams (Figure 5.1) obtained from the improved kinetic radiolysis model provide us with a better simulation of the precipitation, growth, and dissolution of Au NPs under a variety of LCTEM conditions. In the LCTEM system, the Au redox potential is investigated as a parameter of the electron-dose rate, temperature, and pressure. Our new model was verified using experimental data in the literature obtained from low-dose experiments using γ radiation. The validity of the radiolysis model was then confirmed by LCTEM experiments that were consistent with the TDR diagrams. It was confirmed that the Au NPs precipitate firstly as a result of an increased dose rate and, secondly, due to the combined effect of the increased temperature, pressure and saturation concentration of H_2 and O_2, which in both cases shift the equilibrium $[Au^0]/[Au^+]$ concentrations in favor of zero-valence gold (Au^0). Both proposed mechanisms were found to be completely reversible, which suggests that the Au precipitation/dissolution reactions can be fine-tuned by altering the parameters inside the LCTEM.

As such, the presented comprehensive radiolysis model can be, in principle, extended to other materials systems and solvents by including proper system-related radical-induced redox chemistry. The proposed paradigm of modeling the complex redox chemistry inside the LCTEM represents an important contribution to real-time nanoscale visualization and manipulation of the nanostructured systems in liquid environments, as it represents the first of a kind and unique knowledge that can be implemented in many different branches of nanotechnology and energy-related processes.

It was shown that temperature is an important thermodynamic parameter that strongly influences the kinetics of chemical reactions inside the liquid cell. It was recognized that it is crucial that radiolysis in relation to the underlying chemical reactions is well understood, also as a function of elevated temperatures. This study provided a comprehensive radiolysis model for the interpretation of the LCTEM experiments for the temperature range between 20 °C and 100 °C for Au NPs growth and dissolution phenomena in aqueous solutions. The new radiolysis model acknowledges the following parameters: dose rate, temperature, pressure, pH, the formation of gaseous phases, the initial concentration of the gases (for the aerated solutions), rate constants, and the presence of Au ion and Au^0. In particular,

Schneider´s model [43] was modified and upgraded in two aspects: (i) addition of the temperature as a parameter and (ii) a new interpretation of the oxidizing/reductive ability of radiolysis products.

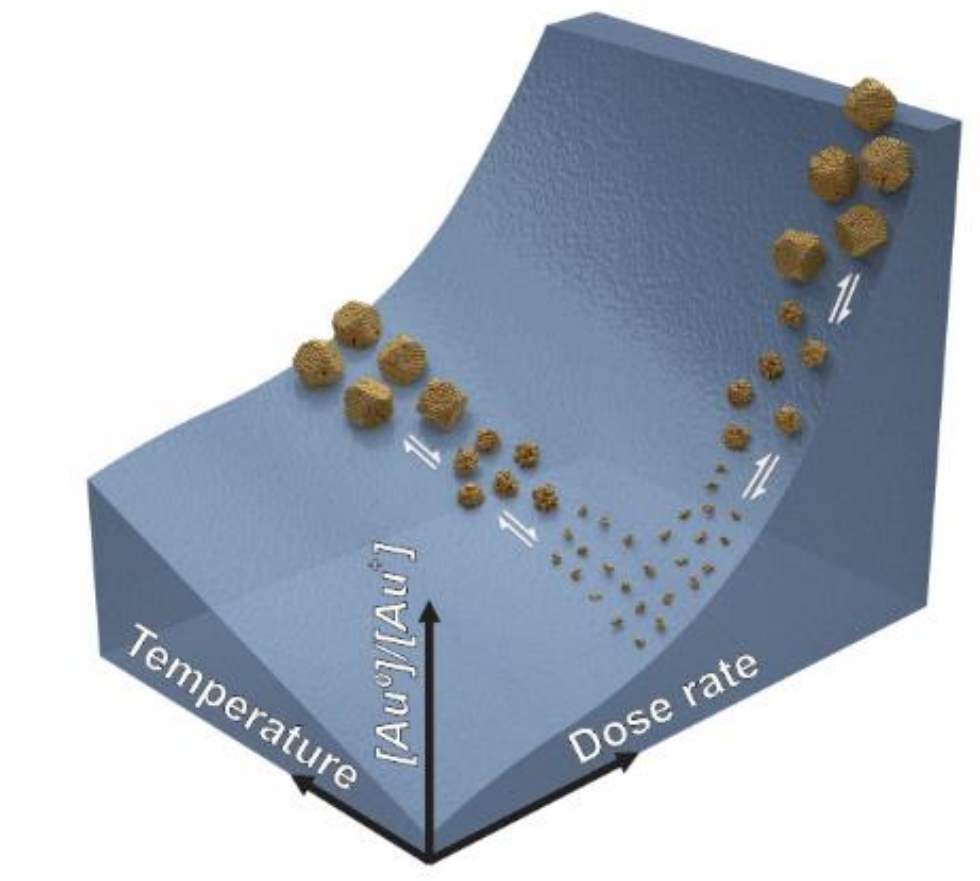

Figure 5.1: Graphical illustration of the Au precipitation/dissolution controlled by the radical-induced redox chemistry inside the LCTEM. The growth and dissolution of Au particles are reversible and can be controlled by different operating conditions in the liquid cell.

We have demonstrated that radiolysis chemistry produces reducing species that dissolved Au spacers in the chips. As a result, gold ions enter into the solution and are deposited directly in the area of the electron beam, causing the formation of Au NPs artifacts.

Y-based precursors as a model phosphorus material were synthesized conventionally in a glass beaker and in situ in TEM using the LCTEM technique. Both techniques yielded precipitation of amorphous yttrium NPs. After the process of annealing in a furnace for 2 h at 700 °C, NPs were in both cases transformed into crystalline yttrium hydroxide. This is believed to be one the first report of the synthesis of hydroxide powders using the LCTEM technique.

We have successfully shown the in situ Fe deposition-dissolution process in a LCTEM and affirmed that the Fe NPs grow through electrochemical deposition rather than by the electron beam. The nucleation, morphology, and composition of the deposited Fe particles are discussed.

5.1 Procedures for Mitigating Radiolysis Artifacts

As shown, radiolysis-driven artifacts are an undesirable consequence of the LCTEM technique. The proposed solutions to mitigate the effects of electron radiolysis are:

1) The use of radiolysis models as demonstrated, making it possible to show the threshold at which the observed processes are radiolytically induced and those which are not.
2) Observing the liquid with a "single exposure technique" - only during the imaging, as demonstrated in the case of LCTEM synthesis of Fe-NPs (Section 4.3.3).
3) The use of STEM can greatly reduce dose rates, because at any one single time only one small area is electron irradiated [65].
4) Use of liquids that are less prone to radiolysis [172].
5) Use of liquids that are not highly volatile or corrosive since they can evaporate before the liquid cell is sealed.
6) Use of highly diluted solutions/solutions with a low concentration of dissolved ions (e.g., in the mM range), since dissolved ions in a diluted solution, react less with the radiolysis species.
7) Whenever possible, direct flow experiments with high flow rates are suggested, to flush the radiolysis species out of the observation area of the liquid cell.
8) Preparations of liquid samples just before the insertion into the liquid cell to prevent the formation artifacts formed from aging of the solution.
9) Observation of samples at reduced dose rates (decreasing spot size, use of small condenser apertures).
10) Observing samples for shorter times.
11) Careful planning of the LCTEM experiments: with the "lowest necessary exposure to ionizing radiation" principle. This means that the sample should be observed only at such a low electron dose and for a such short time, that the image/video/data with only the predetermined required resolution is obtained and not higher than is needed.
12) TEM alignment needs to be performed before the insertion of the LCTEM holder or use of auto-alignment procedures [173], since during TEM alignment high electron doses are expected.
13) Use of ultra-thin graphene liquid cells (instead of SiN) that allows smaller electron dose rates for the same brightness/contrast of the image.
14) Use of liquid cells where the ratio between the windows and the entire volume of the liquid cells is very large, so that diffusion of the radiolysis species is prolonged.
15) Thorough cleaning after each use of all the components of the liquid cell (chips, holder, lids, necessary tools, internal and external tubing) with alcohol, deionized water, and plasma so that contaminants from previous experiments are completely removed, preventing that remaining particles from acting as nuclei for a heterogeneous nucleation process. Frequent replacements of expendable parts (e.g., internal tubing) are suggested.
16) Avoiding the reuse of chips that have already been used in previous experiments.
17) Use of a dust-free clean-room environment for preparing samples and the assembly of the liquid cell to prevent contaminants entering to the solution. Also, the sample-preparation room should have temperature/humidity control.

For the LCTEM experiments, especially the synthesis of NPs, many variables were addressed so that repeatable results were obtained.

To achieve reliable results, the procedure for the assembly of the liquid cell was established (Section 3.2.1.3). Most of the liquid cell (with the expectation of the microscopically small SiN windows) is non-transparent. To observe the effects of mixing of the two different liquids, the lid of the liquid cell was replaced with a sheet of glass. It was found that the mixing of the liquid does not occur inside the mixing chamber (Section 4.1.2). Diffusional mixing occurs in the internal tubing, outside of the viewing area, which severely limits the interpretation of the mixing experiments.

As the dose rate is an important parameter in LCTEM experiments. The procedure for measuring of the dose rate was established (Section 3.4).

5.2 New Research Strategies for Radiolysis-Driven Experiments

Rather than preventing radiolysis effects, a new paradigm [51] is proposed where the LCTEM has the potential to become a powerful tool for studies of the radiolysis effects in various fields of science and industry.

For example, as of December 2019, 455 fission nuclear reactors were operational in the world [174]. However, nowhere in the world has permanent storage for highly radioactive spent nuclear fuel been built [175]. Large resources have been invested in the past few decades for the permanent storage or geological disposal of spent nuclear fuel in corrosion-resistant containers underground in Canada, Finland, Germany, Spain, Sweden, and the United States. Underground containers are expected, during the millennia of storage, to come into contact with groundwater. Since the spent fuel is highly radioactive, it will cause β and γ radiolysis of water, which influences the corrosion rate [176], [177]. Radiolysis was also observed in primary coolant water in pressurized-water reactors and it was shown in some experiments that an increase of the concentration of ^{10}B (boric acid is injected in the reactor before shutting down of the reactor for regular maintenance) increases the water radiolysis rate [178]. LCTEM is potentially a very useful, safe and quick tool for such experiments, since the person operating the TEM is not exposed [16] to any harmful levels of ionizing radiation and therefore does not need specialized nuclear training and personal protective radiological equipment that is commonly used in the nuclear industry [179].

Besides the nuclear industry radiolysis effects are also an important topic in studies of the effect of ionizing radiation (in the form of natural UV) on human skin cells, especially melanin pigment [180]. Radiolysis is also an important effect in the studies of the evolution of the solar system since that effect occurs in water ice on outer solar-system bodies, e.g., Jovian moon Europa [181]. Understanding radiolysis is important for the interpretation of remote sensing data from space probes [182].

References

[1] W. J. Stark, P. R. Stoessel, W. Wohlleben, and A. Hafner, "Industrial applications of nanoparticles," *Chem. Soc. Rev.*, vol. 44, no. 16, pp. 5793–5805, 2015, doi: 10.1039/c4cs00362d.

[2] C. S. C. Santos *et al.*, "Industrial Applications of Nanoparticles - A Prospective Overview," *Mater. Today Proc.*, vol. 2, no. 1, pp. 456–465, 2015, doi: 10.1016/j.matpr.2015.04.056.

[3] D. Chen, X. Qiao, X. Qiu, and J. Chen, "Synthesis and electrical properties of uniform silver nanoparticles for electronic applications," *J. Mater. Sci.*, vol. 44, no. 4, pp. 1076–1081, 2009, doi: 10.1007/s10853-008-3204-y.

[4] R. A. Taylor *et al.*, "Feasibility of nanofluid-based optical filters," *Appl. Opt.*, vol. 52, no. 7, p. 1413, 2013, doi: 10.1364/AO.52.001413.

[5] Q. Q. Zhao, A. Boxman, and U. Chowdhry, "Nanotechnology in the chemical industry–opportunities and challenges," *J. Nanoparticle Res.*, vol. 5, no. 5–6, pp. 567–572, 2003, doi: 10.1023/B:NANO.0000006151.03088.cb.

[6] R. M. Rioux, H. Song, J. D. Hoefelmeyer, P. Yang, and G. A. Somorjai, "High-surface-area catalyst design: Synthesis, characterization, and reaction studies of platinum nanoparticles in mesoporous SBA-15 silica," *J. Phys. Chem. B*, vol. 109, no. 6, pp. 2192–2202, 2005, doi: 10.1021/jp048867x.

[7] A. H. Lu, E. L. Salabas, and F. Schüth, "Magnetic nanoparticles: Synthesis, protection, functionalization, and application," *Angew. Chemie - Int. Ed.*, vol. 46, no. 8, pp. 1222–1244, 2007, doi: 10.1002/anie.200602866.

[8] J. Qin *et al.*, "Gold nanorods as a theranostic platform for in vitro and in vivo imaging and photothermal therapy of inflammatory macrophages," *Nanoscale*, vol. 7, no. 33, pp. 13991–14001, 2015, doi: 10.1039/c5nr02521d.

[9] N. Silva *et al.*, "In Situ Visualization of the Local Photothermal Effect Produced on α-Cyclodextrin Inclusion Compound Associated with Gold Nanoparticles.," *Nanoscale Res. Lett.*, vol. 11, no. 1, p. 180, Dec. 2016, doi: 10.1186/s11671-016-1322-z.

[10] X. Ji, X. Song, J. Li, Y. Bai, W. Yang, and X. Peng, "Size control of gold nanocrystals in citrate reduction: The third role of citrate," *J. Am. Chem. Soc.*, vol. 129, no. 45, pp. 13939–13948, 2007, doi: 10.1021/ja074447k.

[11] M. Wuithschick *et al.*, "Turkevich in New Robes: Key Questions Answered for the Most Common Gold Nanoparticle Synthesis," *ACS Nano*, vol. 9, no. 7, pp. 7052–7071, 2015, doi: 10.1021/acsnano.5b01579.

[12] F. M. Ross, "Opportunities and challenges in liquid cell electron microscopy," *Science (80-.).*, vol. 350, no. 6267, pp. aaa9886–aaa9886, Dec. 2015, doi: 10.1126/science.aaa9886.

[13] N. de Jonge and F. M. Ross, "Electron microscopy of specimens in liquid," *Nature Nanotech.*, vol. 6, no. 1, pp. 695–704, 2011, doi: 10.1016/j.bpj.2012.05.042.

[14] D. B. Peckys and N. de Jonge, "Liquid STEM for Studying Biological Function in Whole Cells," *Liq. Cell Electron Microsc.*, pp. 334–355, 2016, doi: 10.1017/9781316337455.017.

[15] S. W. Chee and M. G. Burke, "Applications of Liquid Cell TEM in Corrosion Science," *Liq. Cell Electron Microsc.*, pp. 258–275, 2016, doi: 10.1017/9781316337455.013.

[16] C. B. Williams, David B., Carter, *Transmission Electron Microscopy: A Textbook for Materials Science*. New York: Springer, 2009.

[17] Y. Jiang *et al.*, "Electron ptychography of 2D materials to deep sub-ångström resolution," *Nature*, vol. 559, no. 7714, pp. 343–349, 2018, doi: 10.1038/s41586-018-0298-5.

[18] H. NYQUIST, "Certain Topics in Telegraph Transmission Theory," *Trans. Am. Inst. Electr. Eng.*, vol. 47, no. 2, pp. 617–644, 1928, doi: 10.1109/T-AIEE.1928.5055024.

[19] T. Ngo and H. Yang, "Toward Ending the Guessing Game: Study of the Formation of Nanostructures Using in Situ Liquid Transmission Electron Microscopy," *J. Phys. Chem. Lett.*, vol. 6, no. 24, pp. 5051–5061, 2015, doi: 10.1021/acs.jpclett.5b02210.

[20] N. Hodnik, G. Dehm, and K. J. J. Mayrhofer, "Importance and Challenges of Electrochemical in Situ Liquid Cell Electron Microscopy for Energy Conversion Research," *Acc. Chem. Res.*, vol. 49, no. 9, pp. 2015–2022, 2016, doi: 10.1021/acs.accounts.6b00330.

[21] H. Liao and H. Zheng, "Liquid Cell Transmission Electron Microscopy Study of Platinum Iron," *J. Am. Chem. Soc.*, vol. 135, pp. 5038–5043, 2013, doi: 10.1021/ja310612p.

[22] L. R. Parent *et al.*, "Directly Observing Micelle Fusion and Growth in Solution by Liquid-Cell Transmission Electron Microscopy," *J. Am. Chem. Soc.*, vol. 139, no. 47, pp. 17140–17151, 2017, doi: 10.1021/jacs.7b09060.

[23] T. H. Moser, H. Mehta, C. Park, R. T. Kelly, T. Shokuhfar, and J. E. Evans, "The role of electron irradiation history in liquid cell transmission electron microscopy," *Sci. Adv.*, vol. 4, no. 4, 2018, doi: 10.1126/sciadv.aaq1202.

[24] J. Hermannsdoerfer and N. de Jonge, "Studying Dynamic Processes of Nano-sized Objects in Liquid using Scanning Transmission Electron Microscopy," *Jove-Journal Vis. Exp.*, no. 120, pp. 1–11, 2017, doi: 10.3791/54943.

[25] J. M. Yuk *et al.*, "High-resolution EM of colloidal nanocrystal growth using graphene liquid cells," *Science (80-.).*, vol. 335, no. 6077, pp. 61–64, 2012, doi: 10.1126/science.1217654.

[26] Y. Kimura, H. Niinomi, K. Tsukamoto, and J. M. García-Ruiz, "In situ live observation of nucleation and dissolution of sodium chlorate nanoparticles by transmission electron microscopy," *J. Am. Chem. Soc.*, vol. 136, no. 5, pp. 1762–1765, 2014, doi: 10.1021/ja412111f.

[27] D. Shin *et al.*, "Growth dynamics and gas transport mechanism of nanobubbles in graphene liquid cells," *Nat. Commun.*, vol. 6, pp. 1–6, 2015, doi: 10.1038/ncomms7068.

[28] N. D. Loh *et al.*, "Multistep nucleation of nanocrystals in aqueous solution," *Nat. Chem.*, vol. 9, no. 1, pp. 77–82, 2017, doi: 10.1038/nchem.2618.

[29] M. R. Hauwiller *et al.*, "Dynamics of Nanoscale Dendrite Formation in Solution Growth Revealed Through in Situ Liquid Cell Electron Microscopy," *Nano Lett.*, vol. 18, p. acs.nanolett.8b02819, 2018, doi: 10.1021/acs.nanolett.8b02819.

[30] X. Chen and J. Wen, "In situ wet-cell TEM observation of gold nanoparticle motion in an aqueous solution.," *Nanoscale Res. Lett.*, vol. 7, no. 1, p. 598, Oct. 2012, doi: 10.1186/1556-276X-7-598.

[31] S. W. Chee, S. H. Pratt, K. Hattar, D. Duquette, F. M. Ross, and R. Hull, "Studying localized corrosion using liquid cell transmission electron microscopy," *Chem. Commun.*, vol. 51, no. 1, pp. 168–171, 2015, doi: 10.1039/c4cc06443g.

[32] T. Kraus and N. De Jonge, "Dendritic gold nanowire growth observed in liquid with transmission electron microscopy," *Langmuir*, vol. 29, no. 26, pp. 8427–8432, 2013, doi: 10.1021/la401584z.

[33] J. H. Park *et al.*, "Control of Electron Beam-Induced Au Nanocrystal Growth Kinetics through Solution Chemistry," *Nano Lett.*, vol. 15, no. 8, pp. 5314–5320, 2015, doi: 10.1021/acs.nanolett.5b01677.

[34] N. de Jonge, D. B. Peckys, G. J. Kremers, and D. W. Piston, "Electron microscopy of whole cells in liquid with nanometer resolution," *Proc. Natl. Acad. Sci. U. S. A.*, vol. 106, no. 7, pp. 2159–2164, 2009, doi: 10.1073/pnas.0809567106.

[35] P. J. M. Smeets, K. R. Cho, R. G. E. Kempen, N. a J. M. Sommerdijk, and J. J. De Yoreo, "Calcium carbonate nucleation driven by ion binding in a biomimetic matrix revealed by in situ electron microscopy.," *Nat. Mater.*, vol. 4193, no. January, pp. 1–6, 2015, doi: 10.1038/nmat4193.

[36] T.-Y. Ahn, S.-P. Hong, S.-I. Kim, and Y.-W. Kim, "In situ liquid-cell transmission electron microscopy for direct observation of concentration-dependent growth and dissolution of silver nanoparticles," *RSC Adv.*, vol. 5, no. 100, pp. 82342–82345, 2015, doi: 10.1039/C5RA14879K.

[37] A. V. Ievlev, S. Jesse, T. J. Cochell, R. R. Unocic, V. A. Protopopescu, and S. V. Kalinin, "Quantitative Description of Crystal Nucleation and Growth from in Situ Liquid Scanning Transmission Electron Microscopy," *ACS Nano*, vol. 9, no. 12, pp. 11784–11791, 2015, doi: 10.1021/acsnano.5b03720.

[38] M. J. Dukes, B. W. Jacobs, D. G. Morgan, H. Hegde, and D. F. Kelly, "Visualizing nanoparticle mobility in liquid at atomic resolution," *Chem. Commun.*, vol. 49, no. 29, pp. 3007–3009, 2013, doi: 10.1039/C3CC41136B.

[39] J. H. Park, D. A. Steingart, S. Kodambaka, and F. M. Ross, "Electrochemical electron beam lithography : Write , read , and erase metallic nanocrystals on demand," *Sci. Adv.*, no. July, pp. 1–8, 2017.

[40] G. Zhu *et al.*, "In situ study of the growth of two-dimensional palladium dendritic nanostructures using liquid-cell electron microscopy," *Chem. Commun.*, vol. 50, no. 67, p. 9447, 2014, doi: 10.1039/C4CC03500C.

[41] M. H. Nielsen, S. Aloni, and J. J. De Yoreo, "In situ TEM imaging of CaCO<inf>3</inf> nucleation reveals coexistence of direct and indirect pathways," *Science (80-.).*, vol. 345, no. 6201, pp. 1158–1162, 2014, doi: 10.1126/science.1254051.

[42] M. S. A. Asghar, B. J. Inkson, and G. Möbus, "Giant Radiolytic Dissolution Rates of Aqueous Ceria Observed in Situ by Liquid-Cell TEM," *ChemPhysChem*, vol. 18, no. 10, pp. 1247–1251, 2017, doi: 10.1002/cphc.201601398.

[43] N. M. Schneider, M. M. Norton, B. J. Mendel, J. M. Grogan, F. M. Ross, and H. H. Bau, "Electron-Water interactions and implications for liquid cell electron microscopy," *J. Phys. Chem. C*, vol. 118, no. 38, pp. 22373–22382, 2014, doi: 10.1021/jp507400n.

[44] D. Alloyeau *et al.*, "Unravelling Kinetic and Thermodynamic Effects on the Growth of Gold Nanoplates by Liquid Transmission Electron Microscopy," *Nano Lett.*, vol. 15, no. 4, pp. 2574–2581, 2015, doi: 10.1021/acs.nanolett.5b00140.

[45] Y. C. Chen, J. Y. Chen, and W. W. Wu, "In Situ Observation of Au Nanostructure Evolution in Liquid Cell TEM," *J. Phys. Chem. C*, vol. 121, no. 46, pp. 26069–26075, 2017, doi: 10.1021/acs.jpcc.7b07956.

[46] Y. Liu, X. M. Lin, Y. Sun, and T. Rajh, "In situ visualization of self-assembly of charged gold nanoparticles," *J. Am. Chem. Soc.*, vol. 135, no. 10, pp. 3764–3767, 2013, doi: 10.1021/ja312620e.

[47] R. F. Egerton, P. Li, and M. Malac, "Radiation damage in the TEM and SEM," *Micron*, vol. 35, no. 6, pp. 399–409, 2004, doi: 10.1016/j.micron.2004.02.003.

[48] J. E. Evans, K. L. Jungjohann, N. D. Browning, and I. Arslan, "Controlled growth of nanoparticles from solution with in situ liquid transmission electron microscopy," *Nano Lett.*, vol. 11, no. 7, pp. 2809–2813, 2011, doi: 10.1021/nl201166k.

[49] T. J. Woehl, K. L. Jungjohann, J. E. Evans, I. Arslan, W. D. Ristenpart, and N. D. Browning, "Experimental procedures to mitigate electron beam induced artifacts during in situ fluid imaging of nanomaterials," *Ultramicroscopy*, vol. 127, pp. 53–63, 2013, doi: 10.1016/j.ultramic.2012.07.018.

[50] A. Mozumder, *Fundamentals of Radiation Chemistry*. San Diego, California: Academic Press, 1999.

[51] S. M. Rehn and M. R. Jones, "New Strategies for Probing Energy Systems with In Situ Liquid-Phase Transmission Electron Microscopy," 2018, doi: 10.1021/acsenergylett.8b00527.

[52] M. A. Hill and F. A. Smith, "Calculation of initial and primary yields in the radiolysis of water," *Radiat. Phys. Chem.*, vol. 43, no. 3, pp. 265–280, Mar. 1994, doi: 10.1016/0969-806X(94)90190-2.

[53] S. Le Caër, "Water Radiolysis: Influence of Oxide Surfaces on H2 Production under Ionizing Radiation," *Water*, vol. 3, no. 4, pp. 235–253, 2011, doi: 10.3390/w3010235.

[54] A. Cameron Varano, A. Rahimi, M. J. Dukes, S. Poelzing, S. M. McDonald, and D. F. Kelly, "Visualizing virus particle mobility in liquid at the nanoscale," *Chem. Commun.*, vol. 51, no. 90, pp. 16176–16179, 2015, doi: 10.1039/C5CC05744B.

[55] T. J. J. Woehl and P. Abellan, "Defining the radiation chemistry during liquid cell electron microscopy to enable visualization of nanomaterial growth and degradation dynamics," *J. Microsc.*, vol. 265, no. 2, pp. 135–147, 2017, doi: 10.1111/jmi.12508.

[56] J. M. Grogan, N. M. Schneider, F. M. Ross, and H. H. Bau, "Bubble and pattern formation in liquid induced by an electron beam," *Nano Lett*, vol. 14, pp. 0–5, 2014, doi: 10.1021/nl404169a.

[57] T. J. WOEHL and P. ABELLAN, "Defining the radiation chemistry during liquid cell electron microscopy to enable visualization of nanomaterial growth and degradation dynamics," *J. Microsc.*, no. December 2016, p. n/a-n/a, 2016, doi: 10.1111/jmi.12508.

[58] J. M. Grogan, N. M. N. M. Schneider, F. M. Ross, and H. H. Bau, "Bubble and pattern formation in liquid induced by an electron beam," *Nano Lett*, vol. 14, no. 1, pp. 0–5, 2014, doi: 10.1021/nl404169a.

[59] M. e. Holtz, Y. Yu, H. d. Abruña, and D. a. Muller, "In-situ Electron Energy Loss Spectroscopy of Liquids," *Microsc. Microanal.*, vol. 18, no. Supplement S2, pp. 1094–1095, 2012, doi: 10.1017/S1431927612007325.

[60] T. J. Woehl, J. E. Evans, I. Arslan, W. D. Ristenpart, and N. D. Browning, "Direct in situ determination of the mechanisms controlling nanoparticle nucleation and growth," *ACS Nano*, vol. 6, no. 10, pp. 8599–8610, 2012, doi: 10.1021/nn303371y.

[61] E. A. Ring and N. De Jonge, "Microfluidic system for transmission electron microscopy," *Microsc. Microanal.*, vol. 16, no. 5, pp. 622–629, 2010, doi: 10.1017/S1431927610093669.

[62] K. Nishijima, J. Yamasaki, H. Orihara, and N. Tanaka, "Development of microcapsules for electron microscopy and their application to dynamical observation of liquid crystals in transmission electron microscopy," *Nanotechnology*, vol. 15, no. 6, 2004, doi: 10.1088/0957-4484/15/6/001.

[63] L. R. Parent *et al.*, "Direct in situ observation of nanoparticle synthesis in a liquid crystal surfactant template," *ACS Nano*, vol. 6, no. 4, pp. 3589–3596, 2012, doi: 10.1021/nn300671g.

[64] D. B. Peckys and N. De Jonge, "Visualizing gold nanoparticle uptake in live cells with liquid scanning transmission electron microscopy," *Nano Lett.*, vol. 11, no. 4, pp. 1733–1738, Apr. 2011, doi: 10.1021/nl200285r.

[65] A. Khelfa, C. Byun, J. Nelayah, G. Wang, C. Ricolleau, and D. Alloyeau, "Structural analysis of single nanoparticles in liquid by low-dose STEM nanodiffraction," *Micron*, vol. 116, no. September 2018, pp. 30–35, 2019, doi: 10.1016/j.micron.2018.09.008.

[66] M. Boholm and R. Arvidsson, "A Definition Framework for the Terms Nanomaterial and Nanoparticle," *Nanoethics*, vol. 10, no. 1, pp. 25–40, 2016, doi: 10.1007/s11569-015-0249-7.

[67] N. T. K. Thanh, N. Maclean, and S. Mahiddine, "Mechanisms of nucleation and growth of nanoparticles in solution," *Chem. Rev.*, vol. 114, no. 15, pp. 7610–7630, 2014, doi: 10.1021/cr400544s.

[68] H. Qin, X. Tan, W. Huang, J. Jiang, and H. Jiang, "Application of urea precipitation method in preparation of advanced ceramic powders," *Ceram. Int.*, vol. 41, no. 9, pp. 11598–11604, 2015, doi: 10.1016/j.ceramint.2015.06.032.

[69] D. Ramimoghadam, S. Bagheri, and S. B. A. Hamid, "Progress in electrochemical synthesis of magnetic iron oxide nanoparticles," *J. Magn. Magn. Mater.*, vol. 368, pp. 207–229, 2014, doi: 10.1016/j.jmmm.2014.05.015.

[70] P. P. Edwards and J. M. Thomas, "Gold in a metallic divided state - From Faraday to present-day nanoscience," *Angew. Chemie - Int. Ed.*, vol. 46, no. 29, pp. 5480–5486, 2007, doi: 10.1002/anie.200700428.

[71] S. Alex and A. Tiwari, "Functionalized gold nanoparticles: Synthesis, properties and applications-A review," *J. Nanosci. Nanotechnol.*, vol. 15, no. 3, pp. 1869–1894, 2015, doi: 10.1166/jnn.2015.9718.

[72] P. Zhao, N. Li, and D. Astruc, "State of the art in gold nanoparticle synthesis," *Coord. Chem. Rev.*, vol. 257, no. 3–4, pp. 638–665, 2013, doi: 10.1016/j.ccr.2012.09.002.

[73] H. Gong *et al.*, "Gold nanoparticle transfer through photothermal effects in a metamaterial absorber by nanosecond laser.," *Sci. Rep.*, vol. 4, p. 6080, 2014, doi: 10.1038/srep06080.

[74] Q. Chen *et al.*, "3D motion of DNA-Au nanoconjugates in graphene liquid cell electron microscopy," *Nano Lett.*, vol. 13, no. 9, pp. 4556–4561, 2013, doi: 10.1021/nl402694n.

[75] K. L. Jungjohann, S. Bliznakov, P. W. Sutter, E. A. Stach, and E. A. Sutter, "In situ liquid cell electron microscopy of the solution growth of Au-Pd core-shell nanostructures," *Nano Lett.*, vol. 13, no. 6, pp. 2964–2970, 2013, doi: 10.1021/nl4014277.

[76] M. H. Nielsen *et al.*, "Investigating Processes of Nanocrystal Formation and Transformation via Liquid Cell TEM," *Microsc. Microanal.*, vol. 20, no. 02, pp. 425–436, Apr. 2014, doi: 10.1017/S1431927614000294.

[77] P. Wang, X. Wang, L. Wang, X. Hou, W. Liu, and C. Chen, "Interaction of gold nanoparticles with proteins and cells," *Sci. Technol. Adv. Mater.*, vol. 16, no. 3, 2015, doi: 10.1088/1468-6996/16/3/034610.

[78] A. Hutzler *et al.*, "In Situ Liquid Cell TEM Studies on Etching and Growth Mechanisms of Gold Nanoparticles at a Solid–Liquid–Gas Interface," *Adv. Mater. Interfaces*, vol. 6, no. 20, 2019, doi: 10.1002/admi.201901027.

[79] M. Khajelakzay, R. Shoja Razavi, M. Barekat, M. Naderi, and M. Milani, "Synthesis of yttria nanopowders by two precipitation methods and investigation of synthesis conditions," *Int. J. Appl. Ceram. Technol.*, vol. 13, no. 1, pp. 209–218, 2016, doi: 10.1111/ijac.12430.

[80] M. D. Fokema, E. Chiu, and J. Y. Ying, "Synthesis and characterization of nanocrystalline yttrium oxide prepared with tetraalkylammonium hydroxides," *Langmuir*, vol. 16, no. 7, pp. 3154–3159, 2000, doi: 10.1021/la991156j.

[81] R. Srinivasan, N. R. Yogamalar, J. Elanchezhiyan, R. J. Joseyphus, and A. C. Bose, "Structural and optical properties of europium doped yttrium oxide nanoparticles for phosphor applications," *J. Alloys Compd.*, vol. 496, no. 1–2, pp. 472–477, 2010, doi: 10.1016/j.jallcom.2010.02.083.

[82] A. Senthil Kumar, A. Raja Durai, and T. Sornakumar, "Yttria ceramics: Cutting tool application," *Mater. Lett.*, vol. 58, no. 11, pp. 1808–1810, 2004, doi: 10.1016/j.ijcard.2014.07.094.

[83] D. Schubert, R. Dargusch, J. Raitano, and S. W. Chan, "Cerium and yttrium oxide nanoparticles are neuroprotective," *Biochem. Biophys. Res. Commun.*, vol. 342, no. 1, pp. 86–91, 2006, doi: 10.1016/j.bbrc.2006.01.129.

[84] V. M. Lojpur, P. S. Ahrenkiel, and M. D. Dramićanin, "Color-tunable up-conversion emission in Y2O3:Yb3+, Er3+ nanoparticles prepared by polymer complex solution method," *Nanoscale Res. Lett.*, vol. 8, no. 1, p. 131, 2013, doi: 10.1186/1556-276X-8-131.

[85] M. Khajelakzay, S. R. Bakhshi, G. H. Borhani, and M. Ramazani, "Synthesis and Spark Plasma Sintering of Mg2Si Nanopowder by Mechanical Alloying and Heat Treatment," *Int. J. Appl. Ceram. Technol.*, vol. 13, no. 3, pp. 498–505, 2016, doi: 10.1111/ijac.12522.

[86] J. E. Alaniz, F. G. Perez-Gutierrez, G. Aguilar, and J. E. Garay, "Optical properties of transparent nanocrystalline yttria stabilized zirconia," *Opt. Mater. (Amst).*, vol. 32, no. 1, pp. 62–68, 2009, doi: 10.1016/j.optmat.2009.06.004.

[87] W. H. R. Shaw and J. J. Bordeaux, "The Decomposition of Urea in Aqueous Media," *J. Am. Chem. Soc.*, vol. 77, no. 18, pp. 4729–4733, 1955, doi: 10.1021/ja01623a011.

[88] S. Peng, C. Wang, J. Xie, and S. Sun, "Synthesis and stabilization of monodisperse Fe nanoparticles," *J. Am. Chem. Soc.*, vol. 128, no. 33, pp. 10676–10677, 2006, doi: 10.1021/ja063969h.

[89] S. Kayal and R. V. Ramanujan, "Anti-cancer drug loaded iron-gold core-shell nanoparticles (Fe@Au) for magnetic drug targeting," *J. Nanosci. Nanotechnol.*, vol. 10, no. 9, pp. 5527–5539, 2010, doi: 10.1166/jnn.2010.2461.

[90] C. H. Griffiths, M. P. O'Horo, and T. W. Smith, "The structure, magnetic characterization, and oxidation of colloidal iron dispersions," *J. Appl. Phys.*, vol. 50, no. 11, pp. 7108–7115, 1979, doi: 10.1063/1.325819.

[91] Z. Sun *et al.*, "Controlled Nano-Bio Interface of Functional Nanoprobes for in Vivo Monitoring Enzyme Activity in Tumors," *ACS Nano*, vol. 13, no. 2, pp. 1153–1167, 2019, doi: 10.1021/acsnano.8b05825.

[92] J. J. De Yoreo, "Principles of Crystal Nucleation and Growth," *Rev. Mineral. Geochemistry*, vol. 54, no. 1, pp. 57–93, 2003, doi: 10.2113/0540057.

[93] J. Gilmour, *Microphysics of Clouds and Precipitation*, vol. 31, no. 5. 1980.

[94] M. H. Nielsen, S. Aloni, and J. J. De Yoreo, "In situ TEM imaging of $CaCO_3$ nucleation reveals coexistence of direct and indirect pathways," *Science (80-.).*, vol. 345, no. 6201, pp. 1158–1162, 2014, doi: 10.1126/science.1254051.

[95] S. Ishizuka, Y. Kimura, and T. Yamazaki, "In situ FT-IR study on the homogeneous nucleation of nanoparticles of titanium oxides from highly supersaturated vapor," *J. Cryst. Growth*, vol. 450, no. June 2016, pp. 168–173, 2016, doi: 10.1016/j.jcrysgro.2016.06.036.

[96] J. Polte *et al.*, "Nucleation and growth of gold nanoparticles studied via in situ small angle X-ray scattering at millisecond time resolution," *ACS Nano*, vol. 4, no. 2, pp. 1076–1082, 2010, doi: 10.1021/nn901499c.

[97] M. Niederberger and H. Cölfen, "Oriented attachment and mesocrystals: Non-classical crystallization mechanisms based on nanoparticle assembly," *Phys. Chem. Chem. Phys.*, vol. 8, no. 28, pp. 3271–3287, 2006, doi: 10.1039/b604589h.

[98] P. J. Skrdla, "Use of dispersive kinetic models for nucleation and denucleation to predict steady-state nanoparticle size distributions and the role of Ostwald ripening," *J. Phys. Chem. C*, vol. 116, no. 1, pp. 214–225, 2012, doi: 10.1021/jp2080513.

[99] M. Grzelczak, J. Vermant, E. M. Furst, and L. M. Liz-Marzán, "Directed self-assembly of nanoparticles," *ACS Nano*, vol. 4, no. 7, pp. 3591–3605, 2010, doi: 10.1021/nn100869j.

[100] G. M. Whitesides and B. Grzybowski, "{S}elf-{A}ssembly at {A}ll {S}cales," *Science (80-.).*, vol. 295, no. 5564, pp. 2418–2421, 2002, doi: 10.1126/science.1070821.

[101] J. W. P. Schmelzer, *Nucleation Theory and Applications*. WILEY, 2005.

[102] G. Cao and Y. Wang, *Nanostructures and Nanomaterials*, vol. Volume 2. WORLD SCIENTIFIC, 2011.

[103] L. Zang, "Lecture 12 : Heterogeneous Nucleation : a surface catalyzed process," 2015. http://www.eng.utah.edu/~lzang/images/lecture-12.pdf.

[104] O. B. Brett, C. M. ; Maria, "Electrochemistry: Principles, methods, and applications," *Oxford Univ. Press.*, p. 426, 1999, doi: 10.1515/bmte.1999.44.s2.11.

[105] D. Pečko, "Electrochemical Study and Synthesis of Fe-Pd Ferromagnetic Nanowires for Future Magnetic Applications: Doctoral Dissertation.," Jožef Stefan Interantional Postgraduate School, 2004.

[106] T. P. Deangelis and W. R. Heineman, "An electrochemical experiment using an optically transparent thin layer electrode," *Journal of Chemical Education*, vol. 53, no. 9. pp. 594–597, 1976, doi: 10.1021/ed053p594.

[107] S. R. C. Douglas A. Skoog, Donald M. West, F. James Holler, *Fundamentals of Analytical Chemistry*. Cengage Learning, 2013.

[108] L. R. F. Allen J. Bard, *ELECTROCHEMICAL METHODS Fundamentals and Applications*. 2001.

[109] "Chemistry Cartoon PNG - Transparent PNG Image." https://www.subpng.com/png-5ftvip/download.html.

[110] C. G. Zoski, *Handbook of electrochemistry*. 2007.

[111] W. Plieth, *Electrochemistry for Materials Science*. 2008.

[112] Š. Trafela, J. Zavašnik, S. Šturm, and K. Ž. Rožman, "Formation of a Ni(OH)2/NiOOH active redox couple on nickel nanowires for formaldehyde detection in alkaline media," *Electrochim. Acta*, vol. 309, pp. 346–353, 2019, doi: 10.1016/j.electacta.2019.04.060.

[113] D. Pletcher *et al.*, *Electrochemistry, Volume 10.*, vol. 10. 1985.

[114] Š. Trafela, "Development of nanostructured redox couple N i (O H) 2 NiOOH-Ni based receptor elements for detection of formaldehyde in alkaline media : doctoral dissertation = Razvoj nanostrukturiranih receptorskih elementov za detekcijo formaldehida v alkalnih medij," Jožef Stefan Interantional Postgraduate School, 2020.

[115] "4.6: Pourbaix Diagrams," *LibreTexts librarie*. https://chem.libretexts.org/Bookshelves/Inorganic_Chemistry/Book%3A_Introduction_to_Inorganic_Chemistry/04%3A_Redox_Stability_and_Redox_Reactions/4.06%3A_Pourbaix_Diagrams.

[116] V. Upadhyay and D. Battocchi, "Localized electrochemical characterization of organic coatings: A brief review," *Prog. Org. Coatings*, vol. 99, pp. 365–377, 2016, doi: 10.1016/j.porgcoat.2016.06.012.

[117] F. Mansfeld, “Use of electrochemical impedance spectroscopy for the study of corrosion protection by polymer coatings I ---I I,” *J. Appl. Electrochem.*, vol. 25, pp. 187–202, 1995, doi: 10.1007/BF00262955.

[118] Y. X. Yin, S. Xin, Y. G. Guo, and L. J. Wan, “Lithium-sulfur batteries: Electrochemistry, materials, and prospects,” *Angew. Chemie - Int. Ed.*, vol. 52, no. 50, pp. 13186–13200, 2013, doi: 10.1002/anie.201304762.

[119] A. B. Stambouli and E. Traversa, “Solid oxide fuel cells (SOFCs): A review of an environmentally clean and efficient source of energy,” *Renew. Sustain. Energy Rev.*, vol. 6, no. 5, pp. 433–455, 2002, doi: 10.1016/S1364-0321(02)00014-X.

[120] E. Fahrenkrug, D. H. Alsem, N. Salmon, and S. Maldonado, “Electrochemical Measurements in In Situ TEM Experiments,” *J. Electrochem. Soc.*, vol. 164, no. 6, pp. H358–H364, 2017, doi: 10.1149/2.1041706jes.

[121] E. R. White *et al.*, “In situ transmission electron microscopy of lead dendrites and lead ions in aqueous solution,” *ACS Nano*, vol. 6, no. 7, pp. 6308–6317, 2012, doi: 10.1021/nn3017469.

[122] F. Wu and N. Yao, “Advances in sealed liquid cells for in-situ TEM electrochemial investigation of lithium-ion battery,” *Nano Energy*, vol. 11, pp. 196–210, 2015, doi: 10.1016/j.nanoen.2014.11.004.

[123] B. L. Mehdi *et al.*, “In-situ electrochemical transmission electron microscopy for battery research,” *Microsc. Microanal.*, vol. 20, no. 2, pp. 484–492, 2014, doi: 10.1017/S1431927614000488.

[124] X. H. Liu and J. Y. Huang, “In situ TEM electrochemistry of anode materials in lithium ion batteries,” *Energy Environ. Sci.*, vol. 4, no. 10, pp. 3844–3860, 2011, doi: 10.1039/c1ee01918j.

[125] Q. Su, J. Xie, J. Zhang, Y. Zhong, G. Du, and B. Xu, “In situ transmission electron microscopy observation of electrochemical behavior of CoS2 in lithium-ion battery,” *ACS Appl. Mater. Interfaces*, vol. 6, no. 4, pp. 3016–3022, 2014, doi: 10.1021/am4056084.

[126] R. Unocic, L. Adamczyk, N. Dudney, D. Alsem, N. Salmon, and K. More, “ In-situ TEM Characterization of Electrochemical Processes in Energy Storage Systems ,” *Microsc. Microanal.*, vol. 17, no. S2, pp. 1564–1565, 2011, doi: 10.1017/s1431927611008695.

[127] J. Fuller, “The Room Temperature Ionic Liquid 1-Ethyl-3-methylimidazolium Tetrafluoroborate: Electrochemical Couples and Physical Properties,” *J. Electrochem. Soc.*, vol. 144, no. 11, p. 3881, 1997, doi: 10.1149/1.1838106.

[128] N. Feature, "Toyota, JFCC breakthrough in real-time observation of fuel cell catalyst degradation," *Fuel Cells Bull.*, vol. 2015, no. 6, pp. 14–15, 2015, doi: 10.1016/S1464-2859(15)30167-X.

[129] G. Z. Zhu, S. Prabhudev, J. Yang, C. M. Gabardo, G. A. Botton, and L. Soleymani, "In situ liquid cell TEM study of morphological evolution and degradation of Pt-Fe nanocatalysts during potential cycling," *J. Phys. Chem. C*, vol. 118, no. 38, pp. 22111–22119, 2014, doi: 10.1021/jp506857b.

[130] H. Kim, J. T. Lee, A. Magasinski, K. Zhao, Y. Liu, and G. Yushin, "In Situ TEM Observation of Electrochemical Lithiation of Sulfur Confined within Inner Cylindrical Pores of Carbon Nanotubes," *Adv. Energy Mater.*, vol. 5, no. 24, pp. 1–7, 2015, doi: 10.1002/aenm.201501306.

[131] E. P. Randviir, D. A. C. Brownson, M. Gómez-Mingot, D. K. Kampouris, J. Iniesta, and C. E. Banks, "Electrochemistry of Q-Graphene," *Nanoscale*, vol. 4, no. 20, pp. 6470–6480, 2012, doi: 10.1039/c2nr31823g.

[132] M. Sluyters-Rehbach, J. H. O. J. Wijenberg, E. Bosco, and J. H. Sluyters, "The theory of chronoamperometry for the investigation of electrocrystallization. Mathematical description and analysis in the case of diffusion-controlled growth," *Journal of Electroanalytical Chemistry*, vol. 236, no. 1–2. pp. 1–20, 1987, doi: 10.1016/0022-0728(87)88014-2.

[133] J. Heinze, "Cyclic Voltammetry—'Electrochemical Spectroscopy'. New Analytical Methods (25)," *Angewandte Chemie International Edition in English*, vol. 23, no. 11. pp. 831–847, 1984, doi: 10.1002/anie.198408313.

[134] B. Ambrožič *et al.*, "Controlling the radical-induced redox chemistry inside a liquid-cell TEM," *Chem. Sci.*, vol. 10, no. 38, pp. 8735–8743, 2019, doi: 10.1039/c9sc02227a.

[135] N. Ahmad, Y. Le Bouar, C. Ricolleau, and D. Alloyeau, "Growth of dendritic nanostructures by liquid-cell transmission electron microscopy: a reflection of the electron-irradiation history," *Adv. Struct. Chem. Imaging*, vol. 2, no. 1, p. 9, Jun. 2017, doi: 10.1186/s40679-016-0023-0.

[136] Prototochips Inc, "Poseidon select: TEM micrscopy liquid cell." https://www.protochips.com/products/poseidon-select/.

[137] M. J. Williamson, R. M. Tromp, P. M. Vereecken, R. Hull, and F. M. Ross, "Dynamic microscopy of nanoscale cluster growth at the solid-liquid interface," *Nat. Mater.*, vol. 2, no. 8, pp. 532–536, 2003, doi: 10.1038/nmat944.

[138] N. Moreno, "Image Processing with ImageJ," *Image (Rochester, N.Y.)*, pp. 249–258, 2007, doi: Image Processing with ImageJ. (2006). Optical Imaging Techniques in Cell Biology, 249–258. doi:10.1201/9781420005615.ax4.

[139] D. R. G. Mitchell, "DiffTools: Electron diffraction software tools for DigitalMicrograph™," *Microsc. Res. Tech.*, vol. 71, no. 8, pp. 588–593, 2008, doi: 10.1002/jemt.20591.

[140] Elliot, A.J. Bartels, D.M., "The Reaction Set, Rate Constants and g-Values for the Simulation of the Radiolysis of Light Water over the Range 20° to 350°C Based on Information Available in 2008; Report AECL No. 153-127160-450-001; Atomic Energy of Canada Ltd.: Chalk River, ON, 2009," 2009.

[141] G. Zhu, Y. Jiang, W. Huang, H. Zhang, F. Lin, and C. Jin, "Atomic resolution liquid-cell transmission electron microscopy investigations of the dynamics of nanoparticles in ultrathin liquids," *Chem. Commun.*, vol. 49, no. 93, p. 10944, 2013, doi: 10.1039/c3cc46667a.

[142] C. L. Young, "Solubility data series, volume 5/6, Hydrogen and Deuterium," in *IUPAC-NIST Solubility Database, Version 1.1*, 1981.

[143] R. Battino, "Solubility data series, volume 7, Oxygen and ozone," in *IUPAC-NIST Solubility Database, Version 1.1*, 1981.

[144] H. L. Xin, K. Niu, D. H. Alsem, and H. Zheng, "In Situ TEM Study of Catalytic Nanoparticle Reactions in Atmospheric Pressure Gas Environment.," *Microsc. Microanal.*, vol. 19, no. 6, pp. 1558–68, 2013, doi: 10.1017/S1431927613013433.

[145] J. J. Lingane, "Standard potentials of half-reactions involving + 1 and + 3 gold in chloride medium: Equilibrium constant of the reaction AuCl4− + 2Au + 2Cl− = 3AuCl2−," *J. Electroanal. Chem.*, vol. 4, no. 6, pp. 332–342, Dec. 1962, doi: 10.1016/0022-0728(62)80079-5.

[146] G. V Buxton, C. L. Greenstock, W. P. Helman, and A. B. Ross, "Critical Review of rate constants for reactions of hydrated electrons, hydrogen atoms and hydroxyl radicals in aqueous solution," *J. Phys. Chem. Ref. Data*, vol. 17, no. 2, p. 513, 1988, doi: 10.1063/1.555805.

[147] H. A. Schwarz, "Free Radicals Generated by Radiolysis of Aqueous Solutions," vol. 58, no. 2, pp. 101–105, 1981, doi: 10.1021/ed058p101.

[148] G. S. Bratsch, "Standards Electrode Potentials and Temperature Coefficients in water at 298.15 K," *J. Phys. Chem. Ref. Data*, vol. 18, no. 1, pp. 1– 21, 1989.

[149] S. Armstrong, D. A., Huie; R. E.; Lymar, S.;Koppenol, W. H.;Merényi, G.; Neta, P.; Ruscic, B.; Stanbury, D. M.; Steenken, "Standard Electrode Potentials Involving Radicals in Aqueous Solution : Inorganic Radicals (IUPAC Technical Report)," *Pure Appl. Chem.*, vol. 87, pp. 1139–1150, 2015.

[150] E. J. Ghosh Mazumdar, A. S. and Hart, "A Pulse Radiolysis Study of Bivalent and Zerovalent Gold in Aqueous Solutions," in *Radiation Chemistry*, 1968, pp. 193–209.

[151] B. Pastina and J. A. Laverne, "Pastina_2001_Effect of Molecular Hydrogen on Hydrogen Peroxide in Water Radiolysis.pdf," pp. 9316–9322, 2001.

[152] E. Hayon, "Radiolysis of Air-Free Aqueous Solutions of Hydrogen Peroxide," *Serv. Chim. C.E.N. Saclay*, pp. 1059–1067, 1963.

[153] C. J. Hochanadel, "Effects of Cobalt γ-Radiation on Water and Aqueous Solutions," *J. Phys. Chem.*, vol. 56, no. 5, pp. 587–594, 1952, doi: 10.1021/j150497a008.

[154] N. J. B. Green, M. J. Pilling, S. M. Pimblott, and P. Clifford, "Stochastic modeling of fast kinetics in a radiation track," *J. Phys. Chem.*, vol. 94, no. 1, pp. 251–258, 1990, doi: 10.1021/j100364a041.

[155] R. F. Anderson, B. Vojnovic, and B. D. Michael, "The radiation-chemical yields of H_3O^+ and OH^- as determined by nanosecond conductimetric measurements," *Radiat. Phys. Chem.*, vol. 26, no. 3, pp. 301–303, 1985, doi: 10.1016/0146-5724(85)90068-8.

[156] E. Atinault, V. De Waele, U. Schmidhammer, M. Fattahi, and M. Mostafavi, "Scavenging of es^- and $OH^\cdot$ radicals in concentrated HCl and NaCl aqueous solutions," *Chem. Phys. Lett.*, vol. 460, no. 4–6, pp. 461–465, 2008, doi: 10.1016/j.cplett.2008.06.048.

[157] R Winston Revie; Herbert Henry Uhlig, *Uhlig's corrosion handbook*, Electroche. Wiley, 2011.

[158] K. Pacławski, K. and Fitzner, "Kinetics of Reduction of Gold(III) Complexes Using H_2O_2," *Metall. Mater. Trans. B*, vol. 37B, no. 5, pp. 703–714, 2006, doi: 10.1007/s11663-006-0054-3.

[159] B. G. Ershov, E. V. Abkhalimov, R. D. Solovov, and V. I. Roldughin, "Gold nanoparticles in aqueous solutions: Influence of size and pH on hydrogen dissociative adsorption and Au(III) ion reduction," *Phys. Chem. Chem. Phys.*, vol. 18, no. 19, 2016, doi: 10.1039/c6cp01996j.

[160] S. Wang *et al.*, "Universal transition state scaling relations for (de)hydrogenation over transition metals," *Phys. Chem. Chem. Phys.*, vol. 13, pp. 20760–20765, 2011, doi: 10.1039/c1cp20547a.

[161] Y. Yang, C. Dai, A. Fisher, and Y. Shen, "A full understanding of oxygen reduction reaction mechanism on Au (1 1 1) surface," 2017.

[162] F. Habahchi, *Kinetics and Mechanism of Gold and Silver Dissolution in Cyanide Solution*. Montana Bureau of Mines Geological Bulletin 59, 1967.

[163] C. L. Young, "Volume 5/6, Hydrogen and Deuterium," in *IUPAC-NIST Solubility Database*, Oxford, U.K.: Pergamon Press, 1981, pp. 1–3.

[164] R. Battino, "Volume 7, Oxygen and ozone," in *IUPAC-NIST Solubility Database*, Oxford, U.K.: Pergamon Press, 1981, pp. 1–5.

[165] N. M. Schneider, M. M. Norton, B. J. Mendel, J. M. Grogan, M. Frances, and H. H. Bau, "Electron - Water Interactions and Implications for Liquid Cell Electron Microscopy – Supporting Information," *J. Phys. Chem. C*, vol. 118, no. 38, pp. 22373–22382, 2014.

[166] W. Su, M. He, J. Xing, Y. Zhong, and Z. Li, "Facile synthesis of porous bifunctional Fe3O4@Y2O3:Ln nanocomposites using carbonized ferrocene as templates," *RSC Adv.*, vol. 3, no. 48, pp. 25970–25975, 2013, doi: 10.1039/c3ra44986f.

[167] S. Huang *et al.*, "Rapid, morphologically controllable, large-scale synthesis of uniform Y(OH)3 and tunable luminescent properties of Y2O3:Yb3+/Ln3+ (Ln = Er, Tm and Ho)," *J. Mater. Chem.*, vol. 22, no. 31, p. 16136, 2012, doi: 10.1039/c2jm32412a.

[168] Q. Su, D. Xie, J. Zhang, G. Du, and B. Xu, "In situ transmission electron microscopy observation of the conversion mechanism of Fe2O3/graphene anode during Lithiation-Delithiation processes," *ACS Nano*, vol. 7, no. 10, pp. 9115–9121, 2013, doi: 10.1021/nn403720p.

[169] K. Yoshida, Z. Xudong, A. N. Bright, K. Saitoh, and N. Tanaka, "Dynamic environmental transmission electron microscopy observation of platinum electrode catalyst deactivation in a proton-exchange-membrane fuel cell," *Nanotechnology*, vol. 24, no. 6, 2013, doi: 10.1088/0957-4484/24/6/065705.

[170] P. Ohresser *et al.*, "Growth, structure, and magnetism of fcc fe ultrathin films on cu(111) by pulsed laser deposition," *Phys. Rev. B - Condens. Matter Mater. Phys.*, vol. 59, no. 5, pp. 3696–3706, 1999, doi: 10.1103/PhysRevB.59.3696.

[171] S. Park, Y. Cho, W. Kim, and S. Kim, "Understanding of Homogeneous Spontaneous Precipitation for Monodispersed TiO 2 Ultrafine Powders with Rutile Phase around Room Temperature," *J. Solid State Chem.*, vol. 238, pp. 230–238, 1999, doi: 10.1006/jssc.1999.8342.

[172] I. P. Bell, M. A. J. Rodgers, and H. D. Burrows, "Kinetic and thermodynamic character of reducing species produced on pulse radiolysis of acetonitrile," *J. Chem. Soc. Faraday Trans. 1 Phys. Chem. Condens. Phases*, vol. 73, pp. 315–326, 1977, doi: 10.1039/F19777300315.

[173] A. J. Koster and W. J. de Ruijter, "Practical autoalignment of transmission electron microscopes," *Ultramicroscopy*, vol. 40, no. 2, pp. 89–107, 1992, doi: 10.1016/0304-3991(92)90052-L.

[174] IAEA, "NUCLEAR POWER REACTORS IN THE WORLD," Vienna, 2018.

[175] P. Ho, “Spent nuclear fuel policies in historical perspective : An international comparison,” vol. 37, pp. 254–263, 2009, doi: 10.1016/j.enpol.2008.09.043.

[176] H. Christensen, S. Sunder, H. C. Studsvik, and M. Ab, “Current State of Knowledge of Water Radiolysis Effects on Spent Nuclear Fuel Corrosion CURRENT STATE OF KNOWLEDGE OF WATER RADIOLYSIS EFFECTS ON SPENT NUCLEAR FUEL CORROSION MANAGEMENT AND DISPOSAL,” vol. 5450, no. September, 2017, doi: 10.13182/NT00-A3107.

[177] S. Sunder and H. Christensen, “Gamma Radiolysis of Water Solutions Relevant to the Nuclear Fuel Waste Management Program GAMMA RADIOLYSIS OF WATER SOLUTIONS RELEVANT TO THE NUCLEAR FUEL WASTE,” vol. 5450, no. December, 2017, doi: 10.13182/NT93-A34900.

[178] B. Pastina, J. Isabey, and B. Hickel, “The in ¯ uence of water chemistry on the radiolysis of the primary coolant water in pressurized water reactors,” vol. 264, no. April 1998, 1999.

[179] C. Petrucci, “Efficiency of radiation protection equipment in interventional radiology : a systematic Monte Carlo study of eye lens and whole body doses Efficiency of radiation protection equipment in interventional radiology : a systematic Monte Carlo study of eye len,” 2015, doi: 10.1088/0952-4746/34/3/509.

[180] T. G. T. Tadeusz Sarna, Barbara Pilas, Edward J. Land, “Interaction of radicals from water radiolysis with melanin,” *Biochim. Biophys. Acta - Gen. Subj.*, vol. 883, no. 1, pp. 162–167, 1986, doi: https://doi.org/10.1016/0304-4165(86)90147-9.

[181] R. W. Carlson and M. S. Anderson, “Sulfuric Acid Production on Europa : The Radiolysis of Sulfur in Water Ice,” vol. 463, pp. 456–463, 2002, doi: 10.1006/icar.2002.6858.

[182] R. E. Johnson and T. I. Quickenden, “Photolysis and radiolysis of water ice on outer solar system bodies,” vol. 102, 1997.

Bibliography

Publications Related to the Thesis

Journal Articles

B. Ambrožič, A. Prašnikar, N. Hodnik, N. Kostevšek, B. Likozar, K. Ž. Rožman, and S. Šturm, "Controlling the radical-induced redox chemistry inside a liquid-cell TEM," *Chemical Science*, vol. 10, no. 38, pp. 8735–8743, 2019.

G. I. Akmehmet, S. Šturm, L. Bocher, M. Kociak, B. Ambrožič, and C. W. Ow-Yang, "Structure and Luminescence in Long Persistence Eu, Dy, and B Codoped Strontium Aluminate Phosphors: The Boron Effect," Journal of the American Ceramic Society, vol. 99, no. 6, pp. 2175–2180, 2016.

Other Publications

G. I. Akmehmet, S. Šturm, M. Komelj, Z. Samardžija, B. Ambrožič, M. Sezen, M. Čeh, and C. W. Ow-Yang, "Origin of long afterglow in strontium aluminate phosphors: Atomic scale imaging of rare earth dopant clustering," Ceramics International, vol. 45, no. 16, pp. 20073–20077, 2019.

J. Kadok, K. Pussi, S. Šturm, B. Ambrožič, É. Gaudry, M.-C. D. Weerd, V. Fournée, and J. Ledieu, "Epitaxial growth of Al9Ir2 intermetallic compound on Al(100): Mechanism and interface structure," Physical Review Materials, vol. 2, no. 4, 2018.

B. Leskovar, S. Šturm, Z. Samardžija, B. Ambrožič, B. Markoli, and I. Naglič, "Epitaxial growth of a metastable icosahedral quasicrystal on a stable icosahedral quasicrystal substrate," Scripta Materialia, vol. 150, pp. 92–95, 2018.

M. Miler, B. Ambrožič, B. Mirtič, M. Gosar, S. Šturm, M. Dolenec, and M. Jeršek, "Mineral and chemical composition of the Jezersko meteorite-A new chondrite from Slovenia," Meteoritics & Planetary Science, vol. 49, no. 10, pp. 1875–1887, 2014.

B. Ambrožič, S. Šturm, M. Jeršek, and B. Mirtič, "Structure of the chondrules and the chemical composition of olivine in meteorite Jesenice," Geologija, vol. 56, no. 1, pp. 19–28, 2013.

B. Ambrožič, S. Šturm, M. Jeršek, and B. Mirtič, "Classification of stony meteorites and chondrules – the case of meteorite Jesenice," Geologija, vol. 55, no. 2, pp. 163–180, 2012.

Scientific Conference Contributing Abstracts

B. Ambrožič, N. Kostevšek, K. Ž. Rožman, S. Šturm. In-situ observations of the growth of the gold nanoparticles. V: M. Pavlin (ur.), et al. *Zbornik = Proceedings*. 9. študentska konferenca Mednarodne podiplomske šole Jožefa Stefana in 11. dan mladih raziskovalcev (Konferenca KMBO) = 9th Jožef Stefan International Postgraduate School Students' Conference and 11th Young researchers' Day, [19.-20. 4. 2017, Ljubljana, Slovenija]. Ljubljana: Mednarodna podiplomska šola Jožefa Stefana: = Jožef Stefan International Postgraduate School: Inštitut Jožef Stefan: = Jožef Stefan Institute, 2017. str. 45.

B. Ambrožič, N. Kostevšek, M. Bele, S. Šturm. First dynamic study of yttrium-based nanoparticles formation at the nanoscale by using transmission electron microscopy combined with the liquid cell. V: S. P. Mihevc (ur.), M. Prunk (ur.), J. Pungerčar (ur.). *10th Young researchers' day, 31 March, 2016, Ljubljana : program and abstract book*. Ljubljana: Institut Jožef Stefan, 2016. str. 13.

B. Ambrožič, N. Kostevšek, K. Ž. Rožman, M. Bele, S. Šturm. Observations of nucleation and growth of gold nanoparticles grown from chloroauric acid solution by using transmission electron microscopy combined with the liquid cell. V: M. Godec (ur.), et al. *Program in knjiga povzetkov = Program and book of abstracts*. 24. mednarodna konferenca o materialih in tehnologijah, 28.-30. september 2016, Portorož, Slovenija = 24th International Conference on Materials and Technology, 28-30 September 2016, Portorož, Slovenia. Ljubljana: Inštitut za kovinske materiale in tehnologije. 2016, str. 30. ISBN 978-961-94088-0-3.

B. Ambrožič, N. Kostevšek, K. Ž. Rožman, M. Bele, S. Šturm. Three-dimensional characterization of Ni−Sm0.2Ce0.8O2−σNi−Sm0.2Ce0.8O2−σ cermet for SOFC anodes by high-resolution FIB-SEM Tomography. V: *The 16th European microscopy congress 2016 August 28 - September 2, 2016 in Lyon, France*. [S. l.]: John Wiley & Sons, 2016. str. [1]. http://emc-proceedings.com/abstract/in-situ-liquid-cell-transmission-electron-microscopy-of-y-based-precursor-growth-dynamics-at-elevated-temperatures/.

J. Kadok, K. Pussi, S. Šturm, B. Ambrožič, É. Gaudry, M.-P. de Weerdt-Pilorge, V. Fournée, J. Ledieu. Epitaxial growth of Al9Ir2Al9Ir2 intermetallic compound on Al(100) : mechanism and interface structure. V: Z. Śniadecki (ur.). *Book of abstracts*. ECMetAC Days 2018, European Integrated Centre for the Development of Metallic Alloys and Compounds, December 3-5, 2018, Poznań, Poland. Poznań: Institute of Molecular Physics, Polish Academy of Sciences, 2018. str. 46-47. ISBN 978-83-933663-7-8.

B. Leskovar, S. Šturm, Z. Samardžija, B. Ambrožič, B. Markoli, I. Naglič. Epitaxial growth of metastable (P-type) Al-Mn-Si quasicrystal from the stable (F-type) Al-Cu-Fe quasicrystalline surface. V: V. Radmilović (ur.), V. Radmilović (ur.). *Program & book of abstracts*. First International Conference on Electron Microscopy of Nanostructures ELMINA 2018, August 27-29, 2018, Belgrade, Serbia = Prva međunarodna konferencija o elektronskoj mikroskopiji nanostruktura ELMINA 2018, 27-29 avgust 2018, Beograd, Srbija g[organized by Serbian Academy of Sciences and Arts and Faculty of Technology and Metallurgy, University of Belgrade. Belgrade: SASA, Serbian Academy of Sciences and Arts, 2018. str. 137-139. ISBN 978-86-7025-785-6.

C. O.-Yang, G. I. Akmehmet, S. Šturm, L. Bocher, M. Kociak, B. Ambrožič, M. Gec, D. F. Ece, M. Sezen. Elucidating the role of boron in extending persistence in Eu2+Eu2+ and Dy3+Dy3+ co-doped Sr4Al14O25Sr4Al14O25 by cathodoluminescence, STEM-EDXS, and electron diffraction. V: A. Šestan (ur.), et al. *Knjiga povzetkov = Book of abstracts*. 1. slovensko posvetovanje mikroskopistov = 1st Slovene Microscopy Symposium, 18. in 19. maj 2015, Piran, Slovenija. [S. l.: s. n., 2015].

A. Prašnikar, N. Hodnik, B. Ambrožič, S. Šturm, B. Likozar. Modelling of water radiolysis in the liquid cell electron microscopy. V: M. Pavlin (ur.), et al. *Zbornik = Proceedings*. 9. študentska konferenca Mednarodne podiplomske šole Jožefa Stefana in 11. dan mladih raziskovalcev (Konferenca KMBO) = 9th Jožef Stefan International Postgraduate School Students' Conference and 11th Young researchers' Day, [19.-20. 4. 2017, Ljubljana, Slovenija]. Ljubljana: Mednarodna podiplomska šola Jožefa Stefana: = Jožef Stefan International Postgraduate School: Inštitut Jožef Stefan: = Jožef Stefan Institute, 2017. str. 75. http://ipssc.mps.si/proceedings/Proceedings_IPSSC+CMBE_2017.pdf.

S. Šturm, B. Ambrožič, N. Kostevšek, M. Bele, K. Ž. Rožman. In situ studies of heat induced precipitation of yttria precursor using liquid-cell transmission electron microscopy. V: *Program and abstract*. 11th Asia Pacific Microwave Conference, 33rd Microscopy Society, 39th Anatomy Association of Thailand Annual Conference, APMC11, MST33/AAT39, May 23-27, 2016, Phuket, Thailand. [S. l.]: Anatomy Association of Thailand, cop. 2016. str. 149. ISBN 978-616-279-846-7.

S. Šturm, B. Ambrožič, M. Bele, N. Kostevšek, K. Ž. Rožman. Three-dimensional characterization of Ni−Sm0.2Ce0.8O2−σNi−Sm0.2Ce0.8O2−σ cermet for SOFC anodes by high-resolution FIB-SEM Tomography. V: *The 16th European microscopy congress 2016 August 28 - September 2, 2016 in Lyon, France*. [S. l.]: John Wiley & Sons, 2016. str. [1]. http://emc-proceedings.com/abstract/in-situ-studies-of-the-dendritic-yttria-precursor-nanostructures-growth-dynamics-at-elevated-temperatures-using-liquid-cell-transmission-electron-microscopy/.

S. Šturm, A. Prašnikar, N. Hodnik, B. Likozar, K. Ž. Rožman, N. Kostevšek, B. Ambrožič. The impact of the electron dose rate and temperature-dependent radiolysis products on the growth and dissolution of metal nanoparticles in LTEM. V: *19th International Microscopy Congress, Sydney, 9-14 September 2018*. Sydney: [s. n.]. 2018, str. [1-2]. http://abstracts.imc19.com/pdf/abstract_1334.pdf.

U. Wolff, B. Ambrožič, K. Ž. Rožman, K. Leistner, K. Nielsch, S. Šturm. In-situ observation of the reversible electrochemical deposition of Fe in a transmission electron microscope. *Microscopy and microanalysis*. [Print ed.]. 2019, vol. 24, supp. s1, str. 310-311. ISSN 1431-9276. DOI: 10.1017/S1431927618002040.

Biography

The author of this thesis, Bojan Ambrožič, was born on August 28th, 1989, in Jesenice, Slovenia. He finished his primary education in 2004 at Osnovna šola Antona Tomaža Linharta, Radovljica. He finished his secondary education at Srednja gostinska in turistična šola, Radovljica in 2008 and Gimnazija Kranj in 2009. He proceeded with his university study program in the Faculty for Natural Sciences and Engineering at the University of Ljubljana. On September 15th, 2012 under the supervision of Prof. Dr. Breda Mirtič and co-supervision of Prof. Dr. Sašo Šturm he obtained a bachelor's degree. He obtained a master's degree in geology on September 23rd, 2015, under the supervision of Prof. Dr. Sašo Šturm and co-supervision of Assist. Prof. Dr. Mirijam Vrabec. In October 2015, he continued with his PhD studies at the Jožef Stefan International Postgraduate School in the field of Nanosciences and Nanotechnologies under the supervision of Prof. Dr. Sašo Šturm at the Department for Nanostructured Materials, Jožef Stefan Institute, Ljubljana, Slovenia.